Self-referenced 1.5 μm Fiber Frequency Combs at GHz Repetition Rates

by

David Chao

B.S., Electrical and Computer Engineering
Cornell University (2003)

M.S., Electrical Engineering and Computer Science
Massachusetts Institute of Technology (2005)

Submitted to the Department of Electrical Engineering and Computer Science
in partial fulfillment of the requirements for the degree of

Doctor of Philosophy in Electrical Engineering and Computer Science

at the

MASSACHUSETTS INSTITUTE OF TECHNOLOGY

February 2012

Author .....
Department of Electrical Engineering and Computer Science
February 3, 2012

Certified by .....
Erich P. Ippen
Elihu Thomson Professor of Electrical Engineering
Professor of Physics
Thesis Supervisor

Accepted by .....
Leslie A. Kolodziejski
Chairman, Department Committee on Graduate Students

Self-referenced 1.5 μm Fiber Frequency Combs at GHz Repetition Rates

by

David Chao

Submitted to the Department of Electrical Engineering and Computer Science
on February 3, 2012, in Partial Fulfillment of the
Requirements for the Degree of Doctor of Philosophy in
Electrical Engineering and Computer Science

Abstract

Tremendous advances in recent years to the optical frequency comb, particularly frequency combs deriving from solid-state and fiber architectures, have enabled a host of important new applications to emerge – applications which include optical arbitrary waveform generation (OAWG), high-speed photonic analog-to-digital conversion (EPIC), space exploration (Astro-Comb) as well as precision spectroscopy and optical clocks. Fiber-based frequency combs have increasingly become attractive alternatives to solid-state systems due to their compact size and robust operation and have recently demonstrated performance comparable to their more traditional counterparts. One area for improvement, however, is in the repetition rate of such systems, as fiber frequency combs based on Ytterbium (Yb) and Erbium (Er) technologies currently only operate with repetition rates ≤1GHz and ≤300MHz, respectively, while solid-state frequency combs have been demonstrated up to 10GHz.

This thesis reports on the development of a 1 GHz repetition rate Erbium-doped fiber laser frequency comb and discusses its potential to be scaled to even higher repetition rates. Nanojoule femtosecond pulses are produced at a GHz repetition rate and used to generate over an octave of supercontinuum spanning 1μm-2.4μm. Carrier-envelope offset frequency (f_{ceo}) detection using f-2f self-referencing provides confirmation that the continuum's frequency comb structure remains intact after undergoing amplification, compression, and supercontinuum generation. The f_{ceo} beat, along with the laser repetition rate f_{rep}, are locked to stable microwave reference oscillators, yielding, to the best of our knowledge, the first octave-spanning self-referenced optical frequency comb centered at the 1.5μm telecom band generated at or above a GHz repetition rate.

Thesis Supervisor: Erich P. Ippen

Title: Elihu Thomson Professor of Electrical Engineering

Professor of Physics

Acknowledgements

(Insert Here: "The Book Of Love" – Peter Gabriel)

A very wise man once said, "All good things must eventually come to an end..." And so, as my time at MIT comes to an end, I can't help but reflect back on all of my wonderful memories here. There's so many of you to thank for this...

Much of the work presented in this thesis would not have come about were it not for the extraordinary vision of my advisor, Professor Erich P. Ippen. To be able to learn from one of the fathers of "mode-locking" has been an absolute privilege. From him, I learned that everything has a simple explanation. Every question has an answer, and every problem a solution. I hope I learned well.

To Professor Franz X. Kärtner, who essentially served as a second advisor to me, for providing help whenever and wherever possible. Full of brilliant ideas, my meetings with him were always tremendously rewarding. To him, no idea seemed impossible.

To Dr. Matthew E. Grein, the mentor to my mentor, for passing along valuable lab skills (even if indirectly). I would often hear the words "This is what Matt used to do..." before something new was introduced to me in the lab. It's been a real pleasure having you on my thesis committee.

To Jason Sickler. The man who taught me everything I know, both in and out of lab. Also the man who taught me the value of 50/50. Always knew how to get his point across, even if it meant having to go above and beyond the call of duty (and dropping everything else in the process), which was often the case. I learned a lot as a result.

To Andrew Benedick, Hyunil Byun, Noah Chang, Jeff Chen, Jonathan Cox, Marcus Dahlem, Jungwon Kim, Ali Motamedi, Jonathan Morse, and Michelle Sander for their many contributions to the completion of this thesis. In addition to them, I'd like to thank Siddharth Bhardwaj, Li-Jin Chen, Edilson Falcao-Filho, Peter Fendel, Irek Grulkowski, Anatoly Khilo, Jonathan Liu, Jeff Moses, Amir Nejadmalayeri, Milos Popovic, Ben Potsaid, Peter Rakich, Alphan Sennaroglu, Hanfei Shen, Katia Shtyrkova, Aleem Siddiqui, Kenny Tao, Chao Zhou, Rona Zhou, Donna Gale and Dorothy Fleisher for making the OQE Group so much fun to be apart of.

To the Defense Advanced Research Projects Agency (DARPA), for supporting me through a National Defense Science and Engineering Graduate Fellowship as well as the DARPA-OAWG Program – life is much easier with funding (or so I've been told).

To Amil Patel and Kerry Cheung, my best friends, for providing voices of reason through the years. They could always be counted on when needed, whether it be for serious life discussions, or just for some light-hearted banter.

To my family (my ever-growing family – hello Sophia, Ella, Edward, Audrey, ...), Papa and Mama Chao (whose sacrifices will forever be appreciated), Papa and Mama Wong, Sisters Evelyn and Lydia and Darice and Emily, Brothers Patrick and Ben and Jason. Thanks for being so supportive, so encouraging, and so understanding through the years.

And finally, to my incredibly loving wife Karen. By my side every step of the way, pushing (sometimes carrying) me forward whenever it seemed like I was stuck in neutral. Thanks for helping me reach the finish line. I can't wait for what's ahead...

Thank you...

Contents

List of Figures

Acronyms

AC	autocorrelation trace
A/D	analog-to-digital
AOFS	acousto-optic frequency shifter
AOM	acousto-optic modulator
APD	avalanche photodiode
APM	additive-pulse mode-locking
AR	anti-reflection
ASE	amplified spontaneous emission
AWG	arrayed waveguide grating
BJT	bipolar junction transistor
CPA	chirped-pulse amplification
CW	continuous-wave
DC	direct current
DCF	dispersion compensating fiber
DFG	difference frequency generation
DSF	dispersion shifted fiber
EDF	erbium-doped fiber
EDFA	erbium-doped fiber amplifier
EDFL	erbium-doped fiber laser
FDTD	finite-difference time-domain
FMLL	fundamentally mode-locked laser
FP/FPI	Fabry-Perot interferometer
FSR	free-spectral range
FWHM	full-width at half-maximum
GDD	group delay dispesion

GVD	group velocity dispersion
GT/GTI	Gires-Tournois interferometer
HMLL	harmonically mode-locked laser
HNLF	highly nonlinear fiber
HWP	half-wave plate
IAC	interferometric autocorrelation
IR	infrared
ISO	isolator
KLM	Kerr-lens mode-locking
MFD	mode-field diameter
MFL	mode-locked fiber laser
MZ/MZI	Mach-Zehnder interferometer
NA	numerical aperture
NPE	nonlinear polarization evolution
NPR	nonlinear polarization rotation
OAWG	optical arbitrary waveform generation
P-APM	polarization additive-pulse mode-locking
PBS	polarization beam splitter
PCF	photonic crystal fiber
PI	proportional-integral
PID	proportional-integral-derivative
PLL	phase-locked loop
PM	polarization-maintaining
PPLN	periodically-poled lithium niobate
QWP	quarter-wave plate
RIN	relative intensity noise
RF	radio frequency
SA	saturable absorber
SBR	saturable Bragg reflector
SCG	supercontinuum generation
SHG	second harmonic generation

SMF	single-mode fiber
SNR	signal-to-noise ratio
SPM	self-phase modulation
SRS	stimulated Raman scattering
SS	self-steepening
TE	transverse electric
TM	transverse magnetic
TOD	third-order dispersion
TPA	two photon absorption
UV	ultraviolet
VCO	voltage-controlled oscillator
WDM	wavelength division multiplexer

Chapter 1

Introduction

Mode-locked lasers, which date back to shortly after the invention of the laser, produce a periodic train of ultrashort optical pulses at their output, typically femtoseconds to picoseconds in duration [1-4]. For years, this time-domain picture of mode-locked lasers was the basis for much of their use in applications. Recently, a significant shift in the applications of mode-locked lasers based on their time-domain behavior to those based on their frequency-domain behavior has taken place as advancements in laser technology have made ultra-precise stabilization of the frequency spectra of these mode-locked lasers possible[1].

The frequency spectrum of a mode-locked laser consists of an ultrabroad set of discrete, evenly-spaced, ultrasharp lasing longitudinal modes – known as frequency comb lines. Once stabilized, this broadband set of "known" frequencies becomes an important enabling technology for experiments in many branches of physics, chemistry, and biology. In particular, the optical frequency comb has revolutionized the field of frequency metrology, dramatically simplifying and improving the accuracy of its measurements. Before optical frequency combs, frequency metrology relied on the precise radio and microwave frequencies (RF) attained from stable atomic and molecular transitions, such as that of the ^{133}Cs transition used in the most precise atomic clocks today, to measure unknown frequencies with the highest achievable accuracy. Harmonic frequency chains were constructed in the late 1960's to produce multiples (or

[1] Most notably, a robust process for controlling the carrier-envelope phase slip of a mode-locked laser's output pulse train was developed – the importance of this development was recognized by the 2005 Nobel Prize in Physics [5,6].

harmonics) of these stable RF frequencies so that frequencies in the optical regime could also be measured to the same accuracy [7]. This led to a number of significant advances in fundamental physics, such as the determination of the speed of light [8], refinement of the Rydberg constant [9], the Lamb shift [10], and the ratio of proton to electron mass [11], as well as a test of Einstein's relativity theory [12]. It is also responsible for the precise measurement of several important atomic transition frequencies, such as that of the Hydrogen 1s-2s transition which has been accurately determined to 13 significant digits [13]. Despite its many contributions, harmonic frequency chains are now obsolete – replaced by the optical frequency comb.

Optical frequency combs first found use as the "gears" of optical atomic clocks [14], but before long, their importance became known for applications ranging from the frequency metrology experiments described above to laser-based precision spectroscopy [15], the generation of attosecond pulses [16], molecular fingerprinting [17], breath analysis [18], etc. More recently, a host of new applications have emerged requiring frequency combs with repetition rates in the GHz regime – applications which include high-speed photonic analog-to-digital conversion (EPIC) [19], high-resolution astronomical spectrograph calibration for more extensive space exploration (Astro-Comb) [20], and in particular, optical arbitrary waveform generation (OAWG) [21,22].

Treating mode-locked lasers in terms of frequency combs has led to the idea of synthesizing optical pulses, or more generally, developing an optical arbitrary waveform generator. A periodic pulse train can be converted into any arbitrary waveform provided that its individual frequency components can be independently controlled in both amplitude and phase at a rapid enough rate. Our proposed approach, as depicted in Fig. 1-1, requires the separation of frequency comb lines so that each can be sent into its own dedicated integrated amplitude/phase modulator before being recombined to form the arbitrary optical frequency comb. For truly arbitrary waveform generation, the modulation of these individual frequency components must be performed at the repetition rate of the input pulse train[2].

In the proposed scheme, arrayed waveguide gratings (AWG) handle both the separation and recombination of the frequency comb lines, and Mach-Zehnder configured modulators control their amplitude and phase. Since AWGs are limited in practice to resolution $\geq$10 GHz [25], this

[2] Other OAWG implementations exist based on spatial pulse shaping techniques using either liquid crystal modulators [23] or acousto-optic modulators [24]. These techniques, however, are too slow for modulation at the required pulse repetition rates.

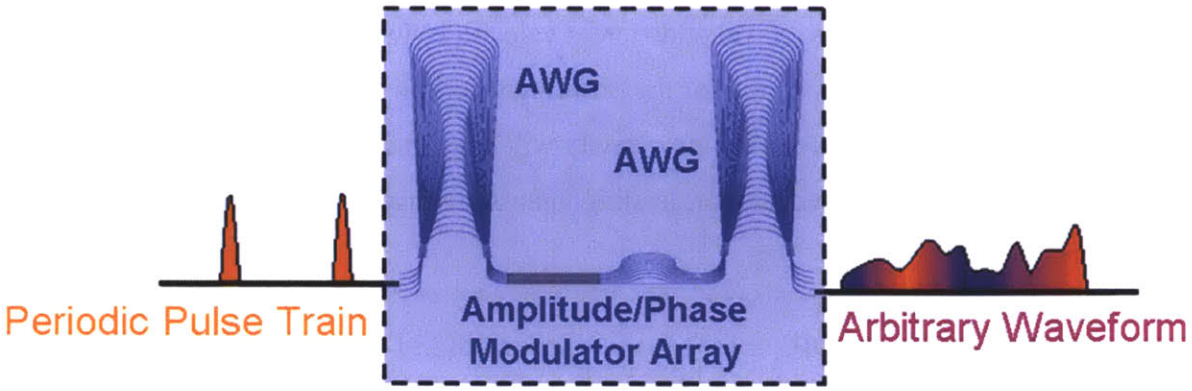

Figure 1-1: Optical Arbitrary Waveform Generation. A periodic pulse train can be transformed into any arbitrary waveform if its discrete frequency content can be separated, modulated in both amplitude and phase, and then recombined. An integrated approach to OAWG using arrayed waveguide gratings (AWGs) for frequency comb separation and recombination, and an amplitude/phase modulator array, is depicted.

imposes constraints on the frequency comb required for OAWG[3]. Namely, the frequency comb lines must be spaced by the same ≥10 GHz constraint.

1.1 The Frequency Comb

In order to better describe the central problem concerning the work conducted in this thesis, more detailed description of the frequency comb and its various components are needed. At the source of a frequency comb is a mode-locked laser. So to begin, let's start with the time-domain picture of a mode-locked laser's output pulse train, as depicted in Fig. 1-2(a). The series of pulses are periodic with period t_{rep}, where t_{rep} is related to the laser cavity by

$$t_{rep} = \frac{l_c}{v_g} \tag{1.1}$$

l_c is the length of the laser cavity, and v_g is the group velocity (i.e. the velocity at which the pulse propagates).

Each pulse is made up of an underlying carrier wave (with frequency ω_c) shaped by an envelope. Notice that in each of the pulses depicted, the peak of the envelope does not correspond to one of the peaks in the carrier wave. This shift in peaks is known as the carrier-

[3] Note that the proposed amplitude/phase modulators have a demonstrated operating range up to 40 GHz [26].

envelope phase shift (Φ_{ce}) and is attributed to propagation in a dispersive medium, causing the pulse envelope and carrier wave to travel at different velocities. In the above figure, dispersion in the laser cavity is directly responsible for the differing Φ_{ce} from pulse to pulse. That is, each successive pulse directly output from the laser cavity will have traveled around the dispersive laser cavity once more than its predecessor, leading to an additional carrier-envelope phase shift of $\Delta\Phi_{ce}$, where

$$\Delta\Phi_{ce} = \left[\left(\frac{1}{v_g} - \frac{1}{v_p}\right) l_c \omega_c\right] \bmod(2\pi) \tag{1.2}$$

v_g is the group velocity, v_p is the phase velocity, l_c is the length of the laser cavity, and ω_c is the frequency of the carrier wave. Note that we only care about the phase slip modulo 2π.

We now move to the frequency domain to finish off the description. The frequency-domain picture of a mode-locked laser's output is obtained by taking the Fourier Transform of the periodic pulse train shown in Fig. 1-2(a). We can represent the pulse train mathematically as follows

$$E(t) = \hat{E}(t)\cos(\omega_c t + \Phi_{ce}) \tag{1.3}$$

where $\hat{E}(t)$ is the periodic train of pulse envelopes, and can be decomposed into

$$\hat{F}(t) \otimes Comb_{t_{rep}}(t) \tag{1.4}$$

where $\hat{F}(t)$ is just the envelope of one pulse and $Comb_{t_{rep}}(t)$ is a train of delta functions evenly-spaced by t_{rep}. Thus,

$$E(t) = \left(\hat{F}(t) \otimes Comb_{t_{rep}}(t)\right)\cos(\omega_c t + \Phi_{ce}) \tag{1.5}$$

Notice that the pulse-to-pulse carrier-envelope phase slip ($\Delta\Phi_{ce}$) is accounted for in the above expression when ω_c is not restricted to be a multiple of the pulse train's repetition rate (or equivalently, not restricting the period of the carrier wave's oscillation to be an exact multiple of the pulse train's period t_{rep}). Eq. (1.5) allows for the Fourier Transform of $E(t)$, $E(\omega)$, to be taken in steps. The Fourier Transform of $\hat{F}(t)$, $\hat{F}(\omega)$, is pulse-shaped with width inversely proportional to the width of $\hat{F}(t)$. The Fourier Transform of $Comb_{t_{rep}}(t)$ is $Comb_{f_{rep}}(\omega)$, where f_{rep} is

inversely proportional to t_{rep} (i.e. f_{rep} is the repetition rate of the mode-locked laser). Next, employing two well-known Fourier Transform identities gives

$$\hat{F}(t) \otimes Comb_{t_{rep}}(t) \xleftrightarrow{F.T.} \hat{F}(\omega) \cdot Comb_{f_{rep}}(\omega) \tag{1.6}$$

and

$$\left(\hat{F}(t) \otimes Comb_{t_{rep}}(t)\right) \cos(\omega_c t + \Phi_{ce}) \xleftrightarrow{F.T.} \hat{F}(\omega - \omega_c) \cdot Comb_{f_{rep}}(\omega - \omega_c) \tag{1.7}$$

Thus,

$$E(\omega) = \hat{F}(\omega - \omega_c) \cdot Comb_{f_{rep}}(\omega - \omega_c) \tag{1.8}$$

In words, the frequency spectrum of a mode-locked laser's output consists of delta functions (i.e. discrete frequencies) evenly-spaced by f_{rep} and shaped by $\hat{F}(\omega)$, the envelope of the optical

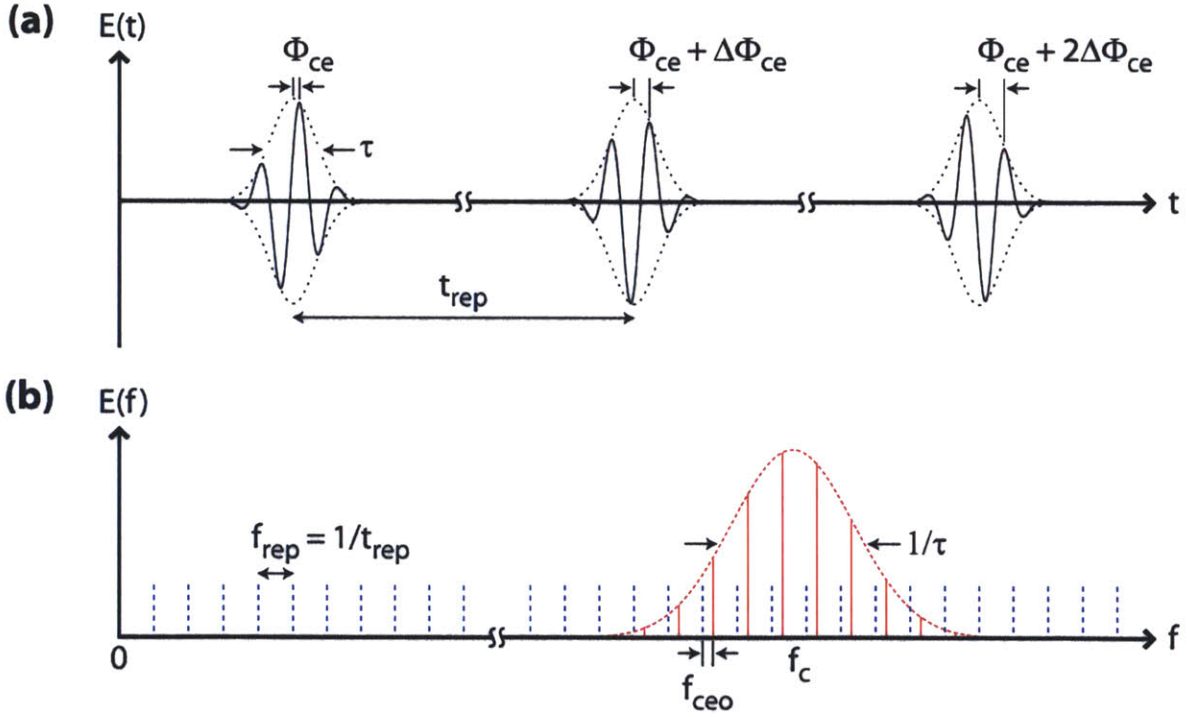

Figure 1-2: Mode-locked laser output. (a) Time domain description. Pulses consist of a carrier wave (black-solid) shaped by an envelope (black-dotted). Intracavity differences in group and phase velocity leads to a pulse-to-pulse carrier-envelope phase slip, $\Delta\Phi_{ce}$. (b) Frequency domain description. A periodic set of discrete frequencies (red-solid) separated by the laser repetition rate f_{rep}, centered at the carrier wave frequency f_c, and shaped by the Fourier Transform of the pulse envelope (red-dotted). The carrier-envelope phase slip corresponds to a shift of the frequencies from the repetition rate harmonics (blue-dotted) by an amount f_{ceo}.

spectrum. Additionally, the comb is shifted so that it is centered at the carrier frequency, ω_c. Since ω_c is not a multiple of f_{rep} (unless $\Delta\Phi_{ce} = 0$), the pulse-to-pulse carrier-envelope phase slip corresponds to an offset of the comb from the harmonics of repetition rate.

The full picture of the frequency spectrum of a mode-locked laser has now been described, and is depicted in Fig. 1-2(b). The optical frequencies of the comb lines can be written as

$$f_n = nf_{rep} + f_{ceo} \tag{1.9}$$

where f_{ceo} is related to $\Delta\Phi_{ce}$ by

$$f_{ceo} = \frac{\Delta\Phi_{ce}}{2\pi} \cdot f_{rep} \tag{1.10}$$

In the absence of active stabilization, f_{rep} and f_{ceo} would be free to drift due to a host of environmental disturbances, leading to changes in the laser's cavity length, refractive index, and nonlinear dynamics. Eq. (1.9) states that we can fully stabilize the locations of the comb lines by stabilizing two parameters, f_{rep} and f_{ceo} – this results in a frequency comb. Techniques for achieving this at GHz repetition rates will be described in this thesis.

1.2 Techniques for Self-referenced 1.5 μm Fiber Frequency Combs at GHz Repetition Rates

To re-emphasize, the stabilization of two parameters, f_{rep} and f_{ceo}, transforms the output of any mode-locked laser into a frequency comb. Stabilization of the repetition rate, f_{rep}, is generally accomplished using RF photodetection and locking to an RF reference oscillator. This requires nothing more than a high-speed photodiode and a phase-locked loop. Stabilization of the carrier-envelope offset frequency, f_{ceo}, on the other hand, requires more processing as RF techniques are not nearly fast enough for its direct detection. Measurement of f_{ceo} is therefore typically done using a self-referencing technique requiring an entire octave of spectrum[4] [28]. This technique is described mathematically as follows:

[4] If an octave-spanning supercontinuum is not attainable, variations of the process can be used to detect f_{ceo}, reducing the burden on SCG. One such variation is beating the 2nd and 3rd harmonics of the high and low frequency sections of the spectrum, respectively; i.e.

$$3f_n - 2f_{\frac{3}{2}n} = 3\left(nf_{rep} + f_{ceo}\right) - 2\left(\frac{3}{2}nf_{rep} + f_{ceo}\right) = f_{ceo}$$

which requires only ~60% of an octave [27].

$$2f_n - f_{2n} = 2(nf_{rep} + f_{ceo}) - (2nf_{rep} + f_{ceo}) = f_{ceo} \quad (1.11)$$

where n is an integer indicating mode number. That is, f_{ceo} is obtained by doubling the low frequency end of the octave-spanning spectrum, then subtracting from it the high frequency end of the same spectrum. Once detected, a phase-locked loop stabilizes f_{ceo}.

Self-referenced frequency combs were first introduced in the late 1990s, based on Kerr Lens Mode-locked Ti:Sapphire solid-state laser systems [29]. Much of the research has continued to center around these superior performing systems, as Ti:Sa offers the broadest gain bandwidth of all known laser mediums. In fact, careful control of cavity dispersion through the use of double-chirped mirrors has led to the generation of sub-two-cycle pulses and an octave-spanning spectrum directly out of the laser [30]. Post-processing (e.g. additional amplification, compression, and/or supercontinuum generation) is therefore not necessary for f_{ceo} detection, making frequency comb generation relatively straightforward. Systems of this nature have been demonstrated to repetition rates of 2GHz [31]. At even higher repetition rates, generating octave-spanning spectrum directly out of the laser becomes constrained by the lower intracavity pulse energies, which scale inversely with repetition rate – this is the case with the 10GHz Ti:Sa laser demonstrated by Bartels et al. [32]. The pulses out of that laser, however, are still sufficiently short and sufficiently energetic so that an octave of supercontinuum can be generated in photonic crystal highly nonlinear fiber without additional amplification and compression. Thus, frequency comb generation with solid-state Ti:Sa laser systems, even under constrained conditions, is relatively straightforward. The 10GHz Ti:Sa frequency comb is the highest repetition rate frequency comb reported to date.

Recently, frequency combs based on fiber architectures have become attractive alternatives to their more traditional solid-state counterparts due to their compact and robust operation. Fiber-based systems, however, face several additional obstacles to frequency comb generation. Specifically, octave-spanning laser spectra are not possible due in part to the significant amount of dispersion inherent with fiber cavities. As a result, the fiber laser output generally requires additional stages of amplification and compression before it can be sent into HNLF for octave-spanning supercontinuum generation. These additional steps make frequency comb generation in fiber systems more difficult as external amplification and compression can easily lead to pulse distortions (and even pulse breakup) if proper measures aren't taken to avoid excessive nonlinearities. Even then, reductions to pulse quality cannot be completely avoided.

Furthermore, the phase coherence of the generated continuum is extremely dependent on pulse energy and duration, both of which are inferior (even after the additional stages of amplification and compression) to the pulses generated out of the Ti:Sa. For these reasons, fiber-based frequency combs weren't developed until 2004 [33], at which time, advances in amplification/compression technologies as well as novel HNLFs allowing supercontinuum generation at lower pulse energy and duration requirements made possible self-referenced f_{ceo} detection suitable for stabilization. It is also for these reasons that fiber frequency combs based on Ytterbium and Erbium platforms have thus far been limited to 1GHz and 300MHz, respectively [34,35]. Of these two fiber platforms, Ytterbium frequency combs centered at 1μm are generally better performing because the higher and more efficient pump absorption compared to Erbium allows for greater power scalability. This means shorter lengths of gain fiber (i.e. shorter laser cavities) can be used to produce sufficient intracavity pulse energies for mode-locking. This also means that post-laser amplification is less demanding. For example, multi-Watt levels can be readily attained with Yb-based fiber amplifiers [36], while Er-based fiber amplification has generally been limited to less than a Watt.

Despite their shortcomings, Erbium-based frequency combs which are centered around the 1.5μm wavelength band are extremely important from an application perspective, due particularly to their direct applicability to telecom systems. The efforts of this thesis will therefore focus on overcoming the many challenges involved with achieving self-referenced GHz repetition rate fiber frequency combs at 1.5μm.

1.3 Thesis Outline

The rest of this thesis is outlined as follows – Chapter 2 describes our fundamental and harmonic mode-locking approaches (and results) for 1 GHz repetition rate oscillators; Chapter 3 details our high-power femtosecond-pulse amplification/compression system which produces 2nJ, 95fs pulses at 1 GHz repetition rates; Chapter 4 reviews our octave-spanning supercontinuum generation studies; Chapter 5 presents our f_{ceo} beat detection and stabilization results, as well as our DFG results for optically-stable frequency combs; Chapter 6 summarizes our repetition rate multiplication experiments for scaling up 1 GHz frequency combs to 10 GHz; Chapter 7 concludes the thesis and discusses future research.

Chapter 2

GHz Repetition Rate Lasers*

There are three general approaches to increasing the repetition rate of mode-locked lasers. The most intuitive and straightforward of the three is a simple reduction of the laser cavity length, since f_{rep} is inversely proportional to the round-trip optical length of the cavity l_c (as given in Eq. 1.1). However, there are physical limitations to how short one can make the laser cavity. For example, a 1 GHz mode-locked fiber laser corresponds to l_c = 20 cm and a 10 GHz mode-locked fiber laser corresponds to l_c = 2 cm (both assuming n = 1.5), which would be extremely difficult given current Erbium fiber technologies.

A second approach is commonly referred to as harmonic mode-locking. A harmonically mode-locked laser has multiple pulses running around the laser cavity at any particular point in time. Thus, the more pulses in the laser cavity, the higher the repetition rate of the laser's output pulse train, just as long as the pulses in the laser cavity are spaced apart evenly. Generally, a harmonically mode-locked laser needs to satisfy two requirements for proper functionality. It needs to be pumped with enough energy to support the multiple pulses in the cavity and it needs a process for sorting the pulses so that they are spaced apart evenly. It does not, however, run into the physical size limitations fundamentally modelocked lasers face when it comes to high repetition rates.

* With contributions from Hyunil Byun, Jonathan Morse, Michelle Sander

The last approach to achieving high repetition rates is to perform repetition rate multiplication using an external cavity, most commonly a Fabry-Pérot (FP). A FP acts as a filter in the frequency domain, with sharp transmission resonances evenly spaced by the FP's free spectral range (FSR). Frequency multiplication results when the FP's FSR is an exact multiple of the laser's repetition rate, f_{rep}. There is a limit to this multiplication, however, as higher factors require higher-Q cavities to ensure that all unwanted frequencies are properly filtered out. We discuss the first two of these approaches here, as they relate to the oscillator. The last approach, which is a post-oscillator implementation, is discussed in a later chapter (Chapter 6).

2.1 Fundamental Modelocking at GHz Repetition Rates

A number of fundamentally modelocked laser configurations were investigated for scaling to GHz repetition rates. Ring cavity designs offered the potential for shorter pulses through P-APM, whereas scaling to higher repetition rates was more feasible with linear cavity assemblies. Results from both approaches are presented.

2.1.1 Ring Cavity 200-300 MHz Erbium Fiber Lasers based on P-APM

Numerous designs for ring cavity fiber lasers operating in the soliton, stretched-pulse, and similariton regimes have been proposed and implemented over the years [37-39]. Pulses with 50fs durations and 5nJ energies have been generated directly out of these lasers. The repetition rates of these systems, however, have generally stayed below 80 MHz, with few exceptions [40], mainly due to the physical limitations associated with scaling down the cavity.

A 75 MHz repetition rate fiber laser using similar ring cavity concepts was developed by previous members of my research group to study the extent to which these configurations could be scaled up in rep rate [41]. This laser, whose setup is shown in Fig. 2-1, operates in the soliton regime with a net cavity dispersion of -52000 fs^2. A fiber section spanning 250 cm, consisting of 50 cm of highly-doped 80 dB/m Liekki gain fiber, 20 cm of HI1060 fiber, 180 cm of SMF-28 fiber, along with a 15 cm free-space section make up the cavity. The 50 cm length of gain fiber was optimal for 500 mW pumping by a semiconductor laser diode at 974 nm. P-APM is implemented through quarter- and half-waveplates in combination with a polarizing

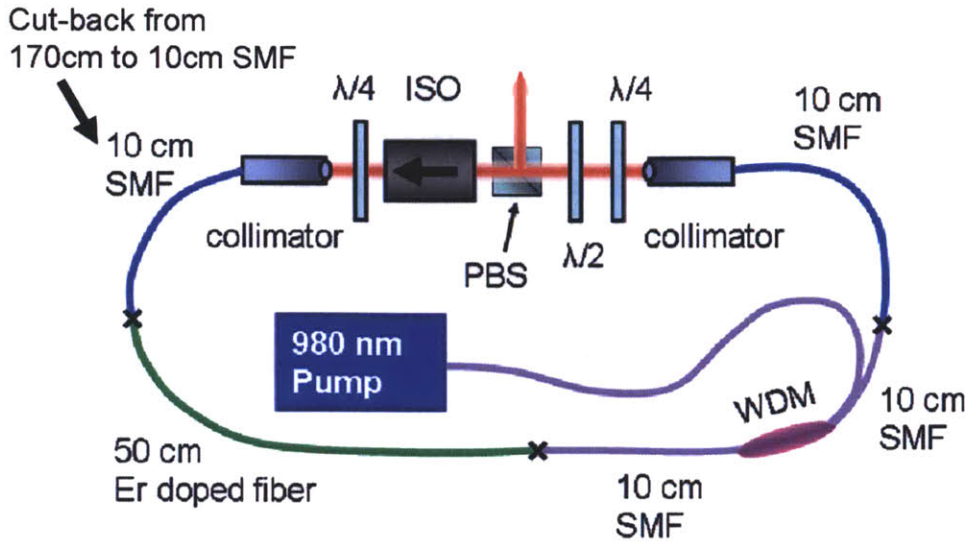

Figure 2-1: Soliton fiber laser configured in a ring cavity, and mode-locked using P-APM. A systematic cut-back of the SMF section from 170cm down to 10cm results in a 200MHz repetition rate.

beamsplitter, which is also used to generate the output. A free-space polarizing isolator, with its polarization axis aligned to that of the beamsplitter, is included to ensure unidirectional operation.

Modelocking was obtained through optimization of the quarter- and half-waveplates, generating the optical spectrum (pink curve) shown in Fig. 2-2. A systematic reduction of the SMF-28 fiber length caused increases of repetition rate to 94 MHz, 120 MHz, and finally 200 MHz. At this point, limitations in pump power prevented further cavity reduction, as fundamental modelocking at 200 MHz required 475 mW of pump power. At these pump levels, an output power of 33.6 mW was achieved, which at 200 MHz corresponds to 168 pJ output pulses. Optical and RF spectra of these output pulses are shown in Fig. 2-3. The 1565 nm centered optical spectrum has a bandwidth of 19.3 nm, indicating transform-limited hyperbolic secant pulse durations of 130 fs. An interferometric autocorrelation was taken to confirm this.

The resonant sidebands seen in the optical spectra, known as Kelly sidebands, are prevalent in soliton fiber lasers [42]. The locations of these sidebands in the optical spectrum depend on the laser's cavity length, average net dispersion, and pulse width [43]. Decreasing the length of the cavity increases the spacing between the Kelly sidebands, allowing for wider optical spectra (and shorter pulses), as is observed with this laser.

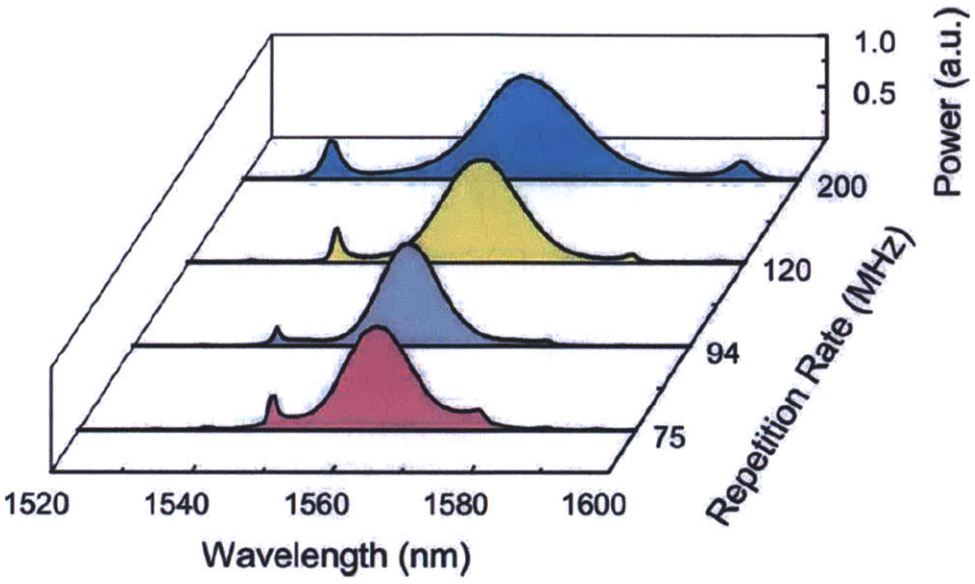

Figure 2-2: Optical spectrum out of the ring cavity soliton fiber laser as the repetition rate is increased from 75MHz to 200MHz. Increases to repetition rate push out the Kelly sideband instabilities leading to greater optical bandwidths.

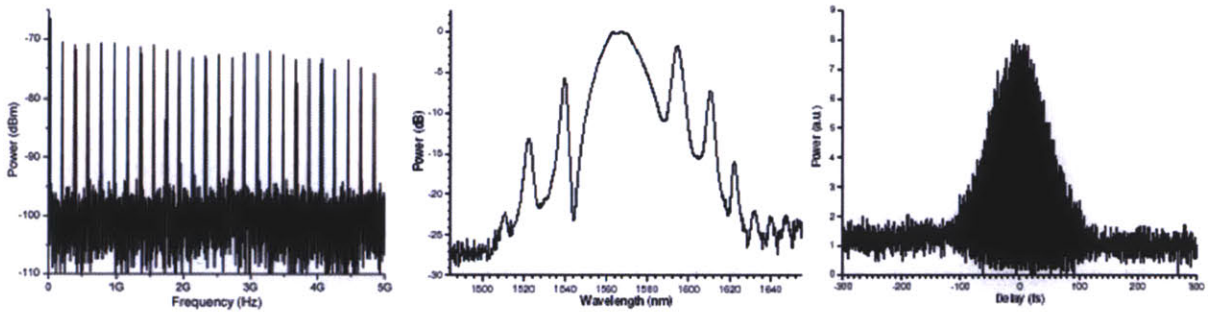

Figure 2-3: Ring cavity soliton fiber laser output characteristics. From left to right: The RF spectrum (200MHz repetition rate), optical spectrum (19.3nm FWHM bandwidth), and interferometric autocorrelation (130fs pulse duration).

The scaling of this laser to even higher repetition rates could have been possible with more pumping capability, and/or more highly absorbing gain fiber. Anomalous dispersion gain fiber with higher doping levels could not be commercially obtained, but increased pumping with two polarization beam-combined pump diodes allowed for successful modelocking of a similarly configured stretched-pulse fiber laser at 300 MHz [44]. To date, this is the highest repetition rate fiber laser using a ring cavity construction. It's unlikely that further improvements will lead to anything more than incremental increases in repetition rate moving forward.

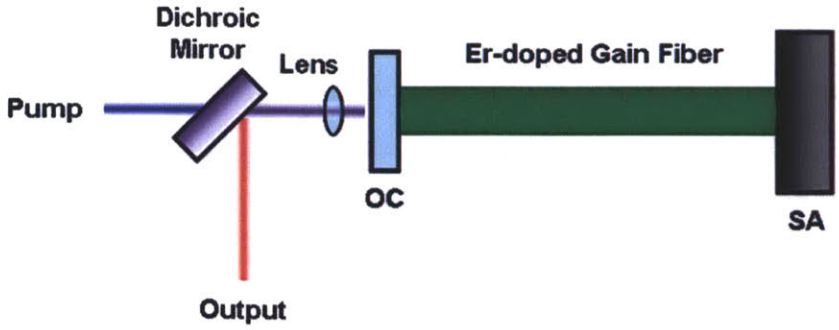

Figure 2-4: Schematic of a linear cavity fiber laser. The Er-doped gain fiber is sandwiched between an output coupler (OC) and a saturable absorber (SA) used for initiating mode-locking. The dichroic mirror separates signal from pump.

2.1.2 Linear Cavity 1 GHz Erbium Fiber Lasers based on SBR Modelocking

To reach GHz repetition rates, two important changes were made to the design decisions described in the previous section. The first was to go to a linear cavity configuration. Doing so makes implementation of short cavities more feasible, and additional scaling more straightforward. The use of saturable absorption modelocking, rather than P-APM, further simplifies cavity design and relaxes intracavity pulse energy requirements for modelocking.

2.1.2.1 Linear Cavity Configuration

A linear cavity configured modelocked laser can be as simple as the depiction in Fig. 2-4, which consists of a piece of gain fiber sandwiched between an output coupler mirror on one end, and a saturable absorber on the other. With highly-doped gain fibers and strong pumping, cavity lengths from 10 cm (corresponding to 1 GHz) to as short as ~3 cm (3 GHz) have been demonstrated in our laboratories [45]. Such a configuration has also generated 20 GHz pulse trains, though with reduced pulse quality [46]. However, problems with the long-term stability of such lasers, in addition to pulse-to-pulse polarization rotation concerns, need to be addressed.

2.1.2.2 SBR Modelocking

SBRs are saturable absorbers used in reflection (via a Bragg mirror stack). They initiate modelocking by imparting an intensity-dependent loss, i.e. reduced losses at higher intensities due to saturation of the saturable absorber, forcing the laser to operate in a modelocked state as this corresponds to the least loss state. This saturable absorption can be designed for different intensity levels, typically requiring less intracavity pulse energies compared to what's required for P-APM. In addition, P-APM relies on nonlinear polarization rotation, which depends on fiber length as well as pulse energy. This means that shorter fiber lengths require more pulse energy, making scaling to higher repetition rates that much more difficult. SBRs, in contrast, depend only on pulse energy. SBR modelocking threshold should therefore remain the same so long as pulse energies can be maintained with shorter cavities.

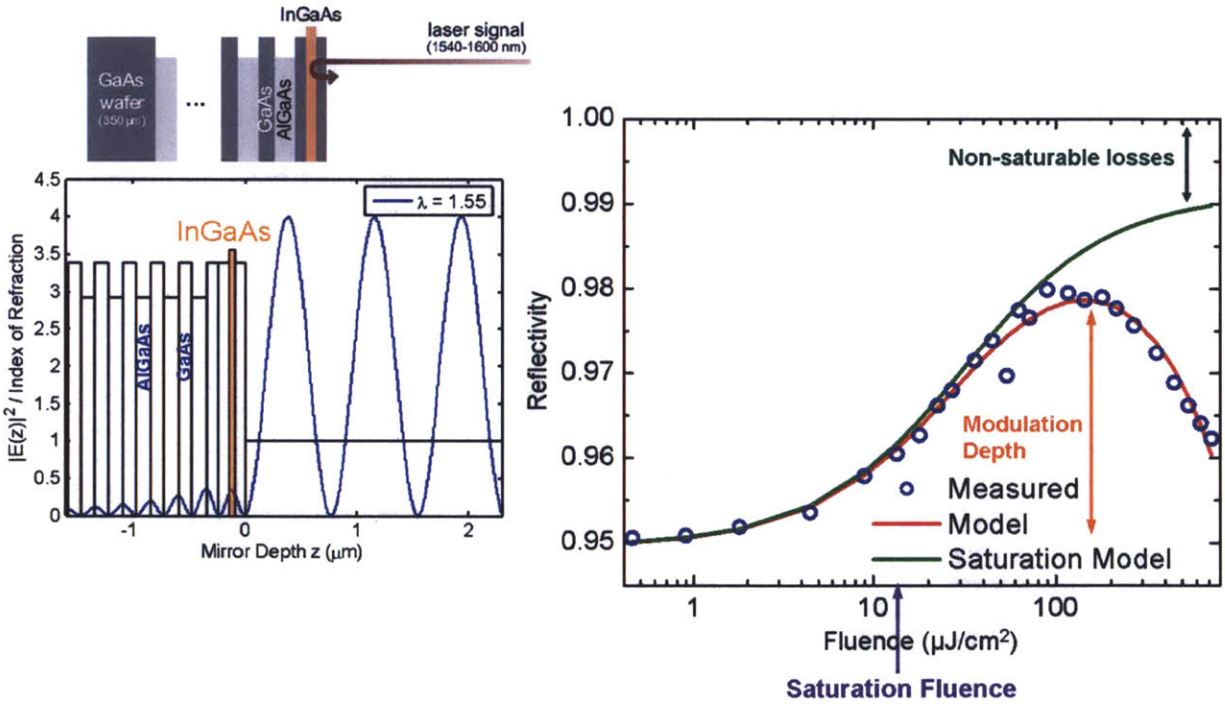

Figure 2-5: Typical saturable bragg reflector (SBR) characteristics. (a) SBR consists of a saturable absorption layer (InGaAs) embedded in a 22-layer bragg stack (alternating quarter-wave layers of AlGaAs and GaAs). The InGaAs layer is placed at a peak of the reflected electric field. (b) SBR reflectivities at different incident intensities. Saturation at high intensities (saturation fluence) leads to increased reflectivities before losses due to two-photon absorption take over to again reduce overall reflectivity. The modulation depth provides a measure of the difference in saturable and non-saturable losses.

A typical SBR layer stack[5], along with the electric field distribution of a reflected wave, is shown in Fig. 2-5. It consists of a saturable absorption layer, in this case InGaAs, and 22 quarter-wave layers of alternating AlGaAs and GaAs making up the Bragg mirror stack. The thickness of the saturation absorption layer, as well as its location within the Bragg stack, are design parameters which determine SBR performance, many of which are illustrated in the reflectivity plot also shown in Fig. 2-5. The SBR's saturation fluence represents the pulse energy density corresponding to onset of saturable absorption. At high enough intensities, two-photon absorption becomes significant, and causes a reduction in reflectivity (and thus the downturn in the reflectivity curve with higher intensities). All SBRs possess some non-saturable loss, as reflectivities never reach 100%, and the modulation depth refers to the extent of the intensity-dependent reflectivity change, ΔR. The SBR's recovery time, typically on the picosecond timescale, is measured through pump probe experiments [47].

Two different SBR samples were used in the following experiments, one grown in-house (referred to as VA86) and the other commercially available through Batop. Both SBRs were measured for their reflectivity profile and recovery time, the results presented in Fig. 2-6. VA86

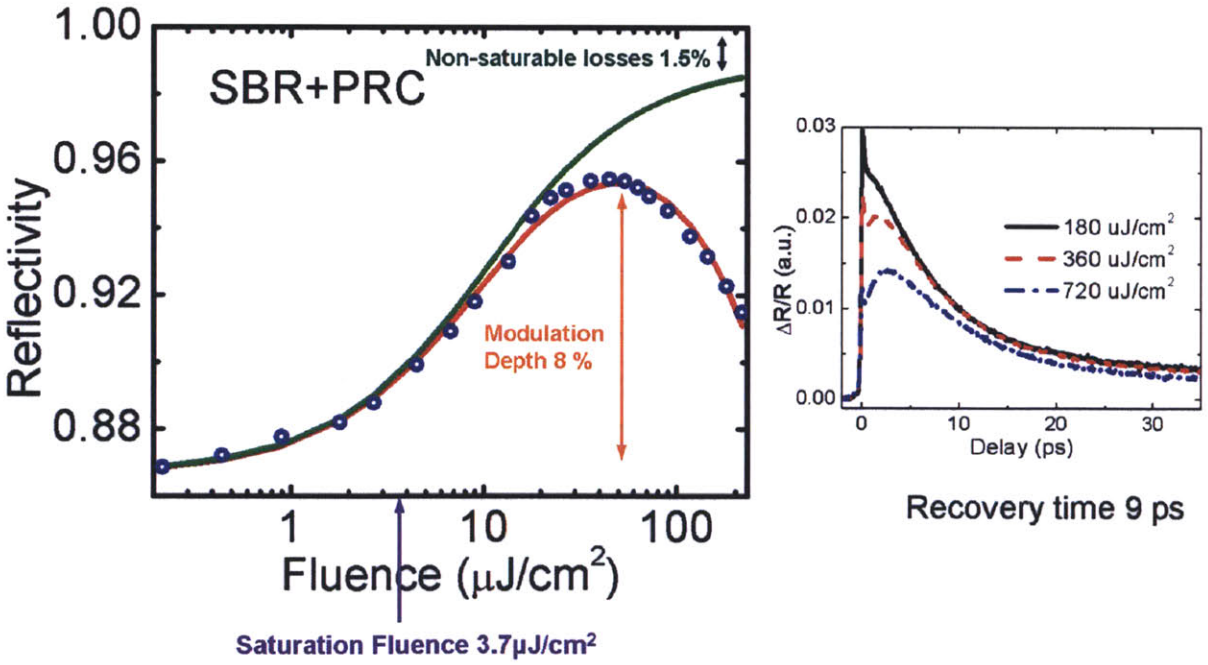

Figure 2-6: VA86 SBR+PRC measurements to determine its saturable and non-saturable losses (13.1%,1.5%), saturation fluence (3.7μJ/cm^2), modulation depth (8%), and recovery time (9ps).

[5] SBR design courtesy of Michelle Sander. SBR growth courtesy of Gale Petrich.

possesses saturable and non-saturable losses of 13.1% and 1.5% respectively, a saturation fluence of 3.7μJ/cm^2, a modulation depth of 8%, and a recovery time of 9ps. The Batop SBR possesses 35%, 14%, 20μJ/cm^2, 21%, 2ps (saturable losses, non-saturable losses, saturation fluence, modulation depth, recovery time).

2.1.2.3 1 GHz Oscillator with Free-space Section

The laser setup depicted in Fig. 2-4 had a multitude of issues that needed resolving before it could even potentially be considered for a frequency comb – issues which include SBR burning and its affect on laser stability, amplitude modulated output pulses and polarization sidebands arising from a periodic polarization rotation at the laser output, as well as what was perceived to be an inability to adjust for repetition rate fluctuations.

Each of these issues could be remedied with the addition of a free-space section between the gain fiber and SBR. Doing so allows for the SBR to be mounted on a piezo-transducer and adjustments to cavity length made with negligible incurred loss. SBR burning, which is at least partially attributed to thermal heating from being in contact with the hot gain fiber core[6], hasn't been completely eliminated, but it's been drastically reduced. Moving the SBR out of contact with the gain fiber helps tremendously, as does free-space air cooling and heat dissipation.

A schematic detailing this particular setup with the free-space section is shown in Fig. 2-7. Instead of butting the gain fiber to the Batop SBR, a set of lenses is used to image the gain fiber output onto the SBR. With the right combination of lenses, a tighter focus can be obtained allowing modelocking to be reached at lower intracavity powers. In this case, a combination of 8 mm and 3 mm focal-length aspheric lenses images the gain fiber's 9.5 μm MFD down to 3.6 μm at the SBR, providing a 7 times higher intensity for the same intracavity pulse energy. The laser now consists of 75mm of 80dB/m Er-doped gain fiber and a free-space section measuring 29mm. The gain fiber is butt-coupled to a 5% dielectric output coupler on one end, and angle-polished on the other end to prevent even the slightest back-reflection from interrupting modelocking operation. A single 980nm semiconductor diode pumps the laser through a 980/1550nm dichroic

[6] Separate experiments were conducted to study the effects of pulse energy on SBR burning. In those experiments, pulses of similar energies and durations were put onto the SBR via butt-coupling to SMF-28 fiber. The MFD of SMF-28 matches that of the Liekki gain fiber, meaning the experiment fairly replicated the intensities incident on the SBR fairly accurately. No burning occurred.

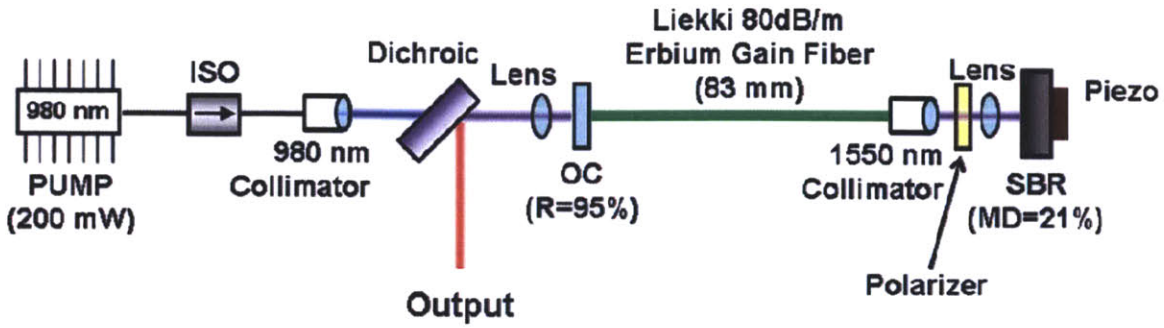

Figure 2-7: GHz repetition rate linear cavity fiber laser with free-space section. The free-space section helps to mitigate SBR burning problems, and allows for the insertion of an intracavity free-space polarizer to eliminate vector soliton behavior as well as a piezo-mounted SBR for repetition rate control. The Batop SBR initiates mode-locking and soliton pulse shaping (-260fs^2 cavity roundtrip dispersion) is used to generate 510fs transform-limited pulses with 2pJ energies.

mirror used to separate signal from pump. Stable modelocking was attained at pump powers above 150mW, with increasing pump leading to progressively shorter and more energetic pulses before the onset of multiple pulsing. At 200mW pump, fundamental modelocking was achieved with output powers of 2mW, corresponding to 2pJ pulse energies.

An estimation of the intracavity roundtrip gain and losses gives an idea of how close we are to operating at projected levels. The gain per pass is estimated to be ~7 mW when pumped at 200 mW[7], and the intracavity loss estimations of 5%, 9%, and 20% correspond to losses from the output coupler, the Batop SBR non-saturable loss, and the loss coupling in-and-out of fiber. These estimations lead to a projected intracavity power of 39.22 mW, which is in good agreement with the experimentally measured value of 40 mW (i.e. 2 mW output power from 5% output coupling).

Fundamental modelocking at a 1.02 GHz repetition rate is verified with the RF spectral trace of the laser output shown in Fig. 2-8a. Without a proper polarization discriminator in the laser cavity, the intracavity pulses are free to take on any polarization, and rotation may not be periodic with every roundtrip. Such behavior, a phenomenon known as vector solitons [48], leads to a periodic polarization rotation in the output pulse train. Any polarization-dependent device will then transform this rotation into an amplitude modulation, causing RF sidebands off the repetition rate and its harmonics. Sidebands of this nature, or any nature, are a problem when

[7] The estimation assumes uniform pumping and gain saturation.

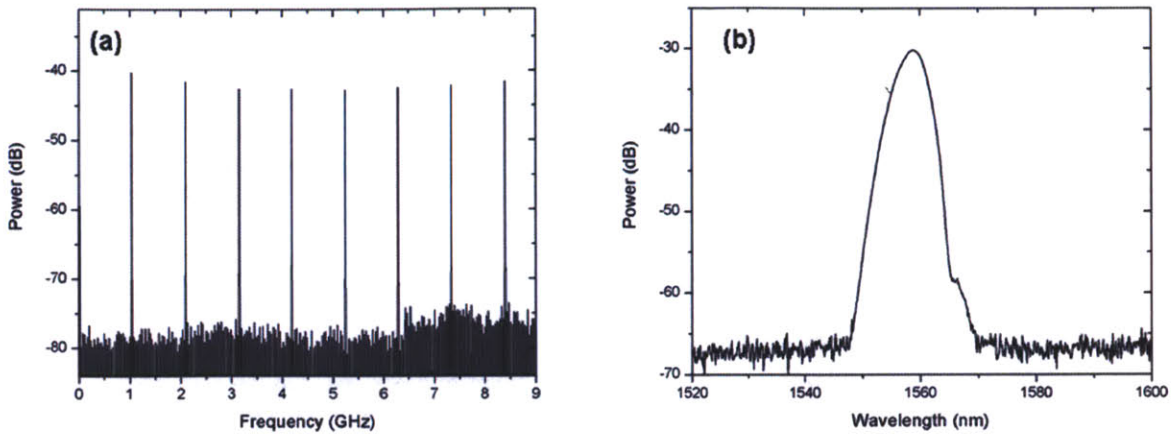

Figure 2-8: Laser output characteristics. (a) RF spectrum confirming clean and stable 1.02 GHz operation. (b) $Sech^2$-shaped optical spectrum with 5nm FWHM bandwidth corresponding to 510fs transform-limited duration pulses.

nonlinear processes are involved. Nonlinear four-wave mixing, for example, can build up these sidebands very quickly, as can be seen in Fig. 2-9. Fig. 2-9a shows the extent of the polarization sidebands after sending the laser output through a polarizer. The sidebands after amplification of the laser output to 65 mW (Fig. 2-9b), and the sidebands after amplification to 2 Watts followed by spectral generation in HNLF (Fig. 2-9c). Not only is there significant amplification of these sidebands after only small levels of amplification (i.e. pulse energies of 65 pJ), there's generation (and amplification) of new sidebands. After significant amplification and nonlinear spectral generation, the sidebands are just as strong as any other signal. Also, nonlinear conversion of amplitude noise to phase noise may be an even bigger problem, as it'll probably prevent phase detection of the carrier-envelope offset frequency.

Fortunately, the free-space section allows for the insertion of a thin-film polarizer into the laser cavity, forcing the polarization of the pulses to follow the same trajectory every roundtrip, thereby eliminating vector soliton behavior. Careful adjustment of the fiber birefringence (i.e. twisting of the gain fiber) allows for the polarizer to be inserted with only 4% roundtrip loss. The results of the laser output (through an external polarizer), after amplification to 65 pJ energies, and after amplification to 2 nJ energies followed with nonlinear spectral generation are shown in Fig. 2-9d-e.

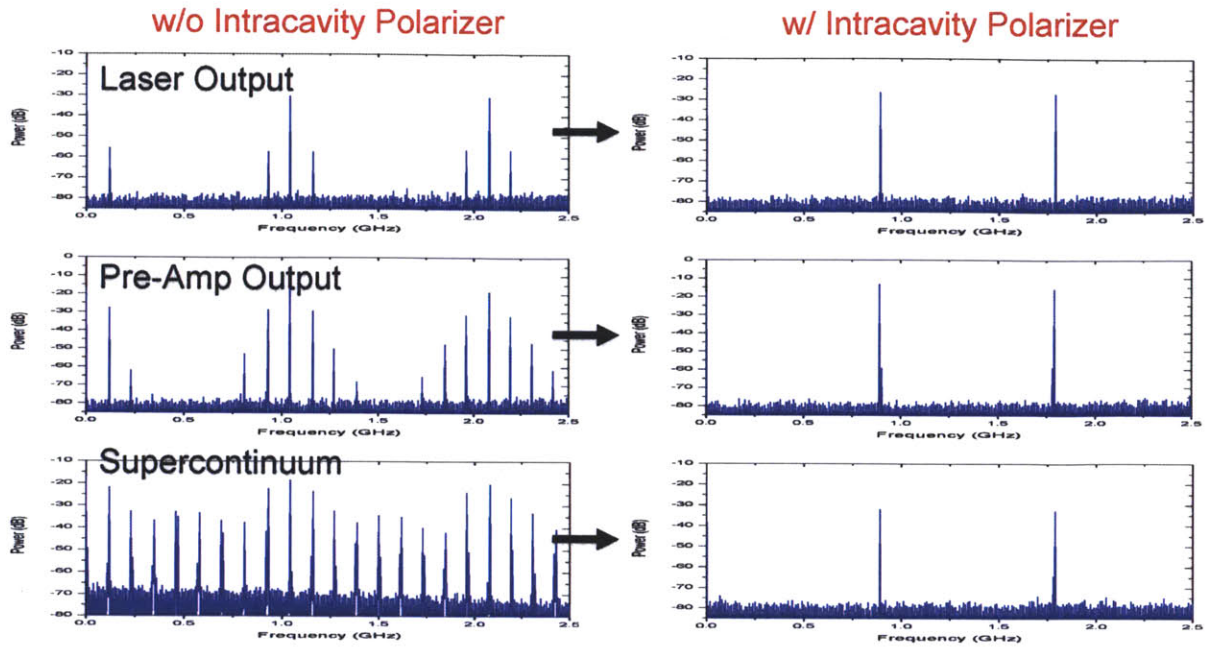

Figure 2-9: Amplitude modulation sidebands due to vector solitons. The AM sidebands detected at the laser output are enhanced (along with the generation of new sidebands) after 18dB amplification. Additional amplification and spectral broadening leads to complete AM sideband fill-in. An intracavity polarizer eliminates vector solitons and its resulting AM sidebands, as evidenced by the RF spectral traces of the laser output, pre-amp output, and supercontinuum output.

The laser operates in the soliton regime based on a calculated total cavity roundtrip dispersion of -260 fs^2. The 1560nm-centered 5nm-wide optical spectrum of the laser output shown in Fig. 2-8b exhibits the requisite $sech^2$-like shape characteristic of soliton spectra, from which we infer transform-limited pulse durations of 510 fs. While still relatively long, these durations are short compared to the response time of the saturable absorber[8], which in this case has a recovery time of 2ps. This is because soliton effects are used to shape and shorten the pulse, as governed by the area theorem [49]:

$$E_p \tau_p = \left| \frac{2\beta_2}{\eta} \right| \tag{2.1}$$

The SBR is still needed to modelock the laser (i.e. it is used to start, and to maintain, modelocking), but pulse shape and duration are independent of SBR dynamics. As a check, the following known values are used ($E_p \approx 40$ pJ, $\beta_2 \approx -19.4$ ps^2/km, $\eta \approx 2.4$ $W^{-1}km^{-1}$) to determine τ_p = 404 fs, corresponding to a pulse duration of 712 fs (compared to the experimentally measured

[8] Proton bombardment can be used to alter SBR recovery time. The VA86 SBRs used in these experiments have been proton bombarded for this very reason.

value of 510 fs). The potential for shorter pulses is possible with higher intracavity pulse energies, and/or more careful management of cavity dispersion and nonlinearity.

2.1.2.4 1 GHz All-fiber Oscillator

Since shorter pulses are desired, the butt-coupled approach outlined at the beginning of this section (Fig. 2-4) is revisited. The lack of a free-space section in this configuration eliminates the dominant losses of the fiber-freespace laser, i.e. the 20% coupling losses from going in-and-out of fiber, and results in increased intracavity pulse energies and shorter pulses. Additionally, a SBR (VA86) with lower non-saturable losses is used to further reduce intracavity losses. On the other end, the bulky and alignment-sensitive pump coupling optics are replaced with a 980/1550 WDM, with the 980/1550 signal port FC/PC connectorized and dielectric-coated for 10% output coupling. This makes the laser completely all-fiber. In addition to being alignment free, benefits to an all-fiber configuration include its compactness (the laser sits on a 4" by 6" breadboard – the smallest we could find) and robustness (more resistant to environmental disturbances, e.g. air currents).

The aforementioned problems with this configuration remain, however – problems that need to be resolved without the inclusion of a free-space section. The following sections detail our solutions and subsequent results.

2.1.2.4.1 SBR Burning Prevention

Our experience with the fiber-freespace laser helped in identifying the main cause for SBR burning in these GHz laser setups – thermal heating from contact with the gain fiber core. The free-space section provided separation between the gain fiber and SBR, which helped tremendously in the prevention of SBR burning. In the all-fiber setup, a similar solution can be implemented. Instead of free-space, a section of passive fiber can be used to separate the gain fiber from SBR. To this end, a 0.6 cm length of SMF-28 fiber was spliced to the Liekki gain fiber. The length was chosen so that it was long enough to provide sufficient thermal buffering, but not so long that it sacrificed valuable gain fiber. Also, SMF-28 was chosen because its core size and MFD matched well with the Liekki gain fiber's core size and MFD, allowing for low-

loss splices to be made. Estimated splice losses of ~0.17 dB were consistently obtained, about 4% loss per pass.

In addition to the "thermal buffer", SBR heating from absorption of residual pump was reduced with a 980 nm pump reflective coating on the SBR surface[9]. The reflection of pump back into the cavity also allows for more of the pump to be absorbed by the gain fiber. This lowers the pump power required for modelocking, making more pump available should it be needed. To further reduce SBR heating, the GaAs wafer on which the SBR is grown was thinned from 500um down to 150um, putting it in closer proximity to the copper heatsink.

2.1.2.4.2 Modelocking Results

A schematic of the 1 GHz all-fiber laser is shown in Fig. 2-10. The cavity consists of 92mm of Liekki 80dB/m Er-doped gain fiber and a SMF-28 passive fiber section measuring 6mm. The fiber assembly is FC/PC connectorized on both ends, so that one end can be butted against a FC/PC 10% dielectric-coated output coupler, and the other end carefully butt-coupled to a VA86 SBR. An isolated 980nm semiconductor pump diode provides up to 350 mW to the laser. Modelocking is achieved by adjusting the butt-coupling at the SBR end. Through this adjustment, a variety of modelocked states could be obtained – states ranging from a few nm up to 20 nm in bandwidth, and centered anywhere from 1550 nm to beyond 1570 nm. The broadest

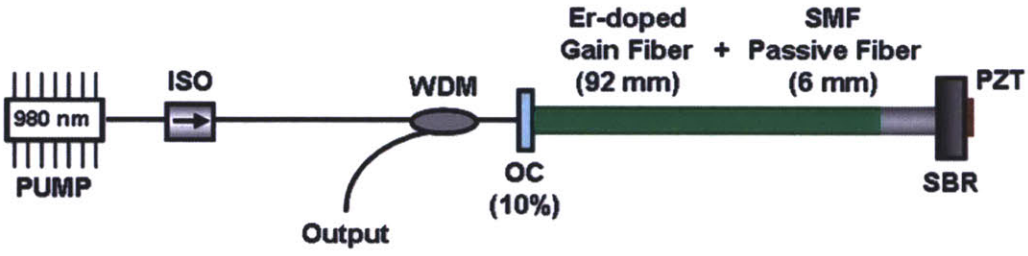

Figure 2-10: GHz repetition rate linear cavity all-fiber laser. The 6mm SMF passive fiber provides a thermal buffer between the gain fiber and SBR. This, along with the addition of a pump reflective coating on the SBR surface, SBR substrate thinning, and better butt-coupling design help to lessen problems with SBR burning.

[9] No such coating was used in the fiber-freespace laser. Absorption of the residual pump was not a major concern here, since the pump was defocused at the SBR surface.

spectral state, centered at 1572 nm with 15.6 nm of bandwidth (corresponding to 166 fs transform-limited sech pulses), is shown in Fig. 2-11. This laser state, along with a handful of others, were used to seed subsequent self-referencing experiments, but were deemed to be too noisy for stabilization. The state considered to be the least noisy is shown in Fig. 2-12. It spans a bandwidth of 7 nm and is centered at 1560 nm (corresponding to transform-limited pulse durations of 360 fs). Modelocking in this state was attained at pump powers above 150 mW, with increasing pump leading to progressively wider optical spectra. At 300 mW pump, the spectrum shown in Fig. 2-12 was produced, with output powers of 10 mW (pulse energies of 10 pJ).

The laser operates in the soliton regime with a calculated total cavity roundtrip dispersion of $-5000fs^2$, and soliton pulse shaping again dominates over SBR effects (actually, this state is even more soliton-like than the state given in Fig. 2-8, as can be reasoned by comparing the "$sech^2$-ness" of the two optical spectra). At 100 pJ intracavity pulse energies, the soliton area theorem (Eq. 2.1) predicts pulse durations of 285 fs.

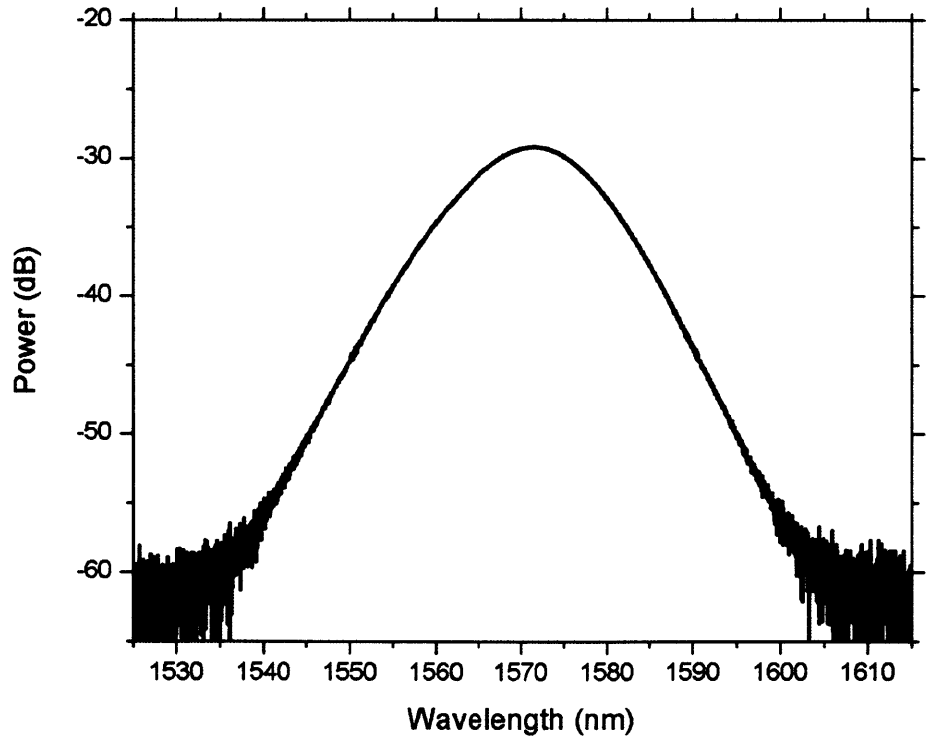

Figure 2-11: One of many mode-locked states attainable with the GHz all-fiber laser. This state, centered at 1572nm, offered the broadest optical spectrum (15nm) with output pulse energies of 25pJ.

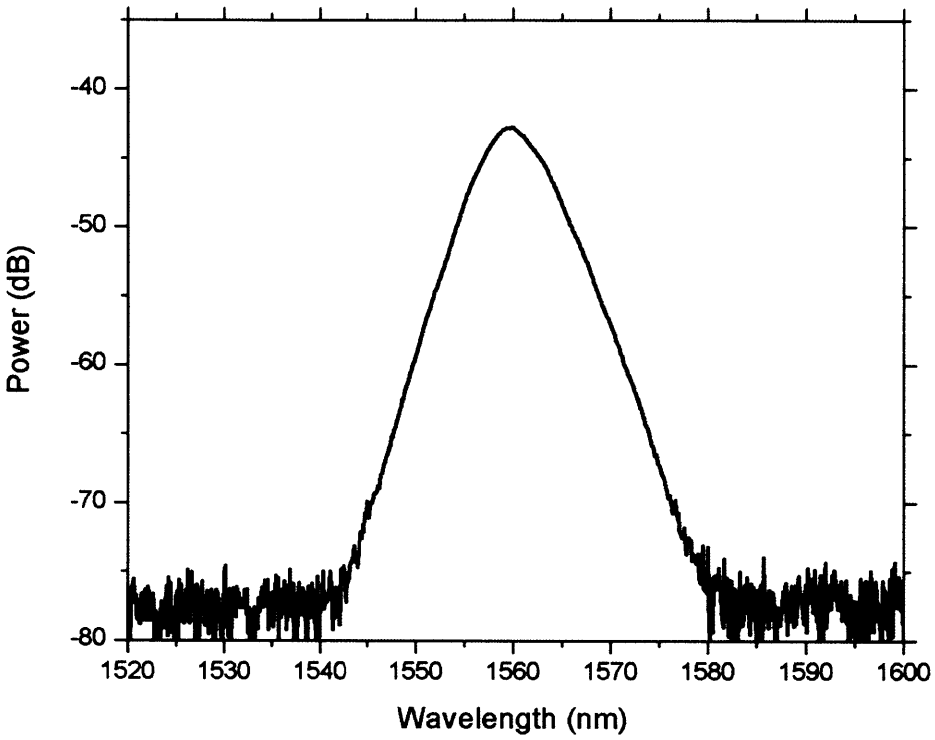

Figure 2-12: Another mode-locked state out of the GHz all-fiber laser. The optical spectrum of this state is centered at 1560nm and spans a FWHM bandwidth of 7nm, with output pulse energies of 10pJ.

2.1.2.4.3 Vector Solitons

The lack of a polarization discriminator in this laser cavity again causes polarization rotations that are not periodic with roundtrip. In the fiber-freespace laser configuration, a polarizer was inserted to fix this, but the all-fiber arrangement doesn't permit such a solution. Instead, since polarization rotation is largely attributed to cavity birefringence, this birefringence can be used to manipulate not only polarization rotation, but also its periodicity. The idea is to adjust the cavity birefringence to find states where the polarization rotation is periodic with the laser's repetition rate (roundtrip frequency).

Changes to cavity birefringence are accomplished through twisting and squeezing of the fiber assembly. This causes the location of the resulting polarization sidebands to shift (a consequence of the changing periodicity), and this tactic can be used to find states where the sidebands collapse into the repetition rate. The twisting and squeezing action, when done in a

controlled manner, can provide the continuous birefringence adjustments needed to easily and reliably push the sidebands into the repetition rate. Most of the time, this can be achieved by pushing on the fiber and twisting of the fiber ends. A more sophisticated contraption using an inline polarization controller was also employed to allow for more precise adjustments. Once collapsed, the polarization rotations are periodic with the laser repetition rate, and the pulses at the laser output have a consistent (non-rotating) polarization. A combination of amplification and highly nonlinear spectral generation tests were conducted, in the same manner described in Sec. 2.1.2.3 and depicted in Fig. 2-9, to confirm that these sidebands weren't just partially suppressed, but truly eliminated.

2.1.2.4.4 Repetition Rate Locking

There are two commonly employed mechanisms for adjusting the cavity length of fiber laser cavities. Those mechanisms, depicted in Fig. 2-13, depend heavily on the type of laser cavity configuration, as well as on bandwidth objectives/requirements. If the laser cavity contains a

Figure 2-13: Two approaches for repetition rate control. A piezo-mounted end mirror (SBR) is used in free-space configurations, while all-fiber configurations typically employ piezo fiber-stretchers for cavity length adjustments. Both approaches are shown for a linear cavity setup.

free-space section, it's generally recommended that one of the end mirrors be attached to a piezo-transducer and used to correct for fluctuations to repetition rate because of its potential for higher locking bandwidths. In all-fiber configurations where such an approach is not possible, a piezo fiber-stretcher can be used for repetition rate adjustments, but at the expense of decreased locking bandwidths. In our GHz all-fiber laser, neither of these two mechanisms is very straightforward in their implementation. The piezo-fiber-stretcher scheme was considered first,

but the short fiber lengths made implementation extremely difficult. The birefringence changes resulting from fiber stretching are also of concern, given our need for full suppression of polarization sidebands. This leaves the piezo-end-mirror scheme, which, despite the all-fiber laser cavity, is physically possible because of its linear cavity configuration. The extreme sensitivity to butt-coupling, however, implies that the coupling losses would be too high. The concern being that even the slightest of adjustments to SBR position would knock the laser out of modelocking, or at the very least, change modelocking states.

Nevertheless, the SBR was outfitted with a piezo-electric transducer[10], and tests conducted to measure the laser's sensitivity to butt-coupling. The butt-coupling gap could be moved by about 0.45μm (corresponding to a repetition rate change of 3 kHz) before modelocking was lost[11]. No change in modelocking state was detected, only a slight shifting of the center wavelength and decrease in bandwidth, over this range. This 3 kHz range should cover fluctuations in repetition rate. To minimize these fluctuations, the laser was isolated from environmental disturbances (e.g. air currents, acoustic/mechanical vibrations, etc.). An enclosure with inch-thick foam layers was constructed to cover the laser, which was enough to lower the repetition rate changes to ~0.1 kHz measured over several minutes. The 0.1 kHz jitter corresponds to cavity length fluctuations of 30 nm, which is well within the demonstrated piezo movement range.

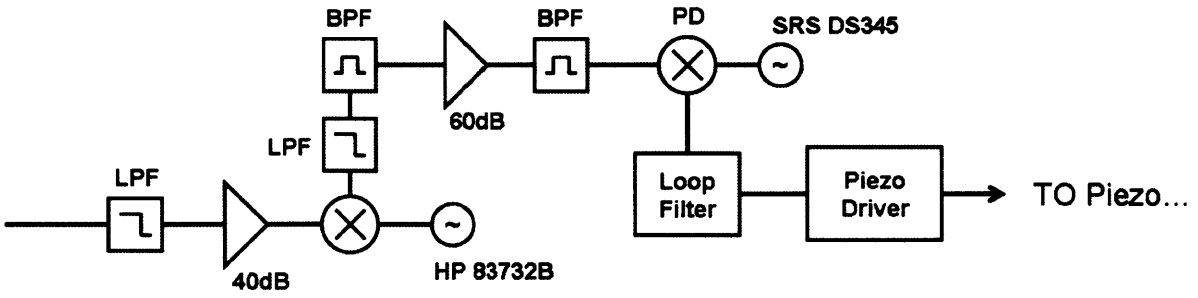

Figure 2-14: Locking electronics setup for stabilization of the repetition rate to a RF reference oscillator (SRS DS345). The GHz repetition rate is first lowpass filtered and amplified before being mixed down to 10.7MHz. The result is then lowpass and bandpass filtered, amplified, and again bandpass filtered before phase detection with the RF reference oscillator. The error signal is loop filtered with proportional integral gain, and sent into a high-voltage piezo driver for controlling the piezo.

[10] The SBR is mounted on a thin copper disk (1cm diameter, 1mm thick), and the copper disk mounted on the piezo-actuator. The copper disk is necessary for heatsinking, but was machined as small as possible to reduce the load on the piezo.

[11] The Rayleigh length for 1560nm-centered pulses out of SMF-28 fiber is 54.5μm.

The repetition rate locking setup is detailed in Fig. 2-14. The laser output is split via a 50/50 fiber coupler, and half the output sent into a fast photodiode (biased InGaAs) to detect the 1 GHz repetition rate pulse train. The 1 GHz repetition rate signal is amplified, and mixed with the output of a signal generator (HP 83732B) down to 10.7 MHz. This is then passed through a series of lowpass and bandpass filters, amplified, and again bandpass filtered before being sent for phase detection to be compared against a RF reference oscillator (SRS DS345) at 10.7 MHz. The error signal generated out of the phase detector is sent to a servo lockbox (Precision Photonics LB1005), essentially a loop filter with proportional-integral gain, to generate the feedback control signal driving the piezo. Optimized lock settings of 7.2 and 1 kHz for the gain and corner frequency, respectively, were used to lock the repetition rate.

Initially, a digital phase detector with $\pm 32\pi$ of tracking range was used for the phase detection. Fig. 2-15 shows the phase detector output (through a separate monitor port in the phase detector unit) when the lock is initiated. The detector's 6 Volt swing collapses to 3mV when locked. The trace was recorded for 100 seconds (the limit for the oscilloscope used), but

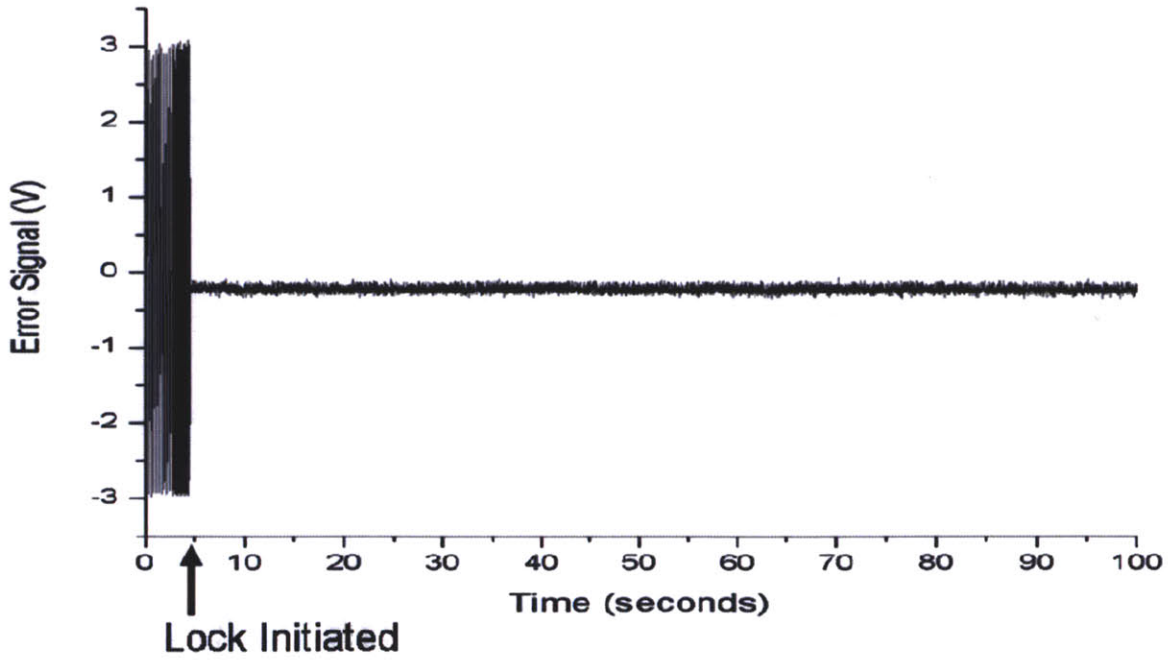

Figure 2-15: In-loop error signal out of the digital phase detector, plotted over 100 seconds. The error signal collapses to 3mV RMS when the lock is initiated, and lasted until the lock was intentionally broken.

the lock remained much past this point, and was only lost when it was intentionally broken. The "locked" voltage of 3mW corresponds to a residual phase noise of 0.1 rad. Note that repetition rate locks are usually better than this, and our lock was also better. It turns out the digital phase detector was resolution limited to 3mW. When an analog mixer was used in its place, the residual phase noise was reduced to 1.4 mrad (lock settings: 7.1 Gain, 1 kHz Corner Frequency).

A spectral plot of the single-sideband phase noise was measured using a signal source analyzer (Agilent 5052A). Fig. 2-16 shows the resulting traces for both free-running (black curve) and locked (red curve) conditions. A locking bandwidth of ~1 kHz is deduced from these traces. Integrated timing jitter is also plotted here (dotted curves). The main contributions to timing jitter occur at frequencies below 1 kHz, which is within our locking bandwidth. In the

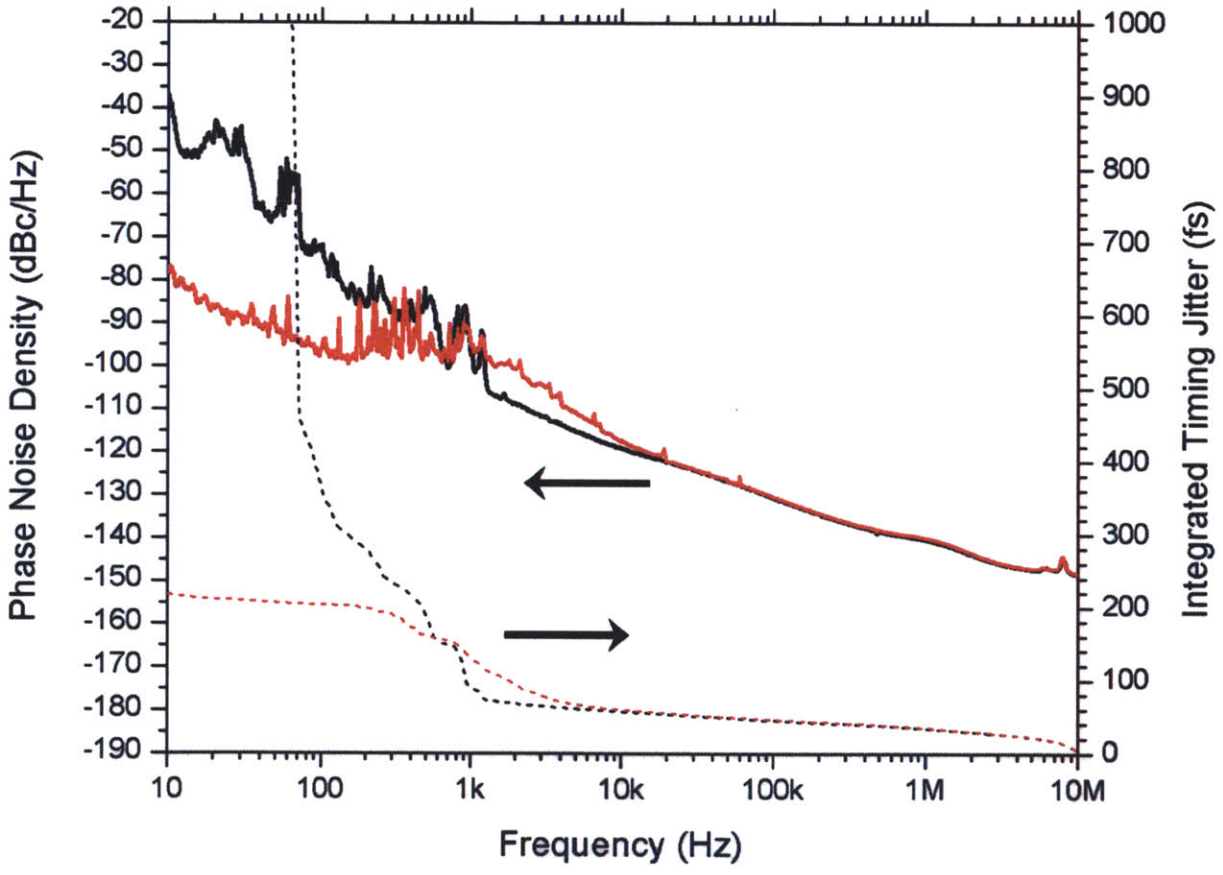

Figure 2-16: Phase noise comparison for free-running (black) and repetition-rate-locked (red) systems. The traces indicate a locking bandwidth of ~1kHz. Integrated timing jitter (integrated from 10MHz) is plotted, demonstrating 217fs of integrated timing jitter from [10Hz,10MHz] when locked (compared to 5.2ps over the same range when unlocked).

free-running case, integrated timing jitter starts to significantly increase below 1 kHz, and explodes below 100 Hz – an integrated timing jitter of 5.2 ps between 10Hz and 10MHz. When locked, the integrated timing jitter drops to 217 fs across this same integration range.

2.2 Harmonic Modelocking at GHz Repetition Rates

Harmonic modelocking refers to the scenario where a modelocked laser operates with multiple pulses and the pulses are equally separated, as shown in Fig. 2-17. This leads to an output pulse train whose repetition rate is scaled by the number of pulses inside the cavity. Multi-pulsing can occur in fundamentally modelocked lasers when the gain is made large enough leading to the breakup of a single strong pulse into multiple weaker pulses[12]. Such lasers have a tendency to break up strong pulses to avoid modelocking instabilities associated with the accumulation of large nonlinear phase shifts [50].

Sorting techniques involving intracavity modulators or interferometers are typically used to force pulses into equal temporal spacing. There are, however, instances when the pulses self-

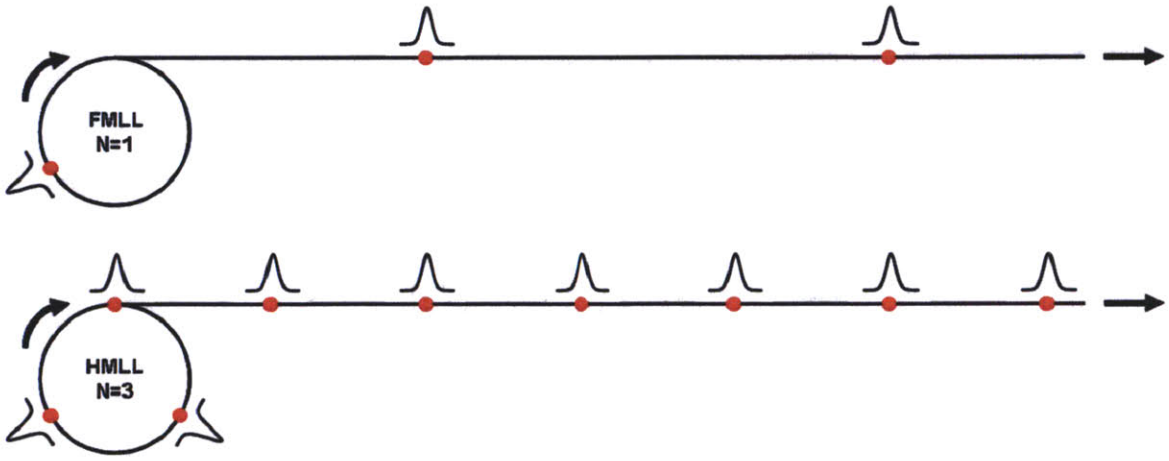

Figure 2-17: Illustration of fundamental mode-locking (FMLL) versus harmonic mode-locking (HMLL). A FMLL has a single pulse traversing the laser cavity, while a HMLL has multiple evenly-spaced pulses traversing the laser cavity. Harmonic mode-locking increases the repetition rate by a factor equal to the number of pulses circulating the laser cavity.

[12] If there's not enough gain to support multiple pulses, CW breakthrough can occur to keep pulses from getting too strong.

sort. That is to say, the pulses circulating the laser cavity sort themselves without influence from an intrusive sorting element. Saturable absorbers have been known to elicit this type of behavior, which has been attributed to its recovery time dynamics [51]. We've observed this in our SBR-modelocked GHz fiber lasers as well. On several occasions, searching for different modelocked states led us to a self-sorted harmonically modelocked 2 GHz output pulse train. The RF spectral trace for this is shown in Fig. 2-18. The trace includes polarization sidebands, as these could not be suppressed without knocking the laser out of harmonic modelocking. For comparison, a 1 GHz fundamentally modelocked pulse train out of the same laser is shown (along with the optical spectra corresponding to the two cases). In general, self-sorting requires the "right" conditions, and is extremely difficult to reproduce. Other approaches are therefore used to provide more reliable and consistent operation.

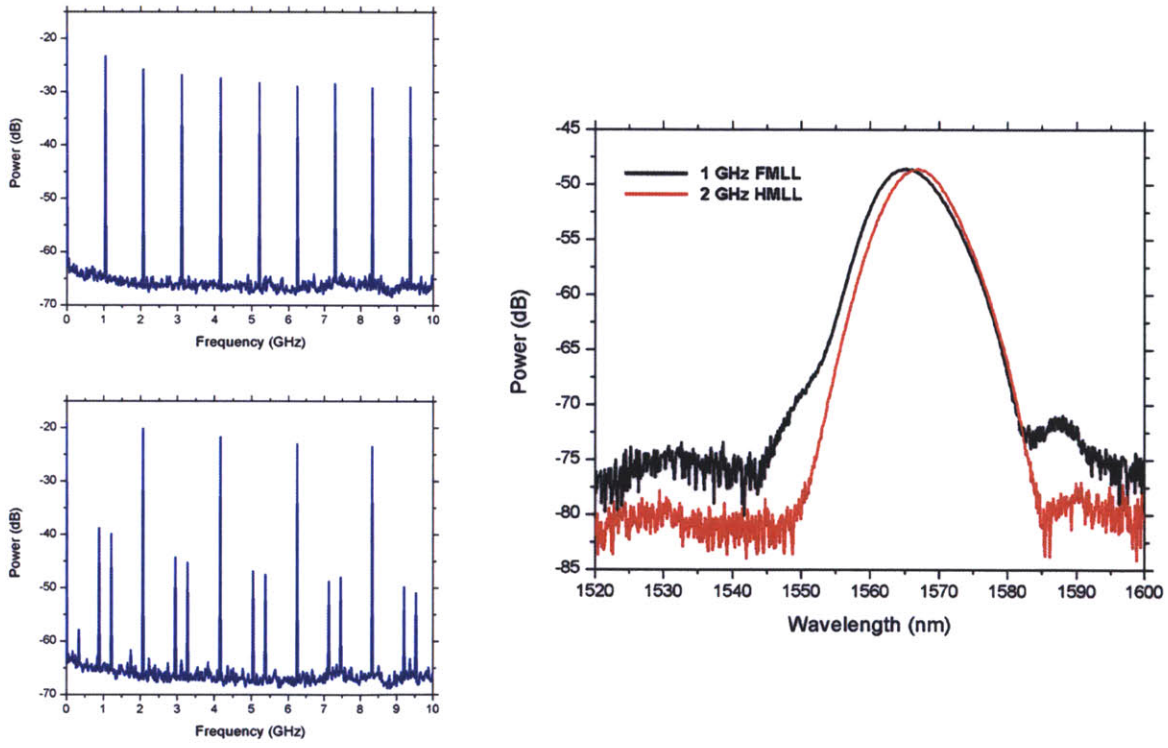

Figure 2-18: Fundamental and harmonic mode-locking from the GHz all-fiber laser. (a) The RF spectrum of the FMLL shows clean and stable operation at 1 GHz. (b) The RF spectrum of the HMLL operating at 2 GHz (via self-sorting) displays amplitude modulation sidebands due to vector soliton behavior. (c) The optical spectra corresponding to the 1GHz FMLL and 2GHz HMLL states.

2.2.1 Active Harmonic Modelocking

The most direct way to achieving harmonic modelocking is through the use of active modelocking techniques involving the periodic modulation of cavity loss (AM) or phase (PM). The literature is rich with systems of this configuration. Of particular note are the HMLL systems simultaneously being developed in the Delfyett Group at CREOL and the Nakazawa Group at Tohoku University.

Delfyett Group HMLL System [52]

Harmonic modelocking is achieved using a regeneratively-driven intracavity amplitude modulator, generating pulses compressible to 863fs durations at a repetition rate of 10.24GHz (fundamental repetition rate of 33.5MHz). An ultra-stable high-finesse (F=100) intracavity Fabry-Pérot serves two purposes – improved supermode suppression and optical frequency stabilization. The filtering property of FPs in the frequency domain is exploited to further suppress the fundamental frequency modes (i.e. supermode suppression). To lock the laser frequencies to the ultra-stable FP resonances, two PDH locks are implemented providing feedback to a piezo-mounted collimator and to a voltage-controlled phase shifter in the regenerative loop. The two feedback loops should be able to compensate for any frequency drifts, resulting in a comb with sub-10kHz linewidths and sub-1MHz drifts.

Nakazawa Group HMLL System [53,54]

Harmonic modelocking is similarly achieved using a regeneratively-driven intracavity amplitude modulator, generating 3ps pulses at 40GHz repetition rates (fundamental repetition rate of 30MHz). This system also employs a high-finesse (F=500) FP cavity for the suppression of supermode noise. However, instead of locking the laser to the FP cavity, the FP cavity is temperature-tuned to follow the laser for the purpose of eliminating mode-hopping. For stabilization, the optical frequencies are locked to an RF synthesizer (f_{rep}) and to a C_2H_2 molecular absorption line (f_{ceo}).

A major drawback to active modelocking, however, is its inability to generate pulses as short as those possible through passive modelocking. Active modelocking generally produces pulses in

the picosecond regime, which is too long for self-referenced frequency comb generation. To overcome this, passive measures are used in combination with active modulation, the former for pulse shaping and the latter for pulse sorting. A 1 GHz harmonically modelocked laser using this balance of active and passive modelocking is implemented for the generation of femtosecond pulses at GHz repetition rates.

2.2.1.1 1 GHz Harmonically Modelocked Laser w/ Regenerative Feedback

A 1 GHz harmonically modelocked laser designed with regenerative feedback to an intracavity phase modulator is shown in Fig. 2-19. In this design[13], a regeneratively-driven phase modulator functions as the sorting element by compensating for fluctuations in pulse timing through shifts of the pulse's carrier frequency. Together with cavity dispersion, these frequency shifts serve to re-time the pulses. The phase modulator is driven at 1 GHz, the 65th harmonic of the fundamental repetition rate (15.4 MHz). It is referred to as regenerative feedback because the 1 GHz signal driving the phase modulator is actually derived from the output pulse train itself. This automatically adjusts the frequency of the phase modulation to the cavity roundtrip frequency.

Two 500 mW, 980 nm pump diodes are polarization-multiplexed together to provide the energy required for the 65 intracavity pulses. The laser relies on P-APM to shape the pulses, thereby allowing for the generation of shorter pulses compared to what's achievable with the actively driven phase modulator. P-APM is achieved in this laser cavity through nonlinear polarization rotation, two sets of QWPs and HWPs, and a polarizing isolator. The spectral filter is used to tune the laser's center wavelength.

Harmonic modelocking results are presented in Fig. 2-20. The modelocked optical spectrum is centered at 1543 nm and spans 3.6 nm, corresponding to transform-limited pulse durations of 694 fs. In this configuration, the laser remains modelocked even if there exist pulse dropouts. Verification of no pulse dropouts is done by checking suppression levels of the RF frequency modes. Suppression levels should be greater than 60 dB when all slots are occupied. One pulse dropout decreases the suppression level to 37dB. Our measured suppression levels of 41dB confirms a 1 GHz pulse train with no pulse dropouts.

[13] This is a slightly redesigned version of [55].

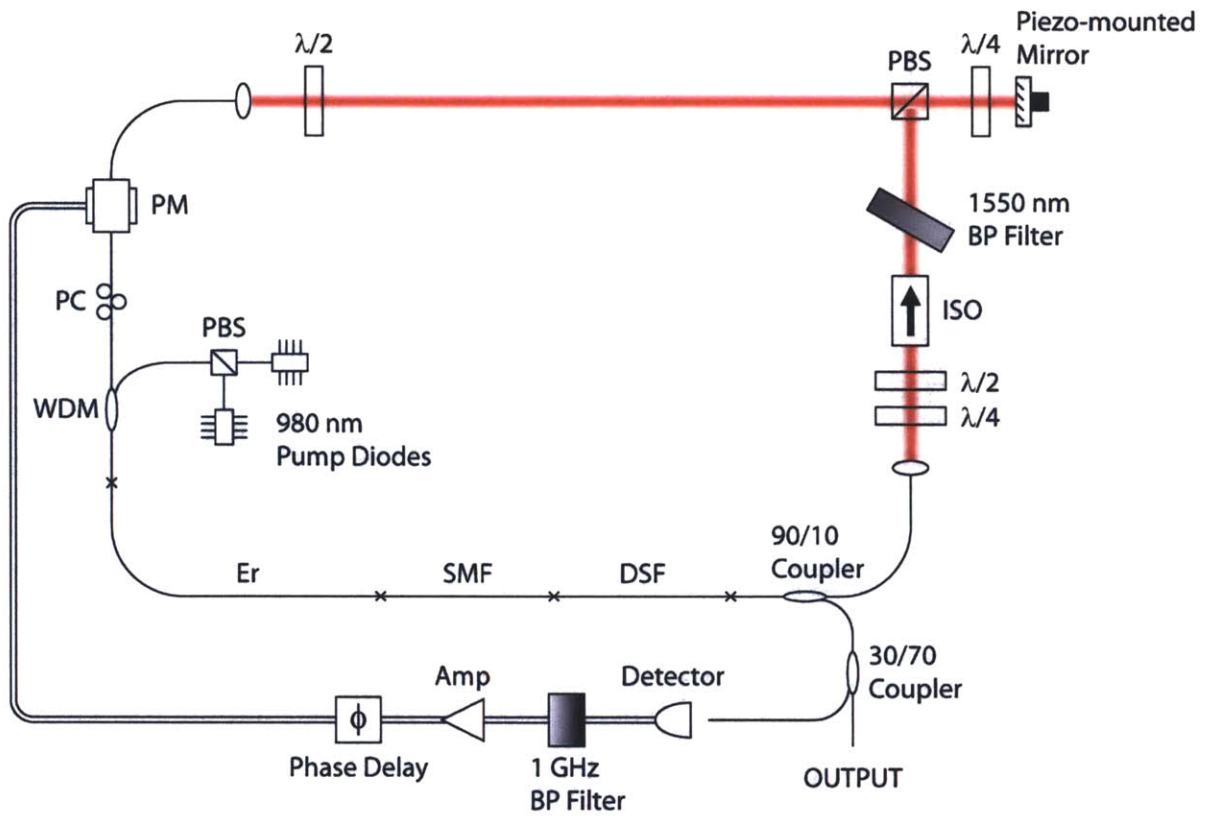

Figure 2-19: Schematic of a 1 GHz harmonically mode-locked fiber laser, passively mode-locked using P-APM. The laser cavity length ~13.5 m (93% in fiber) corresponds to a fundamental repetition rate of 15.4 MHz, meaning 65 evenly-spaced intracavity pulses are required for 1 GHz operation. The regeneratively-driven phase modulator (PM) is responsible for sorting the intracavity pulses.

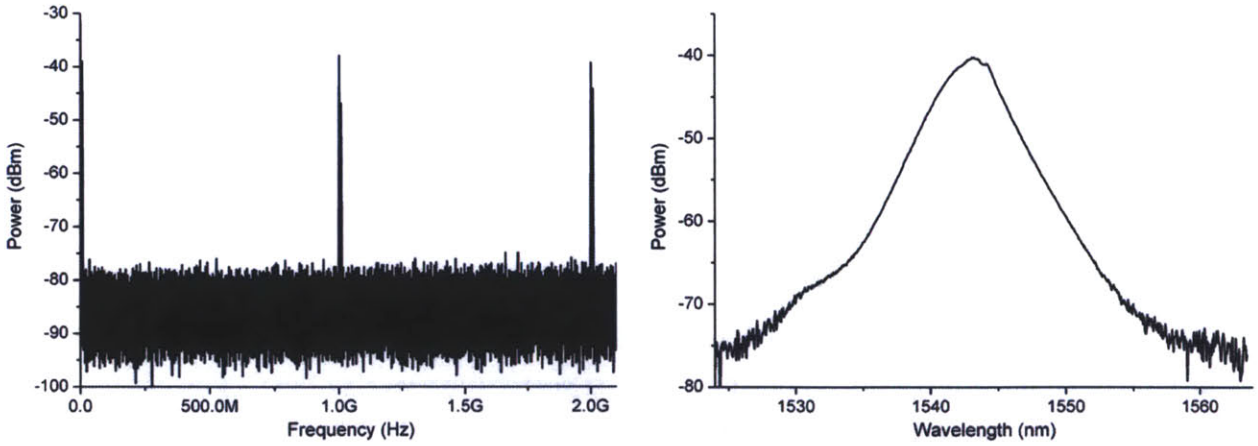

Figure 2-20: 1 GHz HMLL output characteristics. The RF spectrum confirms 1GHz operation with the suppression of the 15MHz fundamental modes by at least 41dB (i.e. one pulse dropout corresponds to a sidemode suppression of 37dB). The optical spectrum demonstrates mode-locking at a center wavelength of 1543nm with a FWHM bandwidth of 3.6nm (corresponding to transform-limited pulses of 694fs).

2.2.2 Phase Correlation between Pulses

The stabilization of the carrier-envelope phase slip $\Delta\Phi_{ce}$ in a harmonically mode-locked laser is more challenging than that in a fundamentally mode-locked laser, as $\Delta\Phi_{ce}$ stabilization in the former requires proper phase relationship for all the pulses in the cavity. To clarify, recall that the output pulse train of a fundamentally mode-locked laser has a carrier-envelope phase slip from pulse to pulse, denoted by $\Delta\Phi_{ce}$, due to differences in group and phase velocities in the laser cavity. In a harmonically mode-locked laser, where multiple pulses circulate the laser cavity, the picture of its output pulse train is rather different, as depicted in Fig. 2-21.

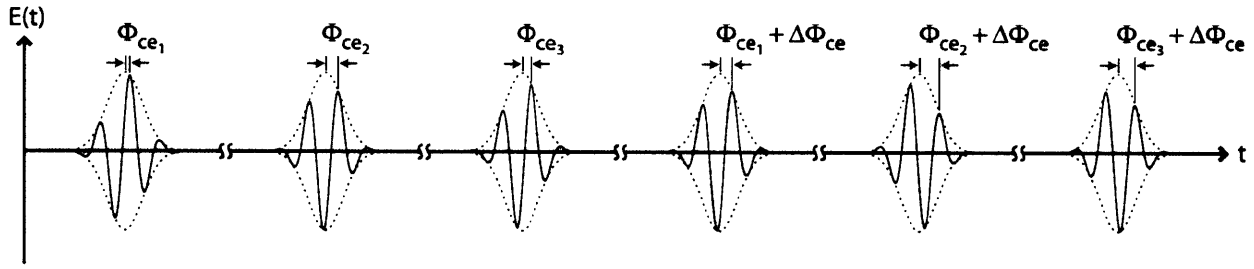

Figure 2-21: The output pulse train of a harmonically mode-locked laser containing 3 intracavity pulses, each with its own distinct carrier-envelope phase shift (Φ_{ce}). The pulse-to-pulse carrier-envelope phase slip differs even though the intracavity pulses experience the same roundtrip carrier-envelope phase slip, $\Delta\Phi_{ce}$.

Even though all the pulses in the cavity experience the same $\Delta\Phi_{ce}$ phase shift every roundtrip through the cavity, their starting Φ_{ce}'s are independent of one another. Then, with the exception of a few cases, the pulses output from the laser no longer exhibit a constant carrier-envelope phase slip from pulse to pulse, in which case $\Delta\Phi_{ce}$ becomes ill-defined. In the example of the harmonically mode-locked laser containing 3 pulses depicted in Fig. 2-21, only if

$$\Phi_{ce_2} = \Phi_{ce_1} + \frac{1}{3}\Delta\Phi_{ce} \quad \text{and} \quad \Phi_{ce_3} = \Phi_{ce_1} + \frac{2}{3}\Delta\Phi_{ce} \tag{2.2}$$

will there be a consistent carrier-envelope phase slip from pulse to pulse, equal to

$$\Delta\Phi_{ce_{eff}} = \frac{\Delta\Phi_{ce}}{3} \tag{2.3}$$

where $\Delta\Phi_{ce}$ is the carrier-envelope phase slip encountered by each pulse in the laser cavity every roundtrip. Therefore, it's important that there be an imposed phase correlation between all the pulses in the laser cavity.

A qualitative description of harmonic modelocking will now be given to make this even more clear. The pulse train out of a harmonically modelocked laser supporting N phase-uncorrelated pulses can be represented in terms of a fundamentally modelocked laser (i.e. N=1) as follows:

$$P_{HMLL}(t) = \sum_{k=1}^{N} P_{FMLL}\left(t - k\frac{1}{Nf_r}\right)e^{-i\Phi_k} \tag{2.4}$$

where $P_{FMLL}(t)$ represents the pulse train out of a fundamentally modelocked laser operating at a repetition rate of f_r, following the definition given in Eq. (1.3). Also, it's been assumed that all N pulses making up the harmonically modelocked laser be indistinguishable in both shape and duration (i.e. all N pulses have identical pulse envelopes). In the frequency domain (using the Fourier Transform identity for timing shifts), this becomes:

$$P_{HMLL}(f) = \sum_{k=1}^{N} P_{FMLL}(f)e^{-i2\pi f\left(k\frac{1}{Nf_r}\right)}e^{-i\Phi_k} \tag{2.5}$$

where $P_{FMLL}(f)$ represents the comb of discrete frequencies, spaced by f_r, out of a fundamentally modelocked laser. From this, it's clear that the N harmonic pulses all consist of the same frequencies. It's the phases at each of these frequencies that differ from pulse train to pulse train. Next, let's consider the results of the following summation:

$$\sum_{k=1}^{N} e^{-i2\pi f\left(k\frac{1}{Nf_r}\right)} \underset{f=mf_r}{=} \sum_{k=1}^{N} e^{-i2\pi k\frac{m}{N}} = \begin{cases} N & \text{for } m \text{ a multiple of } N \\ 0 & \text{otherwise} \end{cases} \tag{2.6}$$

When f is a multiple of the harmonic repetition rate, Nf_r, the summation goes to N. In all other cases, this becomes a summation of a constant-interval sampled sinusoidal signal, which sums to zero since the sampling interval differs from the signal period. Conclusions about Φ_k can now be made. When all Φ_k's are equal, Eq. (2.5) breaks down to that of a fundamentally modelocked laser output spectrum with repetition rate Nf_r, and this is what is meant by phase correlation of the N harmonic pulses. All other scenarios for Φ_k will lead to a non-constant weighting for the summation of the sinusoidal expression given in Eq. (2.6), which at best, results in partial suppression of the N-1 frequency modes. Total suppression of these N-1 modes, along with perfect constructive interference of the Nth mode, is only possible in the phase-correlated case

(i.e. $\Phi_1 = \Phi_2 = \Phi_3 = \ldots = \Phi_N$). Only the Nth mode survives in this case, making it indistinguishable from the output of a fundamentally modelocked laser operating at that multiplied repetition rate. Keep in mind that this analysis takes place in the optical domain. Things are drastically different in the RF domain, where full suppression can be achieved without phase correlation (e.g. Fig. 2-20).

2.2.3 Passive Harmonic Modelocking (w/ Pulse-to-Pulse Phase Correlation)

Passive harmonic modelocking requires a non-active sorting element to take the place of amplitude/phase modulators – candidates include FPI, GTI, MZI, etc. In addition to sorting, these interferometers provide a means for establishing phase-correlated pulses inside a harmonically modelocked laser. Two attempts were made at implementation using both FPIs and GTIs. Harmonic modelocking was not achieved in either configuration, but valuable insight was gathered and is shared in the sections that follow.

2.2.3.1 Gires-Tournois and Fabry-Pérot Interferometers w/ Regenerative Feedback

Our first attempt at passive harmonic modelocking with an intracavity interferometer was based off the HMLL depicted in Fig. 2-19. A free-space GTI was inserted after the polarizing beamsplitter, and a HWP placed at its input to adjust the tap-off amount (Fig. 2-22). We chose to use a GTI because its configuration provided the most flexibility, as a pre-aligned GTI could be inserted into (and taken out of) the laser cavity with minimal disruption to the laser's modelocking state. In addition, ideal GTIs are lossless, imparting only a frequency-dependent phase (i.e. no filtering) to the pulses in the laser cavity, which should also help reduce the amount of disturbance to the laser's modelocking state. The regeneratively-driven phase modulator remained connected, as it could be used to help initiate modelocking. Once initiated, the modulator would be switched off.

In our efforts to obtain modelocking, every knob was turned and every sequence and combination of actions exhausted. This included adjustment of all waveplates and polarization controllers (for P-APM), methodical tuning of the GTI cavity spacing, different pumping levels,

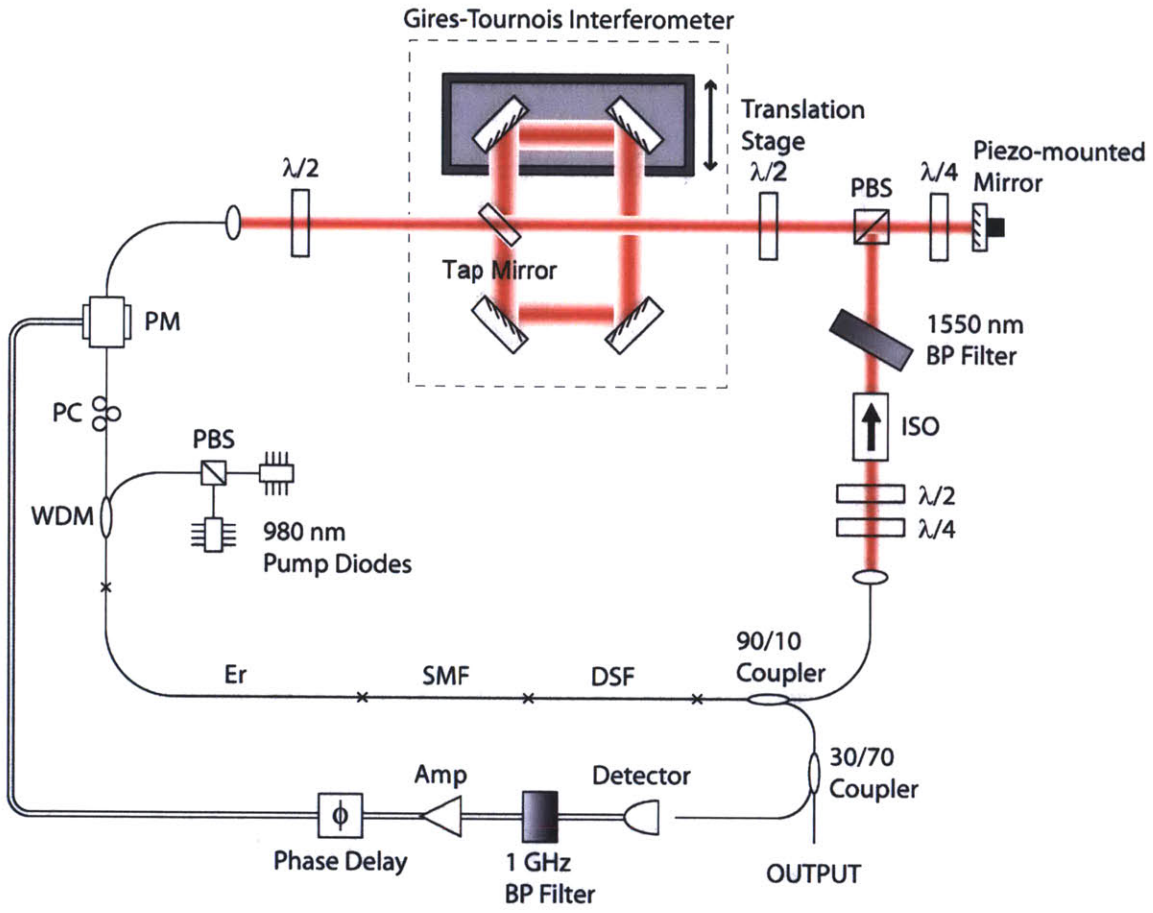

Figure 2-22: Schematic of a 1 GHz phase-correlated harmonically mode-locked fiber laser. The insertion of a Gires-Tournois Interferometer serves to phase-correlate the intracavity pulses, in addition to sorting them. Its configuration allows for easy removal and re-insertion (i.e. by blocking the tapped-off beam) with minimal disturbance to laser operation. If needed, the regeneratively-driven phase modulator (PM) can be used for initiating harmonic mode-locking.

etc. The regenerative feedback loop was switched on and off as well, to no effect. When the GTI was blocked from feeding back into the laser cavity, modelocking was achieved with help from the regenerative feedback loop (see results in Sec. 2.2.1.1 and Fig. 2-20). But modelocking would disappear once the GTI was unblocked. This sequence of blocking and unblocking was performed over the entire GTI translation range, but the results were no different. Lastly, we replaced the GTI with a FPI consisting of 90% reflectivity mirrors (Finesse = 30). This also did not lead to modelocking.

Temporal misalignment of the GTI/FPI and laser cavity is believed to be the problem. Our approach for alignment doesn't appear to be sensitive enough in this case. And even when aligned, drifting is a concern, especially over long timescales. A locking scheme will therefore

need to be implemented so that the laser cavity can be synchronized to the GTI/FPI, or vice versa [56].

2.2.3.2 Gires-Tournois and Fabry-Pérot Interferometers w/ Saturable Absorbers

Temporal misalignment of the GTI/FPI and laser cavity, including alignment drifts over time, makes modelocking very difficult. A locking scheme was recommended above to better deal with this, but another option exists – the use of SA-modelocking to correct for mismatches in temporal alignment. This idea stems from our experience with SA-modelocking, and the fact that modelocking was consistently observed over a wide range of center wavelengths. Furthermore, the center wavelength could be shifted in a continuous manner without loss (or change) of the modelocked state, by, among other things, small changes to the butt-coupling. Operation over a continuous range of center wavelengths is therefore possible. This is important because shifting of the center wavelength, together with cavity dispersion, can be used to re-time pulses (similar to the phase modulation concept for timing correction). Modelocking should then be possible even under misaligned conditions (not too misaligned). More importantly, sustained modelocking should now be possible, as drifts over time in the alignment would be automatically corrected. Tamura and Nakazawa reported on similar behavior with a 10GHz actively-modelocked HMLL [57]. The repetition rate of their HMLL was allowed to drift (i.e. no attempts were made to stabilize the laser repetition rate or even to shield the cavity from environmental disturbances), but modelocking was still maintained over long time intervals. Changes to pulse shape/duration and optical spectrum shape/bandwidth were minimal; instead, shifts in the center wavelength were observed to compensate for the changes to repetition rate. As a further test, the center wavelength was manually tuned over an 8nm range (1553.8nm-1561.8nm) by controlled adjustments to the repetition rate via an intracavity delay line.

A schematic of our setup is provided in Fig. 2-23. An improved design for a 1 GHz harmonically modelocked fiber laser is implemented, whereby the fiber cavity is rebuilt with shorter cavity lengths in mind. The result is that fewer pulses are needed in this laser cavity to achieve the same 1 GHz pulse train at the output (15 intracavity pulses in this design versus 65 in the previous design). In addition, the shorter cavity design reduces limitations to pulse duration caused by resonant spectral sidebands (Kelly sidebands). Decreasing the length of the cavity

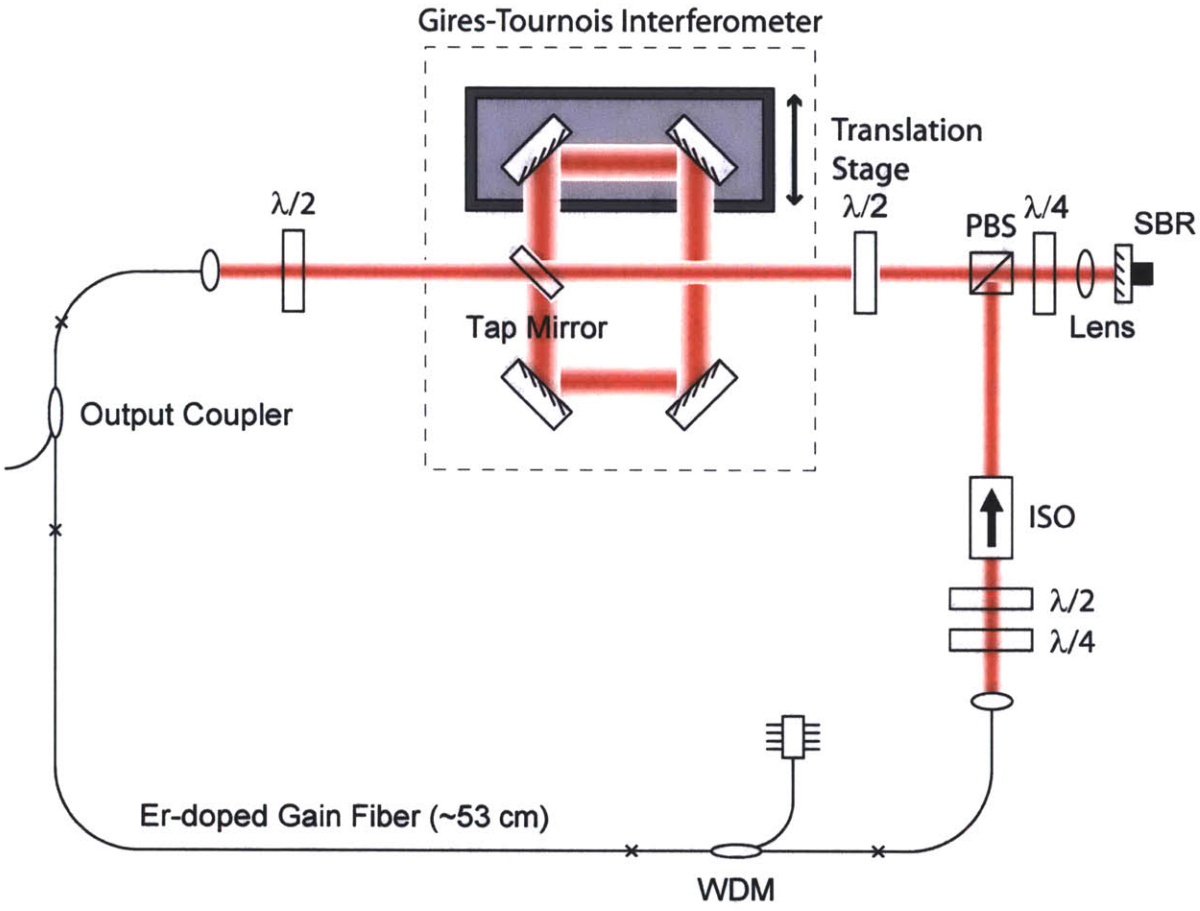

Figure 2-23: An improved 1 GHz phase-correlated harmonically mode-locked fiber laser design. This laser cavity operates at a fundamental repetition rate of 68MHz, which means only 15 evenly-spaced intracavity pulses are required for 1GHz operation. The Gires-Tournois Interferometer sorts and phase-correlates the 15 intracavity pulses. An SBR is used to initiate mode-locking, as well as sustain mode-locking through re-adjustments of the center wavelength to compensate for temporal misalignment of the laser cavity and GTI.

increases the spacing between the Kelly sidebands, allowing for wider optical spectra and consequently, shorter pulses. The pulses output from this new laser cavity are predicted to be 2 to 3 times shorter than those output from the previous design (200 fs compared to 500 fs). The shortened cavity also provides the added benefit of placing lesser constraints on the strength of the resonating interferometer (i.e. it allows for lower-Q cavities), since its frequency comb lines are spaced further apart.

A combination of SBR-modelocking and soliton pulse shaping is used to generate 255 fs transform-limited pulses, with a fundamental repetition rate of 68.3 MHz. Modelocking at this repetition rate was achieved with extremely low pump powers (50mW). The 1 GHz GTI cavity

was then inserted, resulting in loss of modelocking. Because we were running into pump limitations, a lower multiplication factor was tried. Instead of 15, a factor of 9, which corresponds to a harmonic repetition rate of 615 MHz (and a GTI spacing of 49cm), was implemented. More than enough pump was available for operation at this harmonic. Even then, however, modelocking could not be achieved with the intracavity GTI, nor with an intracavity FPI (Finesse = 30).

Future steps should include better isolation of the laser setup to protect against environmental and man-made disturbances in hopes of minimizing cavity drifts, a thermally-stable FPI (equipped with Zerodur/ULE spacers), and implementation of a locking scheme for synchronization of the laser and interferometer cavities to one another (along the lines of the PDH locking scheme used in the Delfyett HMLL).

Chapter 3

High Power Amplification and Femtosecond Pulse Compression*

The development of GHz repetition rate lasers brings forth the need for new and improved techniques for the amplification and compression of ultrafast pulses. These techniques need to provide higher levels of amplification so that the required pulse energies can still be achieved at the higher repetition rate. Additional compression is also needed to compensate for the longer pulses that result from saturable absorber modelocking compared to P-APM. Systems currently employed for lower repetition rate sources are at, or are very close to, their practical limit, and cannot be scaled much further. An analysis is performed to determine this limit. At 1 GHz, amplification and compression to levels necessary for octave-spanning supercontinuum generation are still possible, but extremely difficult. Instead, a novel amplification/compression scheme with the potential for use in 10 GHz (and even 100 GHz) systems is proposed and demonstrated with our 1 GHz source.

* With contributions from Jason Sickler

3.1 Watt-level High-power Ultrafast Pulse Amplification

Most traditional approaches to ultrafast pulse amplification use variations of the fiber amplifier configuration depicted in Fig. 3-1. This basic fiber amplifier design consists of a single WDM with pump and signal input ports, and an output port spliced to a length of gain fiber. In the case of 1.5 μm amplification using Er-doped gain fibers, pump wavelengths at 980 nm and 1480 nm coincide with the gain fiber's absorption peaks. Typical pump-to-signal conversion efficiencies range from 20% to 40%, depending on the pump wavelength and gain fiber used [58]. Most of our 980 nm pumped fiber amplifiers give a conversion efficiency of 20%, using the Liekki family of gain fibers with 110dB/m, 80dB/m, and 40dB/m doping levels (with optimized gain fiber lengths). The 980 nm semiconductor pump diodes used offered 500mW – 700mW, leading to amplifications to 100mW – 140mW (when operating above the saturation power). 1480 nm semiconductor pump diodes were never used, but 30% conversion efficiency can be assumed by taking into account the quantum efficiency difference between 1480 nm and 980 nm. 400mW pump diodes are available at 1480nm, and should provide amplification to 120mW.

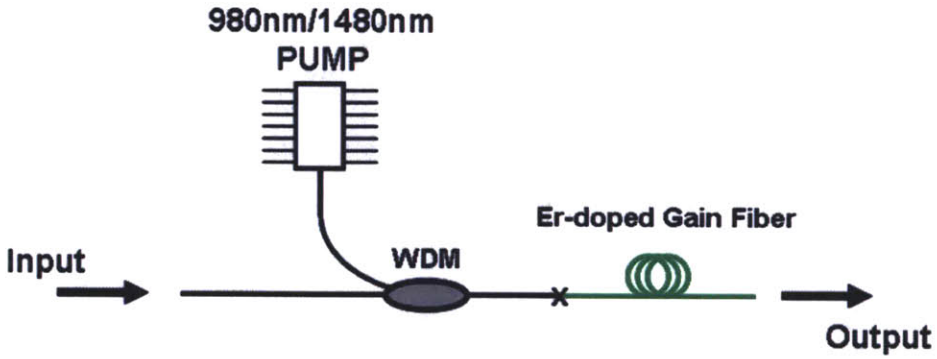

Figure 3-1: Basic fiber amplifier design. The design consists of a section of Er-doped gain fiber pumped at either 980nm or 1480nm using a WDM to combine signal and pump into the amplifier.

3.1.1 Amplification Scaling

Higher amplification levels are attained with increases in pump and/or increases in the number of amplification stages. Pump intensities can be scaled using a number of pump-

combining techniques, which take advantage of the spatial, spectral, and polarization properties of the pump for an ~8-fold increase. The second approach relies on scaling the number of amplifier stages. Stringing together successive amplifier stages can, in theory, provide unlimited gain. In practice, however, the losses associated with these additional stages act to clamp the gain to some finite quantity. These two approaches are analyzed to determine their realistic prospects for amplification scaling.

3.1.1.1 Pump-combining

Pumps can be combined in three general ways: spatial, spectral, polarization

- Spatial: Bi-directional pumping can, in general, be applied to double the available pump. In practice, however, only a ~63% increase can be realized because pumping in both directions requires the pumps to be protected with isolators (typical isolator insertion loss: ~1dB). Additional splice losses will drop this even further below 63%.
- Spectral: Erbium's dual absorption peaks allows for pumping at both 980nm and 1480nm. Pump diodes operating at those wavelengths can be multiplexed together for increased pumping capability.
- Polarization: Polarization beam-combining is achieved using a polarization dependent multiplexer to couple together pumps with orthogonal polarizations, one oriented in TE and the other in TM. Fused fiber polarization multiplexers provide high power handling and low multiplexing losses, which is ideal for polarization beam-combining.

A schematic of a single-stage design implementing all three pump-combining schemes is shown in Fig. 3-2. The 1550nm signal is first multiplexed with the polarization beam-combined 1480nm pump through a 1480/1550 WDM, and then multiplexed with the polarization beam-combined 980nm pump through a 980/1550 WDM (in that order; the reverse order requires custom WDMs). To get a rough idea of expected amplification levels, an estimate assuming only isolator losses (~1dB) calculates out to an amplification of ~826mW. Next, conservative estimates of ~10% insertion losses for each multiplexing element is incorporated, further reducing amplification to ~638mW. Therefore, pump-combining results in a 5-fold increase over a single pump design, at best.

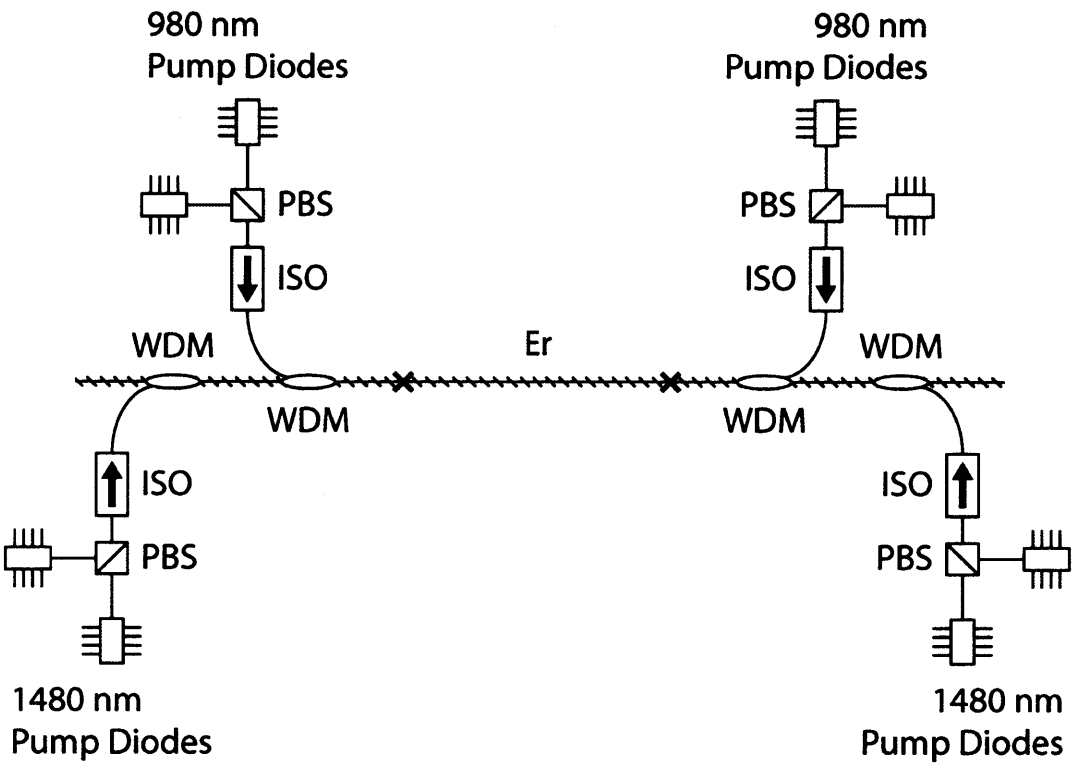

Figure 3-2: Schematic of a scaled-up high-power fiber amplifier. The single-stage amplifier is bi-directionally pumped with eight laser diodes, four at 980nm and four at 1480nm, using a combination of polarization and wavelength multiplexing.

3.1.1.2 Multi-stage Amplifiers

A three-stage amplifier was constructed to test the limits of this approach. A schematic of the setup is shown in Fig. 3-3. Here, each stage is identical in design to the amplifier pictured in Fig. 3-1. With 500mW of pump at 977nm, an optimized gain fiber length of 50cm was carefully determined using a cut-back approach. Isolators are placed between each stage to block backward-propagating ASE from otherwise stealing a good percentage of the gain. Losses from the isolator (~1 dB) and splices (~0.5% SMF-to-SMF, ~4.3% SMF-to- Gain Fiber) reduce the ~100mW gain per stage. With a 42 MHz, 88fs pulse train with 1mW average power seeding the amplifier, an output power of 241mW was achieved. This agrees well with the predicted three-stage gain of 225mW (calculated from the gain and loss values stated above).

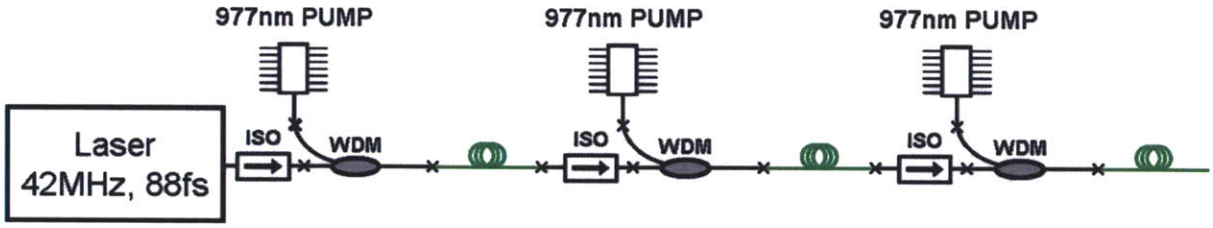

Figure 3-3: Three-stage amplifier chain. Each stage is pumped with a single 977nm laser diode outputting 500mW. An isolator separates each stage to prevent the amplification of backward ASE. In total, the amplifier outputs 241mW when seeded with a 1mW laser source.

Additional stages can be added to further increase signal gain via

$$P_{n+1} = \left(P_n \times \left(1 - L_{beforeGain}\right) + G\right) \times \left(1 - L_{afterGain}\right) \tag{3.1}$$

but at diminishing amounts with each additional stage. The amplifier chain will eventually saturate as the losses catch up to the gain. For the amplifier chain pictured in Fig. 3-3, a plot of signal gain as a function of stage number (Fig. 3-4) illustrates these diminishing returns. The signal gain will asymptotically approach a power level defined by

$$P_{sat} = \frac{G}{\frac{1}{\left(1 - L_{afterGain}\right)} - \left(1 - L_{beforeGain}\right)} \tag{3.2}$$

which is reached when additional stages impart zero signal gain, i.e. when the power out of the amplifier stage equals the power into the amplifier stage. In other words, the total achievable gain using multi-stage amplifiers is clamped by its losses. For the case considered above, the total achievable gain is limited to P_{sat} = 363mW.

3.1.2 Amplifier Design Considerations

Several design aspects for a new and improved amplifier are discussed, in order to provide a basis/explanation for the design choices that were made. As the above analysis showed, a combination of pump- and stage-combining may be able to get amplification near the Watt levels needed for a GHz pulse train (this depends on the accuracy of the estimated component losses and splice losses used in the analysis). This, however, would be extremely difficult since we'd be operating at the very edge of its limit. In addition, even if successful, such an approach could

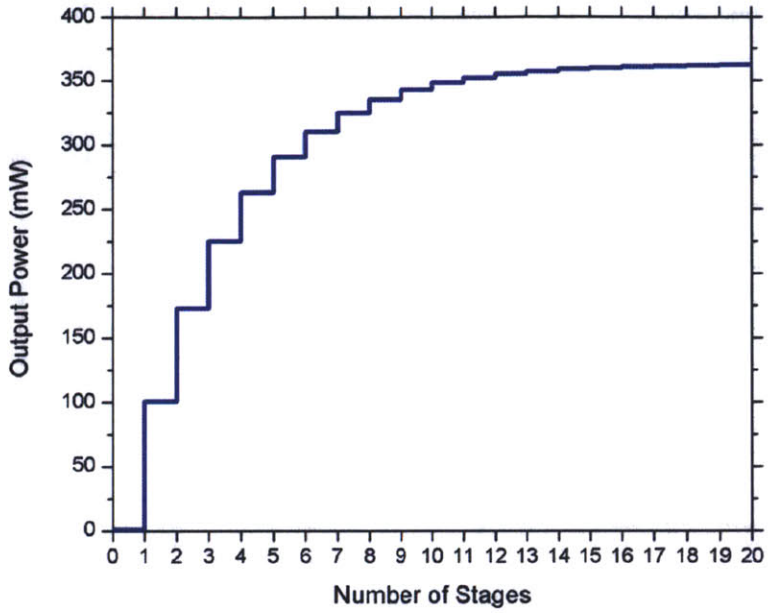

Figure 3-4: Projection of amplifier output power with increasing number of stages. The output power is clamped by amplifier losses, as the losses per stage eventually catch up to the fixed amount of gain per stage.

not be scaled much further. This has led us in search of a new approach to the amplification of ultrafast pulses – one that would not only work for our 1 GHz repetition rates, but hopefully one that could be scaled up to 10GHz, 20GHz, ...

Ultrafast amplifier designs are intended to increase pulse energy without negatively affecting any of the other properties of the pulse. One important rule-of-thumb is to minimize the accumulation of nonlinear phase during amplification. For example, CPA systems accomplish this by strongly chirping pulses, reducing pulse peak power, and thus the nonlinearity it experiences (since nonlinearity leads to pulse distortions, and potentially pulse breakup) [59]. For non-CPA systems, it's therefore important to use low-nonlinearity gain fiber, and for that gain fiber to be as short as possible. There's one additional constraint – the gain fiber needs to be normal dispersion (for reasons that will be made known shortly, i.e. compression-related). These constraints narrow our choice of gain fiber down considerably (as the need for low-nonlinearity and normal dispersion are competing factors). Of the gain fibers available, the Liekki 110dB/m Er-doped gain fiber is most suited for this application. It's a good compromise

between high-doping levels and low-nonlinearity[14]. That's, of course, if we stick to core-pumped singlemode gain fibers. If so, then we need a high-power singlemode pump source. Do such sources exist? Why aren't they more actively used for ultrafast applications? A source of this nature does exist – a Raman fiber laser providing up to 81 Watts of singlemode power at 1480nm [60]. Not surprisingly, there are drawbacks to using this pump technology for ultrafast applications. But can these drawbacks be corrected, or at least minimized? Before delving any further into this, let's consider the alternative – for the sake of comparison.

The alternative is to use multimode pump diodes, also capable of providing Watts of pump power, together with cladding-pumped gain fibers. The design/fabrication challenges related to the production of cladding-pumped gain fibers that are normal dispersion might not even make this option possible. Furthermore, and more importantly, cladding-pumped gain fibers fundamentally are not as efficient as core-pumped gain fibers with regards to pump absorption. This would mean longer lengths of gain fiber leading to excessive nonlinear phase accumulation during the amplification process. A third concern centers around the relative intensity noise of multimode pump diodes – but this is also a concern with the Raman fiber laser. Still it seems, for the previous reasons, the Raman fiber laser is the better option.

3.1.3 The Raman Fiber Laser Pump Source

The Raman fiber laser consists of a 1.06μm Yb fiber laser, followed by a cascade of nested fiber-bragg-gratings etched into a germanosilicate fiber to Raman frequency shift 1.06μm to 1.48μm in six precise steps (1060→1117→1175→1240→1315→1395→1480nm), Fig. 3-5. At its core is a Yb fiber laser operating at 1.06μm. Its high output powers are due to more efficient pump-to-signal conversion efficiency at 1.06μm. As a result, Yb fiber lasers have been demonstrated to operate at kilowatt powers [61]. The Raman gain spectrum in germanosilicate fibers covers the range 430 cm^{-1} – 440 cm^{-1}, but the integration of FBGs as high-reflectivity resonator mirrors makes the Raman shifting process both highly efficient and precise. The end result is a high-power singlemode pump source operating at 1480nm with a linewidth of ~1-2nm,

[14] OFS makes a more highly-doped gain fiber, spec'd at 150dB/m. But its nonlinearity is also ~2.3 times higher (A_{eff} = 14.5μm^2).

Figure 3-5: 1480nm Raman fiber laser. A CW Yb fiber laser operating at 1.06μm seeds a section of Raman gain fiber to Raman shift 1060nm to 1480nm. For germanosilicate fibers with Raman gain covering $430cm^{-1}$ – $440cm^{-1}$, this process takes six steps (1060→1117→1175→1240→1315→1395→1480nm). Six sets of fiber-bragg-gratings, each designed to be highly reflecting over a narrow bandwidth centered at one of the six intended wavelengths, form resonators to ensure precise conversion to the intended wavelengths. This leads to a high-power singlemode pump source at 1480nm.

and ~98% power contained in its main peak. Our 1480nm RFL, obtained commercially from IPG Photonics (Model# RLR-10-1480), has 10 Watt capability.

There are two potential drawbacks to using an RFL as a pump source. First, the relative intensity noise of such pumps may limit certain applications. The Yb laser that drives the RFL is itself pumped with multimode pump diodes that are noisy compared to the singlemode semiconductor laser diodes typically used in our setups. The RIN in these multimode pump diodes will transfer to the Yb laser, which then subsequently transfers to the Raman fiber laser. To quantify this, a RIN measurement was taken of the RFL output. This is shown in Fig. 3-6, along with the RIN from one of our JDSU singlemode pump diodes. One notices right away the increase in RIN associated with the RFL compared to the JDSU pump source. Two approaches may be used to combat this. First, feedback is always possible to reduce RIN. In our system, direct access to the multimode diode that's pumping the Yb laser can be used for feedback modulation. Feedback bandwidths are estimated to be limited to ~10kHz, but this should be more than enough since Erbium itself acts as a lowpass filter due to its relatively long upper-state lifetime (~1ms). Therefore, the RIN above ~10kHz, which presumably can't be suppressed with feedback to the pump, is instead suppressed by the Erbium gain process. As a result, there should be no reason why the RIN from a RFL after feedback can't be as good, if not better than the RIN out of the unstabilized semiconductor pump diodes typically used for our setups.

The second drawback is not fundamental to the RFL, but rather to our design goal of minimizing gain fiber length in order to minimize the amount of nonlinear phase shifts. The

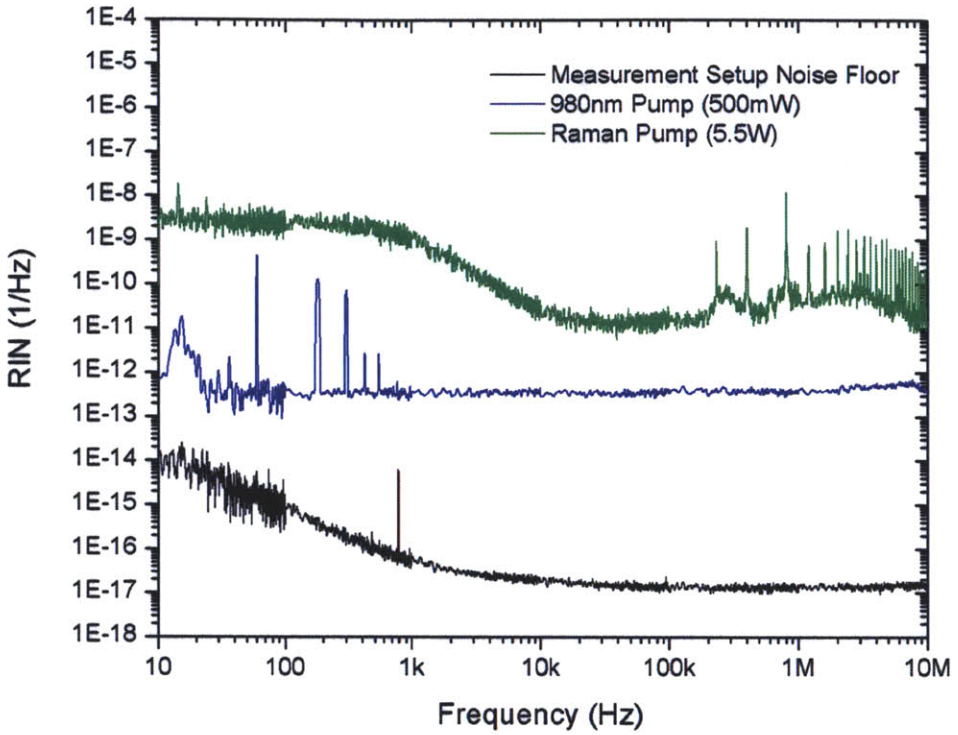

Figure 3-6: Comparison of relative intensity noise for different pump sources. The Raman fiber laser pump at 5.5W output powers (green) exhibits higher RIN compared to a JDSU semiconductor pump diode at 500mW output powers (blue) over the [10Hz,10MHz] range measured. RFL RIN at frequencies below 10kHz can be suppressed using feedback to the Yb fiber laser seeding the RFL, and RFL RIN at frequencies above 10kHz is naturally filtered by the long upper-state lifetime of Erbium (~1ms).

drawback relates to the fact that Erbium gain fibers, including the one used in our amplifier setup, have much higher absorption at the 980nm peak compared to the 1480nm peak. This means that a longer length of gain fiber will be needed to absorb pump at 1480nm compared to what would be needed to absorb pump at 980nm. This is investigated, and more thoroughly chronicled in the ensuing amplifier development section.

3.1.4 Amplifier Optimization

The 10pJ, 360fs GHz repetition rate laser pulses will need to be amplified up to ~1 nJ pulse energies (and compressed down to ~100 fs pulse durations) before they can be used to generate an octave of usable spectrum with existing HNLFs – this means an amplifier providing >20 dB

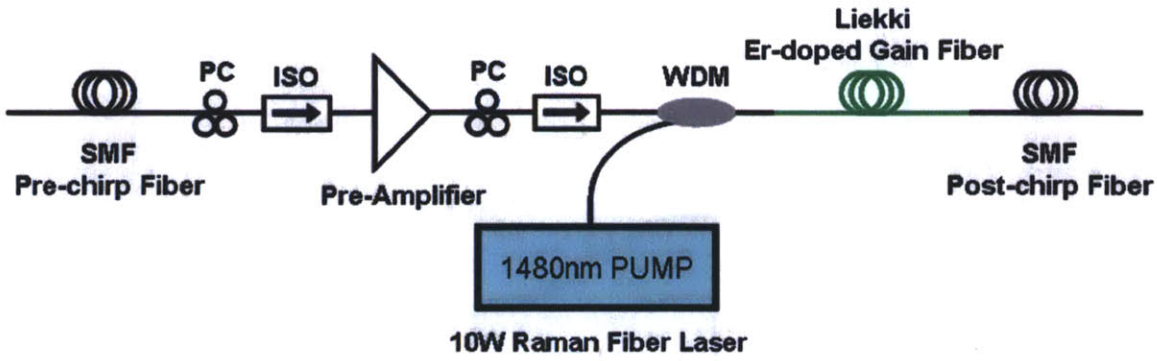

Figure 3-7: High-power amplification and femtosecond-pulse compression setup. A pre-amp amplifies the input pulse train to 65mW to ensure saturation of the power-amp, which consists of 1.2m of Liekki 110dB/m normal dispersion gain fiber pumped by a 10W Raman fiber laser operating at 1480nm. SMF fiber pre-chirps the pulses so that nonlinearity is minimized during the beginning and middle stages of amplification. The pulses become transform-limited towards the latter stages of amplification to generate compressible spectrum via self-phase modulation. SMF fiber (or gratings/prisms/LMA-fiber) is used for post-chirp compensation.

gain is needed (along with 3.6x pulse compression). The configuration of the system is depicted in Fig 3-7. To ensure saturation of the RFL-pumped EDFA, the laser output is first pre-amplified to 65mW in a 980nm-diode-pumped 50cm section of 110dB/m Er-doped gain fiber. The next stage of amplification is comprised of the Raman fiber laser, capable of outputting up to 10W of power at 1480nm, pumping a section of the same highly-absorbing fiber used in the pre-amplifier. The gain fiber's high absorption ensures that only a short length is needed to extract most of the pump, thus minimizing the amount of nonlinear phase shift accumulated during the amplification process. An optimal gain fiber length of 1.2m is determined using a cut-back procedure maximizing the conversion of pump to signal power, yielding amplified pulses with energies greater than 2nJ (~2W output for 5W pump). When this approach was used initially for gain fiber length optimization, more than half the gain was lost to back-reflections from the output end of the gain fiber. We have since taken better care in eliminating these back-reflections by angle-cleaving the gain fiber during the cut-back process, achieving a two-fold increase in output power. A plot of the amplifier's performance for a range of pump powers is shown in Fig. 3-8. Also shown in Fig. 3-8 is an earlier plot taken when back-reflections were not eliminated. At low pump powers, the output powers between the two are similar since back-reflections are weak compared to the input. This difference in output powers increases with

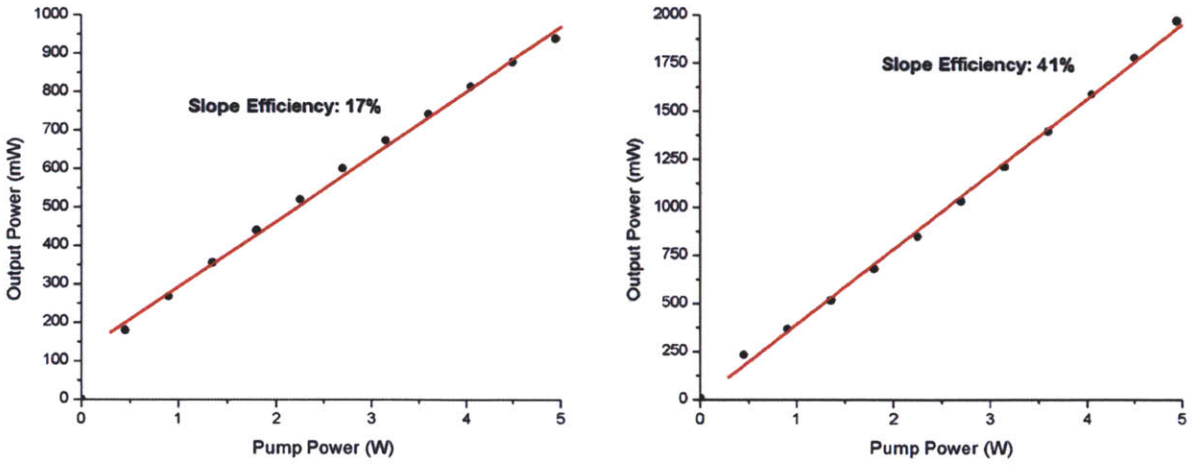

Figure 3-8: Amplifier performance. A non-optimized amplifier with back-reflections stealing a large percentage of the gain leads to a slope efficiency of 17% (and a conversion efficiency of 19% at 5W pump). Elimination of back-reflections results in an improved slope efficiency of 41% (as well as an improved conversion efficiency of 41% at 5W pump).

increasing pump powers. At 5 Watts pump, the non-optimal amplifier has 1 Watt output – this corresponds to back-reflections of 40mW (4%) which is now comparable with the 65mW input, meaning that nearly half of the gain is stolen by the back-reflected signal. It turns out that eliminating this source of back-reflection doubles our output power, and more than doubles our pump-to-signal conversion efficiency. Note that the ~41% conversion efficiency is more than we have gotten from any of our previous amplifier systems.

It's surprising that only 1.2m of gain fiber was needed to provide 41% pump-to-signal conversion efficiency, given the lower absorption peak at 1480nm. For comparison, the 980nm-pumped pre-amplifier needed 50cm of the same gain fiber to absorb 10x less pump (500mW). In any case, drawback #2 for the use of RFLs has been proven to not be a drawback after all. Therefore, both initial concerns for the use of RFLs in ultrafast systems have been resolved. The RFL should now be considered a viable candidate as a pump source for any ultrafast application.

3.2 Ultrafast Pulse Compression

The pulse compression component of the system is based entirely on spectral generation during amplification in the normal dispersion gain fiber, which is accomplished through careful optimization of the pre- and post-chirp fiber lengths. A segment of anomalous dispersion pre-

chirp fiber (SMF-28e) is inserted before the pre-amplifier to minimize nonlinearities in the beginning stages of amplification. The amount of pre-chirp is carefully optimized so that the pulses compress back to their transform limit near the end of the amplifier, where they will experience intense nonlinearities and thereby generate more than sufficient spectrum to both compensate for gain narrowing during the amplification process and permit further compression. It is important that the gain fiber be chosen to have normal dispersion, as this leads to SPM-dominated spectral generation whereby the resulting chirp is largely linear and compressible [62].

Fig. 3-9 (red curve) shows the broadened spectrum at the gain fiber output resulting from 1.1m of pre-chirp fiber. The nearly symmetric broadening is characteristic of SPM, which is to be expected when operating in the normal dispersion regime. The spectrum out of the amplifier is broadened to a FWHM of ~25nm, which is a 3.5 times increase over the spectrum directly out of the oscillator. The resulting chirp can be largely compensated for using a pair of gratings or

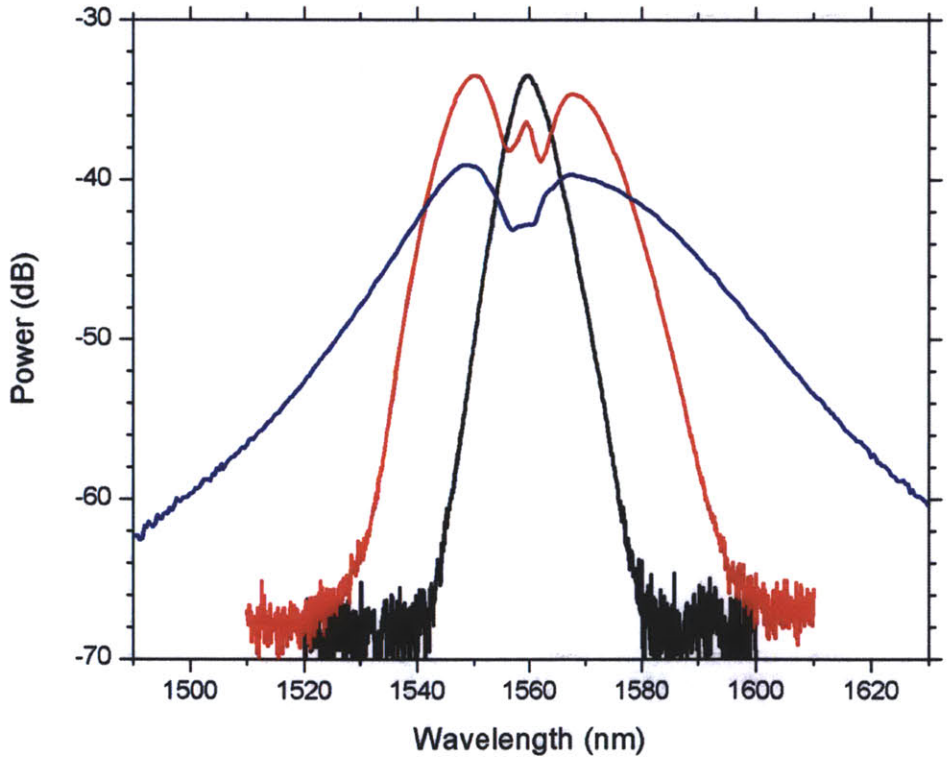

Figure 3-9: Spectral generation in the amplifier and post-compression fiber. The laser output (black) is first spectrally broadened in the normal dispersion gain fiber (red) to a FWHM of 25nm. The resulting spectral features are characteristic of self-phase modulation, as expected. Further broadening in the anomalous dispersion SMF post-chirp fiber (blue) leads to a FWHM of 41nm.

prisms. Fiber can also be used to provide the necessary amount of anomalous dispersion, as long as nonlinearities are minimized during the process. In our setup, the fiber option is preferred as it eliminates the need to go in-and-out of fiber and the losses this entails. At our current pulse energies, compression in standard singlemode fibers is possible with minimal distortions to pulse quality. Fig. 3-9 (blue curve) shows the spectrum after 0.9m of SMF-28e post-chirp fiber, and autocorrelations (Fig. 3-10) indicate a compressed pulse duration of 95fs (assuming a sech^2 fit) with only a slight pedestal.

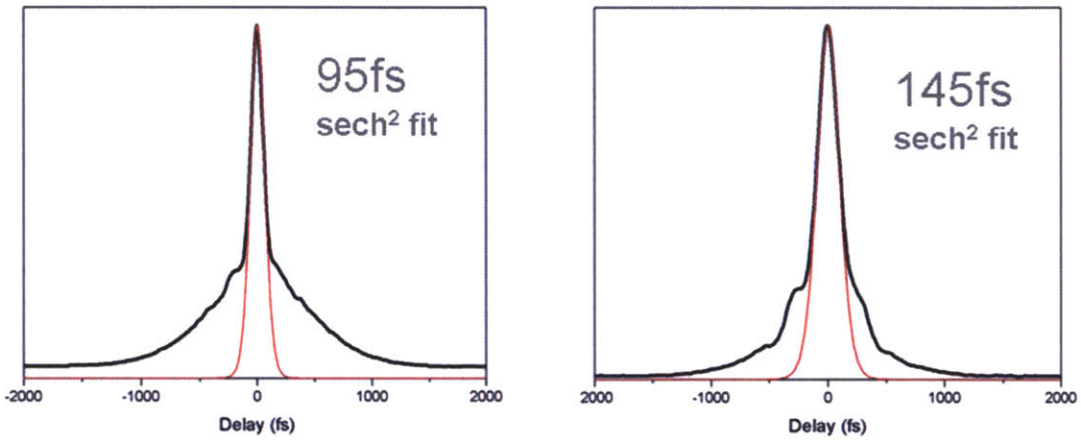

Figure 3-10: Autocorrelation traces representing pulse compression with and without additional nonlinearities. Compression without additional nonlinearities (e.g. gratings/prisms/LMA-fiber) leads to 145fs duration pulses while compression with additional nonlinearities (e.g. SMF fiber) leads to 95fs duration pulses. The additional nonlinearities lead to shorter pulses at the expense of increased pedestal.

In order to determine if the pedestals are from the use of SMF-28e for chirp compensation (as the additional spectral broadening in Fig. 3-9 suggests), a further experiment was conducted to simulate low-nonlinearity conditions (i.e. to mimic the use of LMA fibers for chirp compensation). To do this, the amplified output was attenuated so that only ~0.05% (1mW) was coupled back into a 1.4m length of SMF-28e post-chirp fiber to compensate for chirp resulting from the spectral broadening process. This should eliminate any nonlinearities we may have faced earlier. Notice that a longer piece of the same post-compression fiber is needed to compensate for the chirp at low powers. The spectrum at the post-compression fiber output was no different from that out of the gain fiber (see Fig. 3-9), and the pulses can now be compressed

down to only 145fs, as the autocorrelation trace shown in Fig. 3-10 indicates. As expected, the pedestals are certainly less severe, but pulse duration is sacrificed.

Chapter 4

Octave-spanning Supercontinuum Generation Experiments*

HNLFs are enabling the generation of supercontinuum spectra spanning multiple octaves, achieving high nonlinearities over long interaction lengths through tight waveguiding confinement. Compared to SCG in bulk media, SCG using highly nonlinear optical fibers provide better performance with lower seeding requirements. From conventional small-core step-index fibers to more advanced photonic crystal geometries, HNLFs can be designed for maximum spectral broadening, as well as for the generation of very specific frequencies. For applications requiring flat continuum generation, HNLFs also exist.

For f-2f self-referenced f_{ceo} detection, an octave-spanning spectrum is required. However, it's undesirable to generate much more than an octave as this just spectrally spreads out the available power over more frequencies, thus reducing power at λ_f and λ_{2f}. Instead, SCG with amplified λ_f and λ_{2f} regions would be best. Such HNLF designs are now possible with better understanding of the processes responsible for SCG. Powerful numerical models, which can accurately predict the complex temporal and spectral structure resulting from SCG in HNLFs, can be exploited for these specific designs. A host of different HNLF architectures were investigated to determine which HNLFs were best suited for octave-spanning SCG. The results

* With contributions from Jason Sickler

of these experiments are presented, followed by a discussion comparing the fibers for subsequent f_{ceo} detection and stabilization. The importance of coherent SCG is also discussed in relation to this.

4.1 SCG Theory

The physics behind SCG is now generally well understood to consist of three general processes: self-phase modulation (SPM), stimulated Raman scattering (SRS), and self-steepening (SS). The first two fall under the more general heading of four-wave mixing, a 3rd order nonlinear process where three fields interact in a nonlinear medium to generate a fourth field. Their dominance in SCG is due to the fact that these processes are automatically phasematched, so special conditions don't need to exist for their effects to be realized (i.e. their conversion efficiencies are maximized at all times and for all circumstances). Self-steepening is also a consequence of the Kerr effect, as temporal pulse steepening results from the intensity-dependent refractive index. The generalized Nonlinear Schrödinger Equation provides a comprehensive model for these effects.

4.1.1 SCG Modeling via the Generalized NLSE

The generalized NLSE is used to model pulse propagation,

$$\frac{\partial E}{\partial z}+\frac{\alpha}{2}E-\sum_{k\geq 2}\frac{i^{k+1}}{k!}\beta_k\frac{\partial^k E}{\partial \tau^k}=i\gamma|E|^2E-\frac{\gamma}{\omega_0}\frac{\partial}{\partial\tau}\left(|E|^2E\right)-i\gamma T_R E\frac{\partial}{\partial\tau}|E|^2 \qquad (4.1)$$

It takes into account propagation loss (α), as well as all orders of dispersion (β_k). The three nonlinear processes mentioned above are accounted for on the right hand side: SPM, SS, SRS (in that order). This PDE is generally solved using the split-step method [63], where the dispersion terms are handled in the frequency domain, and the nonlinear processes in the time domain. Very good quantitative agreement between simulation and experiment can be achieved with such a scheme.

4.1.1.1 Modeling SCG Coherence

Coherence is important for f_{ceo} detection since it involves the beating of the two spectral ends of the octave-spanning supercontinuum (where coherence is typically at its worst). Without coherence, no beat will be detected. In general, the level of coherence determines the strength of a detected beat. Dudley et al. has shown that the coherence of the SCG process can be predicted to first order [64]. They do this by averaging over an ensemble of simulated traces, each trace obtained with some random noise at the input, i.e.

$$\left|g_{12}^{(1)}(\lambda)\right| = \left| \frac{\left\langle \tilde{A}_1^*(\lambda)\tilde{A}_2(\lambda)\right\rangle}{\sqrt{\left\langle \left|\tilde{A}_1(\lambda)\right|^2\right\rangle\left\langle \left|\tilde{A}_2(\lambda)\right|^2\right\rangle}} \right| \tag{4.2}$$

Coherent SCG would be immune to this noise, so any SCG dependence on noise at the input means phase-coherence at the output is poor. Their results indicate that coherence requires short pulses (sub-100fs) and short segments of HNLF. Coherence, of course, is only of real concern for SCG in the anomalous dispersion regime, as soliton fission (i.e. the splitting of higher-order solitons into multiple fundamental solitons) is the main cause for loss of coherence. In the normal dispersion regime of operation where SPM dominates, SCG is very phase-coherent. This regime of operation, however, doesn't produce optimal broadband SCG. It's the soliton effects which both help, and hurt, SCG. For this reason, it's extremely important that our seed pulses have durations of ~100fs.

4.2 Different HNLF Architectures

The two important parameters for SCG are nonlinearity and dispersion, and it's the interplay between the two that determines SCG. Specifically, nonlinearities should be maximized, as they are the fundamental base for spectral broadening; and dispersion should be minimized, as it acts to diminish nonlinearities through peak power reduction. Both nonlinearity and dispersion depend on material and waveguide properties. Nonlinearity is determined by

$$\gamma = \frac{n_2 \omega_0}{c A_{eff}} \tag{4.3}$$

where n_2 is the material nonlinearity and A_{eff} is the effective mode confinement area. Dispersion, too, consists of material and waveguide components. Therefore, different HNLF architectures have been developed to provide enhanced nonlinearity with minimal dispersion. Typically the material is silica (though other materials such as chalcogenide glass have also been employed); so that establishes material nonlinearity and dispersion. Waveguide design, on the other hand, can be manipulated to match overall nonlinearity and dispersion to specified quantities. Small-core step-index silica fibers and photonic crystal fibers are two of the most common types of HNLFs (pictured in Fig. 4-1). These are the two architectures considered in this thesis.

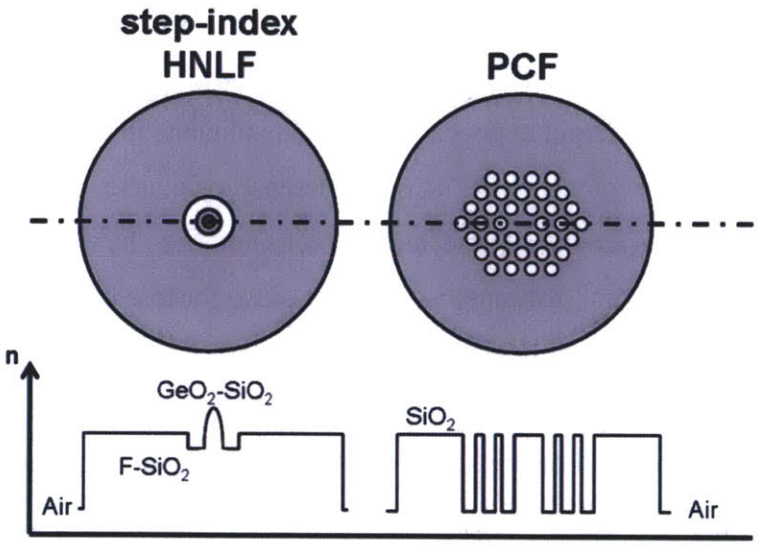

Figure 4-1: Examples of the two most common HNLF architectures. Step-index HNLFs define their core size and dispersion profile through doping, while photonic crystal fibers define these same parameters through the geometry of their air holes. PCF designs allow for greater control of nonlinearity and dispersion, while step-index HNLFs are more easily integrated with standard singlemode fibers.

4.2.1 Small-core Step-index HNLFs

These types of fibers confine light based on a refractive index difference between the fiber core and cladding. Different dopants are used to define the core from the cladding. Parameters such as the core size, refractive index difference, etc. can therefore be adjusted to control both

dispersion and nonlinearity. In dispersion-shifted fibers, for example, the zero dispersion point is shifted from 1.3μm (pure silica) to its intended region of operation using such an approach [65]. Recently, it's been demonstrated that the dispersion profile of these fibers can also be fine-tuned using UV-irradiation [66].

4.2.2 Photonic Crystal Fibers

PCF HNLFs typically consist of a solid silica core surrounded by a cladding region made up of a traverse array of air holes. Their dispersion and nonlinearity parameters are controlled by the orientation of these air holes, and engineering this geometry (via pitch and air fill fraction) can lead to drastic changes in both. The advantages of PCF compared to step-index fiber are that its architecture allows for much greater freedom in the tailoring of dispersion and nonlinearity. This has, for example, led to designs with orders of magnitude smaller A_{eff}, as well as designs with multiple zero dispersion crossing points, e.g. 4 ZDWs between 1100 – 1700nm [67]. Its main disadvantage compared to step-index fiber is its incompatible mode sizes compared to standard singlemode fibers. This leads to much higher coupling losses, thus weakening SCG if it can't compensate for these losses with high enough nonlinearities.

4.3 SCG Experiments

A number of HNLFs were tested (7 in total: 2 PCFs, 2 conventional small-core step-index dispersion-shifted fibers, 3 small-core step-index dispersion-shifted fibers with additional UV treatment for additional dispersion tailoring). The fibers all have minimal dispersion at 1550nm – though some anomalous dispersion is desired to take advantage of soliton effects for SCG. Recall that these effects help lead to broader continua (e.g. via soliton self-frequency shifts), but instabilities due to soliton fission can also lead to destruction of coherence in the generated continuum. To prevent this destruction of coherence, nJ/sub-100fs pulses are used for the following SCG experiments, together with short lengths of HNLF.

4.3.1 The Seed Source(s)

Because the samples were obtained at different times, two different seed sources were used, albeit with similar pulse energies and durations. These two systems consisted of similar, but not identical, 200 MHz soliton laser sources, one home-built (described in Sec. 2.1.1) and the other a commercial Menlo Systems product. The commercial system had similar output pulses (and output spectrum) to the home-built system (see Fig. 2-3). Both sources, however, used the same commercial Menlo Systems amplifier bi-directionally pumped with four total pump diodes to give amplifications of ~275mW, Fig. 4-2. Spectral broadening at the amplifier output, followed by SMF chirp compensation gave ~1.4nJ pulse energies and ~50fs pulse durations, also Fig. 4-2.

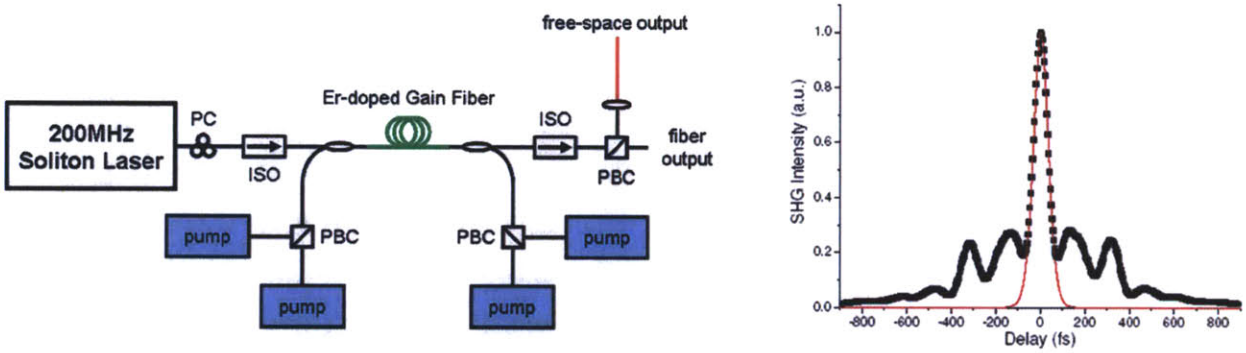

Figure 4-2: The 200MHz rep rate 1.4nJ/50fs source used for the supercontinuum generation experiments.

4.3.2 The SCG Traces

SCG plots for the different HNLFs tested are presented here. Two different setups were used for these experiments, one setup specifically for the PCFs since they required free-space coupling into and out of the HNLF, and the other for the Furukawa and OFS step-index fibers which uses an all-fiber configuration. The two setups are depicted in Fig. 4-3. The laser/amplifier/compressor sections of both setups are identical. Only the coupling portion of the setup is modified for free-space versus fiber coupling. Results for the best fibers in each group are presented.

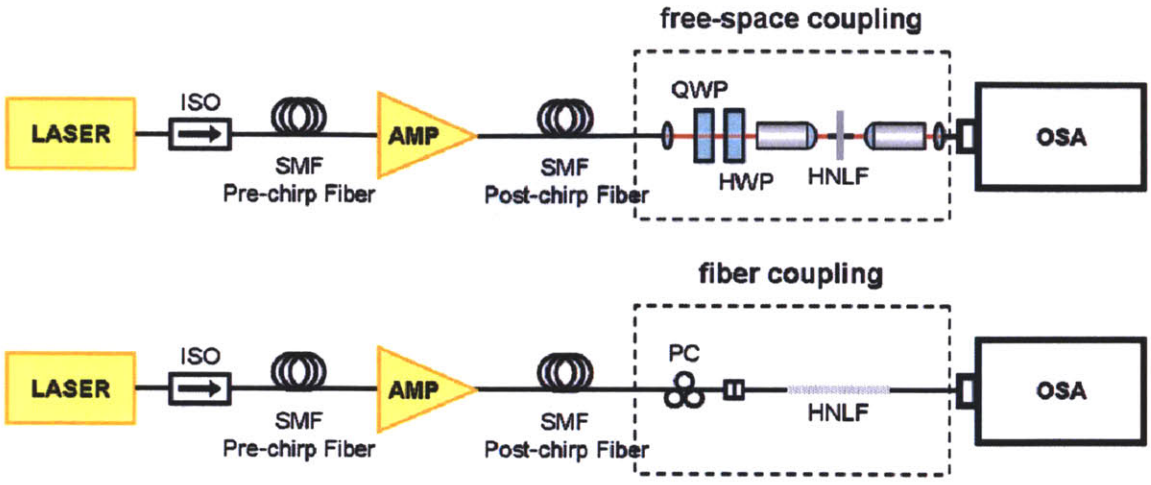

Figure 4-3: The free-space and fiber setups used for coupling in-and-out of the various HNLFs tested. The PCFs required free-space coupling, while the step-index HNLFs were spliced to connectors and fiber coupled.

SF6 and Tellurite PCFs

PCFs made of both SF6 and Tellurite were tested. These fibers were obtained from Prof. Omenetto's Group at Tufts University - they were able to generate multiple octaves using sub-centimeter pieces with OPO input pulses [68]. Tests with our seed pulses didn't generate nearly as much spectrum with centimeter long pieces of SF6 PCF, as shown in Fig. 4-4. Two traces are shown, one taken with the OSA which could only measure out to 1700nm. A spectrometer was used to capture the remaining spectrum past 1700nm. Clipping occurred in our lock-in amplifier as the sensitivity was set high enough to measure signals 30dB down from the peak so that it wouldn't be lost in the noise. Approximately 137mW of the incident 205mW was coupled into the fiber to generate supercontinuum spanning 1250nm – 2000nm (30dB down from peak). The Tellurite PCF performed much worse, producing very little SCG. Follow-up discussions with the Omenetto Group confirmed our results; but it also revealed that only slightly higher pulse peak powers would have caused the continuum to explode by over three octaves – this is actually not what we want…

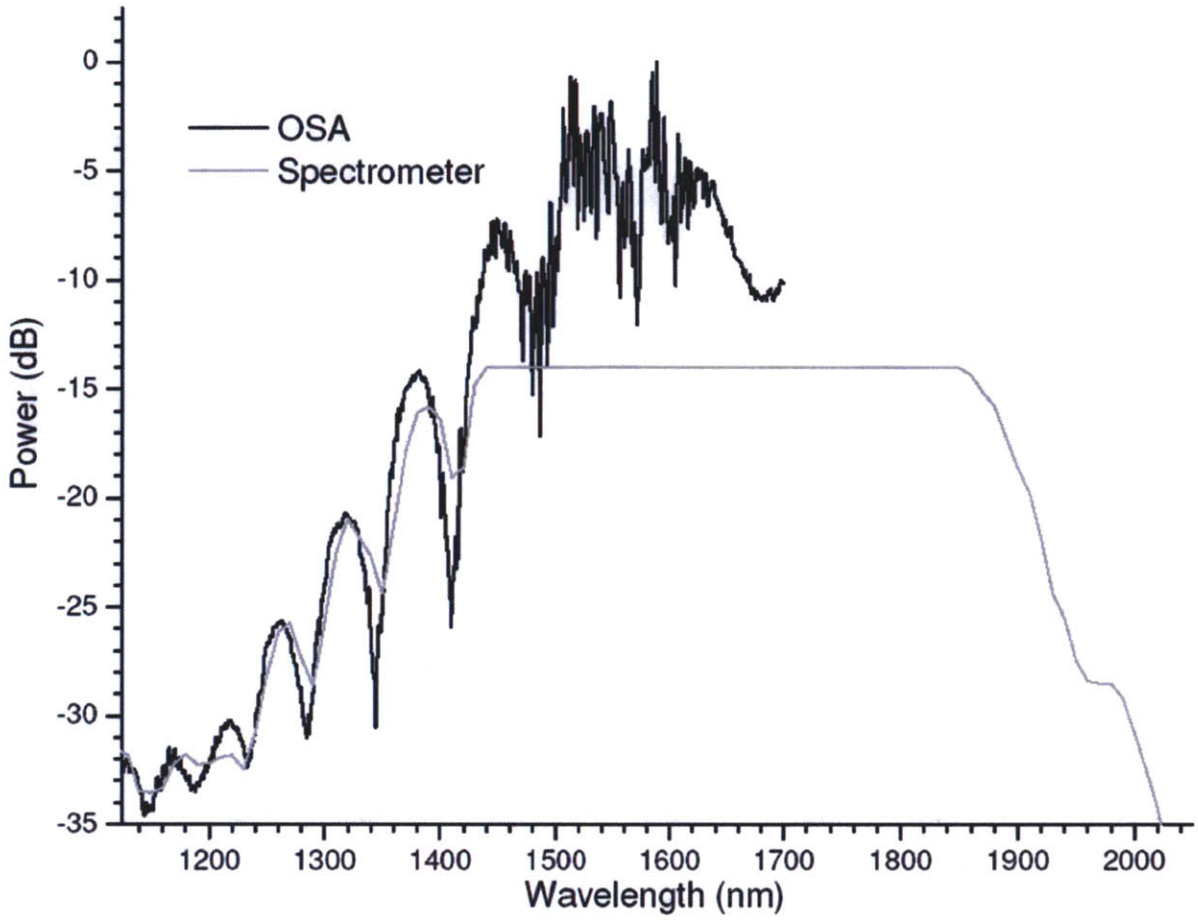

Figure 4-4: Supercontinuum generation from the SF6 PCF. The continuum spans 1250nm – 2000nm 30dB down from the peak, which is not quite an octave. The spectrometer trace (gray) is clipped as a result of the lock-in detection sensitivity being set to detect signals 30dB down from the peak. An OSA trace (which only measures out to 1700nm) is used to determine the spectral peak.

Furukawa HNLF Samples #1 and #2

Two different types of PM-HNLF samples were obtained from Furukawa, labeled Sample #1 and Sample #2. Sample #1 consistently performed better, so its results are presented here. A 50cm length of this HNLF was spliced to Hi1060 fiber on both ends. One end was connectorized to the seed source, and the other end sent into a spectrometer for diagnostics. The resulting supercontinuum trace, Fig. 4-5, spans an octave at 15dB (λ_f) and 20dB (λ_{2f}) down from the peak.

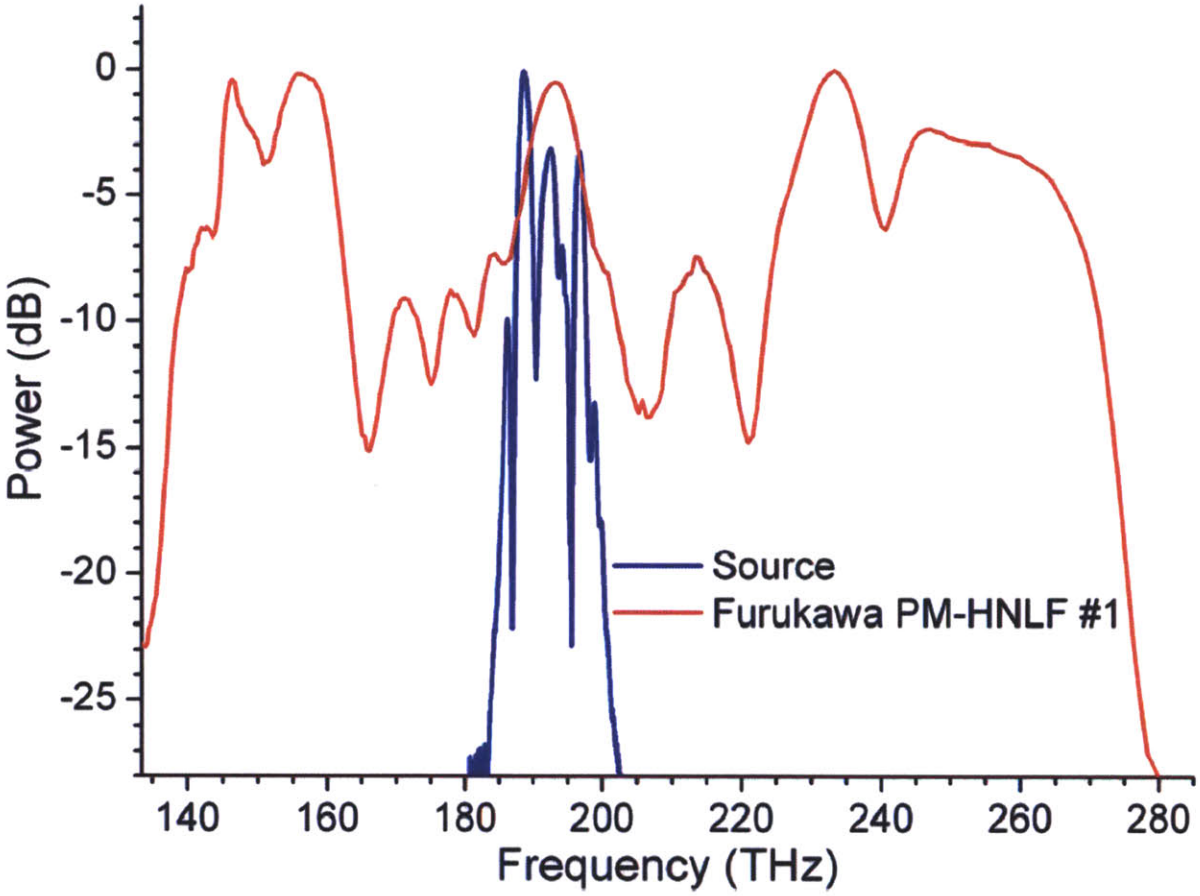

Figure 4-5: Supercontinuum generation from the Furukawa PM-HNLF #1. An octave of continuum is obtained 15dB and 20dB down from the peak using 50cm of HNLF.

OFS HNLF Type A, B, C

Three different types of OFS HNLF with different UV-irradiation levels were tested, referred to as Type A, B, and C. Types B and C produced octave-spanning spectra with our seed source while Type A did not. Below are the results for Types B (as Type C produced much lower powers at the f and 2f portions of its continuum), Fig. 4-6. This HNLF, ~11 cm in length, had optimized splices to SMF fiber on both ends. The f and 2f sections of this fiber were only 11dB down from the peak.

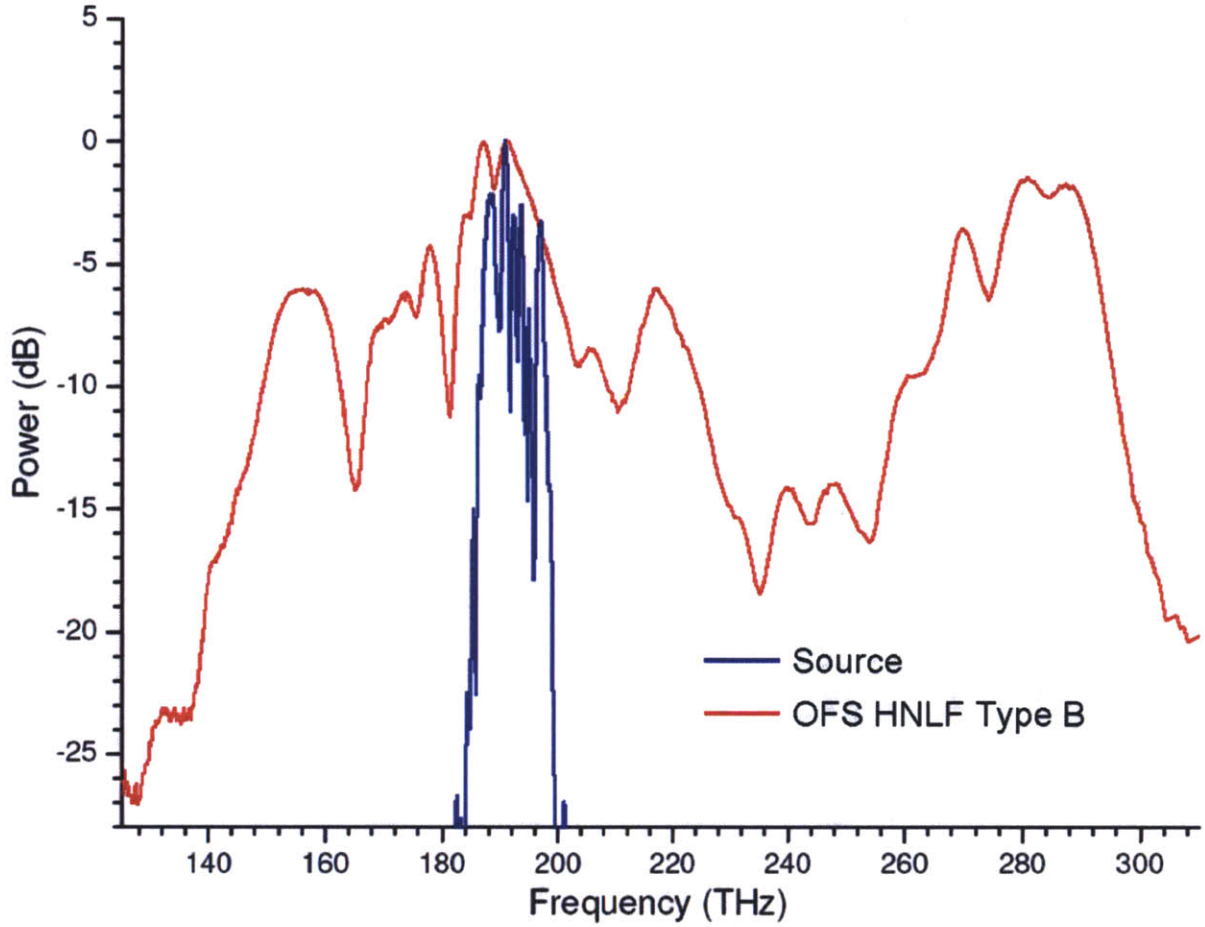

Figure 4-6: Supercontinuum generation from the OFS HNLF Type B. An octave of continuum is obtained 11dB down from the peak using 11cm of HNLF.

4.3.3 HNLF Selection

Of the three groups of HNLFs tested, the PCFs generated the least spectrum, failing to produce an octave. On top of that, these HNLFs require free-space coupling which would be more prone to environmental noise – our preference is to remain in fiber for the reasons mentioned throughout this thesis. Between the two small-core step-index HNLFs, the Furukawa HNLF needed 50cm to generate an octave (compared to only 11cm of OFS Type B HNLF), meaning the f-2f coherence could be jeopardized. It is for these reasons that we chose to go with the OFS HNLF Type B. It generates an octave of supercontinuum, with a good portion of it concentrated in the f and 2f sections used for f_{ceo} detection. It also produces the octave in only

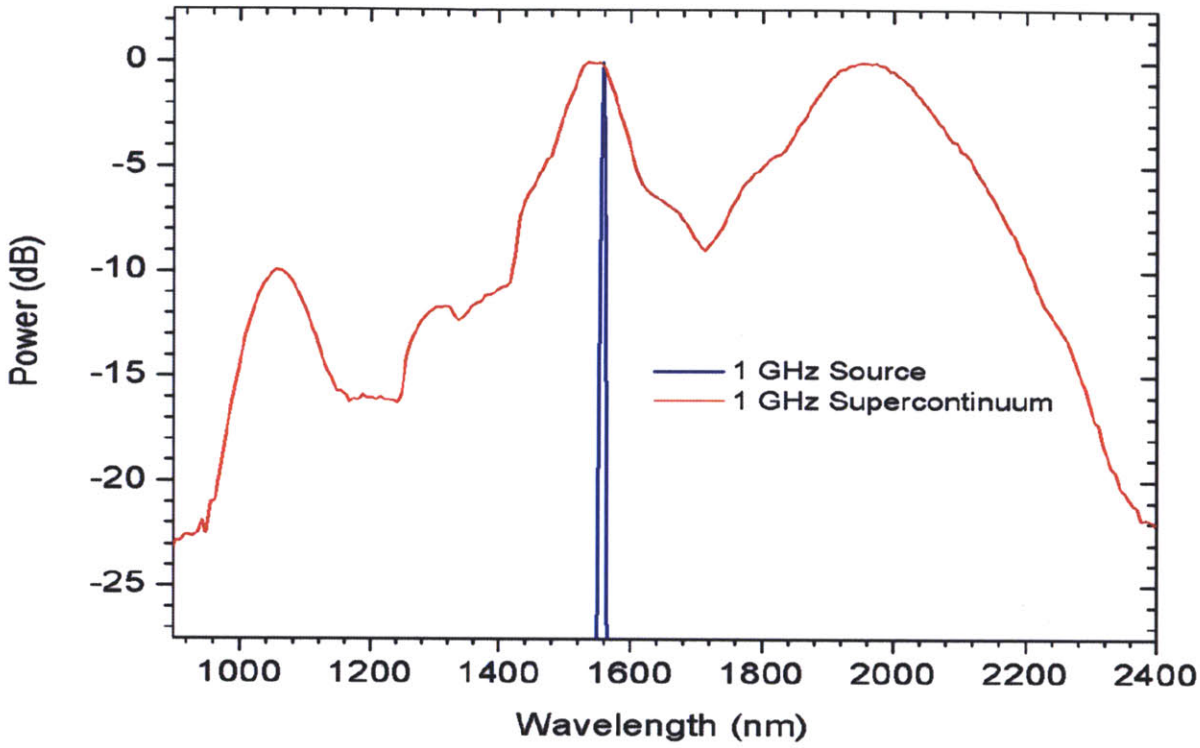

Figure 4-7: The octave-spanning supercontinuum generated with the 2nJ/95fs GHz pulses using 11cm of OFS HNLF Type B. The continuum spans 1μm – 2.4μm, with a peak at 2μm (and the 1μm peak is only ~10dB down). This corresponds to 65mW and 7mW, respectively, over a 10nm bandwidth at those f and 2f wavelengths.

11cm, which with 1nJ/100fs pulses, should preserve the phase coherence. Fig. 4-7 shows the octave-spanning supercontinuum generated with our 2nJ, 95fs GHz repetition rate pulses. The differences between this trace and the one shown in Fig. 4-6 are due to the different seed sources. Surprisingly, this SCG appears more optimal, even though longer duration pulses were used for its generation. This should be more than sufficient for f_{ceo} beat detection (assuming phase-coherent SCG) and stabilization, which is the topic of the next chapter (Chapter 5).

Chapter 5

Self-referenced f_{ceo} Beat Detection and Stabilization & Optically-stable Frequency Combs*

The ultrafast high-power amplification, femtosecond-pulse compression, and octave-spanning supercontinuum generation techniques were developed for the purpose of f_{ceo} detection and stabilization. An octave of supercontinuum, resulting from sub-100fs nanojoule pulses in HNLF, is used to facilitate a self-referencing scheme for f_{ceo} detection. Once detected, stabilization is carried out through both internal and external cavity feedback. Results from both approaches are presented, analyzed, and compared. This, along with f_{rep} stabilization (described in Sec. 2.1.2.4.4), completes the frequency comb – the first GHz-repetition-rate frequency comb centered at the 1.5μm telecom band (to the best of our knowledge).

An optically-stable technique for frequency comb stabilization is presented to further improve the stability of frequency combs. The technique involves difference frequency generation locking to a methane-stabilized HeNe optical reference, enabling extremely tight stabilization of the laser repetition rate. Proof-of-concept experiments were conducted to show

* With contributions from Andrew Benedick, Guoqing Chang, Jonathan Cox, Jason Sickler

the validity and performance benefits of this scheme, with demonstrated improvements to frequency comb stability of one to two orders of magnitude.

5.1 Self-referenced f_{ceo} Beat Detection

Carrier-envelope offset frequency beat detection is accomplished using an f-2f self-referencing scheme, whereby detection of f_{ceo} occurs through the beating of its own frequency components, not those of an external reference oscillator. This generally requires an octave of spectrum, though other less-efficient beating combinations do exist if an octave cannot be obtained. Those combinations, however, may not generate a beat strong enough for stabilization, as it's already difficult enough using f-2f self-referencing. These difficulties are described, along with the strategies employed for overcoming them.

5.1.1 f-2f Interferometer Setup

Fig. 5-1 illustrates our experimental setup for f-2f f_{ceo} self-reference detection. An f_{ceo} heterodyne beat is detected using the f and 2f ends of the generated continuum, denoted as λ_f and λ_{2f}, respectively. Since the phase-matching for second harmonic generation is sensitive to incoming polarization, λ_f and λ_{2f} are first separated at the output of the HNLF so that their polarization can be independently adjusted before they are recombined and focused into the PPLN for SHG. λ_f's polarization is adjusted to optimize SHG conversion and λ_{2f}'s polarization is adjusted to optimize the strength of its beating with λ_f. The relative delay between λ_f and λ_{2f}, due to dispersion in the HNLF, also needs to be compensated, and is done so using a retro-reflecting translation stage in the λ_{2f} arm of the interferometer. Also, steering mirrors in each interferometer arm optimize for spatial and angular overlap of the λ_f,λ_{2f} beams. After SHG, λ_f,λ_{2f} are passed through a series of dielectric filters (1100nm cutoff lowpass, 10nm 1012nm-centered bandpass, 1.5nm 1012nm-centered bandpass) to eliminate everything but λ_f,λ_{2f}. A set of 25mm and 40mm focal-length plano-convex lenses maximizes coupling into a Hi1060 fiber-pigtailed collimator, which is used for alignment and delivery of λ_f,λ_{2f} to an InGaAs APD to generate the f_{ceo} beat.

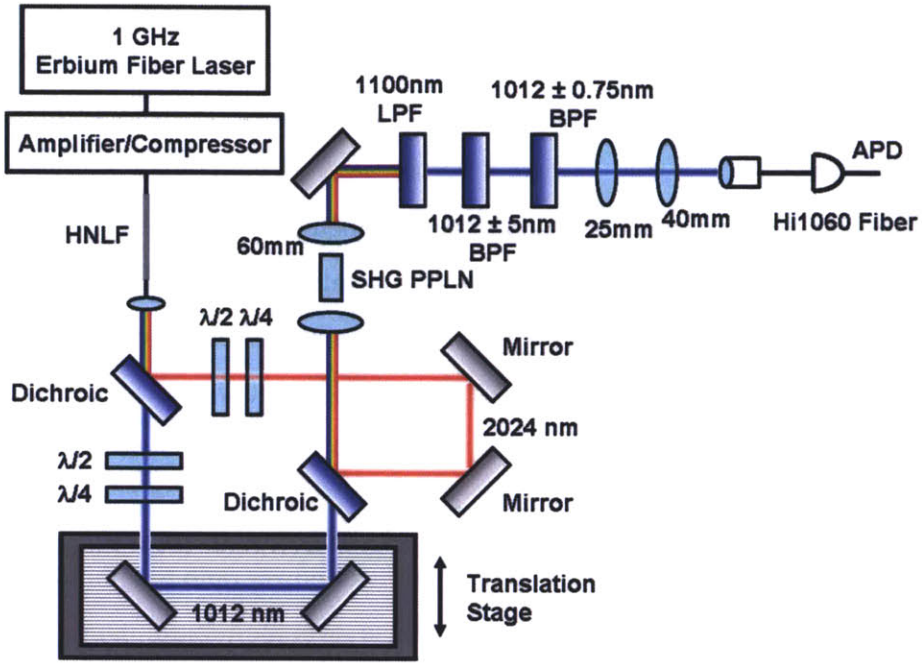

Figure 5-1: The f-2f interferometer for f_{ceo} beat detection. The f (2024nm) and 2f (1012nm) ends of the supercontinuum are first separated so that their temporal, spatial, angular, and polarization overlap can be optimized before SHG. Identical 60mm lenses are used to focus into and re-collimate after the SHG PPLN, which is phasematched for SHG at 2024nm with 2.5nm bandwidth. A series of dielectric lowpass and bandpass filters ensures transmission of only λ_{FUND} and λ_{SHG} to minimize shot noise and maximize fceo SNR. A set of 25mm, 40mm, and 11mm lenses optimally couples λ_{FUND} and λ_{SHG} into Hi1060 fiber, which are then directed into an APD for f_{ceo} beat detection.

5.1.2 f_{ceo} Beat Detection Strategies

A number of design decisions were taken into careful consideration for generating an optimal f_{ceo} beatnote. In this case, optimal means maximum signal-to-noise. Many of the strategies considered here stem from difficulties in achieving a large enough signal-to-noise for stable phase-locking. From experience, this is an SNR of 30 dB in a 100 kHz RBW. As a result, many of the components involved in this process have been thoroughly analyzed so that they can be optimized. A discussion of these optimization strategies follows.

Power in λ_f and λ_{2f}

The power concentrated at 1012 nm, from the fundamental (λ_{2f}) and SHG (λ_f), relates to the power in their beat (i.e. the f_{ceo} beat) through

$$P_{f_{ceo}} = k\sqrt{P_{\lambda_f} P_{\lambda_{2f}}} \tag{5.1}$$

where k is a proportionality constant taking into account losses in the detection process, detector responsivity, etc. This states that increases in either λ_f or λ_{2f} power leads to a square root power increase in the f_{ceo} beat.

Contributions to the noise level also need to be considered so that the signal-to-noise ratio can be optimized. Noise contributions come from the amplification, compression, and supercontinuum generation processes, as well as from shot noise. Shot noise is frequency-independent quantum-limited intensity noise. It appears as "white noise", and scales with total power levels as

$$S(f) \propto \sqrt{P_{tot}} \tag{5.2}$$

To determine whether we're shot noise limited, the optical power onto the photodiode was systematically reduced and the resulting RF signal noise level monitored. Doing this confirmed shot noise limited operation. In this limit, the following with regards to the optimization of λ_f and λ_{2f} power levels are considered for maximizing SNR. It turns out that increases to λ_f and/or λ_{2f} power can only help SNR. In the worst case, SNR remains unchanged with λ_f,λ_{2f} power increases. This comes from the fact that signal strength goes up with the square root of the product of λ_f and λ_{2f} powers, while shot noise only goes up with the square root of the sum of λ_f and λ_{2f} powers. Let's first consider the case when λ_f and λ_{2f} power levels are equal. Then, for example, a doubling in either λ_f or λ_{2f} power leads to a $\sqrt{2}$ increase in signal strength compared to a $\sqrt{1.5}$ increase in shot noise. When λ_f,λ_{2f} power levels differ[15], then power increases to one (the weaker signal) will have a greater effect on SNR compared to power increases to the other (the stronger signal). In the extreme case when power in one signal dominates power in the other signal, then power increases to the weaker signal is completely transferred to increasing SNR (since shot noise is only marginally increased), while power increases to the stronger signal results in no change to SNR (i.e. f_{ceo} and shot noise go up by the same amount).

Also, note that differences in optical power are squared during the optical-to-RF detection process[16]. This means that the conclusions from the SNR discussion above differ from what's actually measured on the RF spectrum analyzer by a factor of 2 (in log scale). So for the

[15] Typically, there's more power in λ_{2f}.

[16] The photodiode converts optical power to current, *I*. The RF spectrum analyzer plots $S(f) \propto I^2$.

example of equal λ_f and λ_{2f} powers, a doubling of either λ_f or λ_{2f} power would result in an RF SNR increase of $\frac{4}{3}$ (not the $\frac{\sqrt{2}}{\sqrt{1.5}}$ SNR increase stated earlier).

SHG PPLN

Generally, λ_f power limits f_{ceo} beat detection. To get to higher λ_f powers requires SHG be optimized. Since SHG is a periodic process, where power in the second harmonic is gained and lost, a periodically-poled lithium niobate nonlinear crystal is used to counteract this loss by periodically reversing the sign of the nonlinear coefficient at the point SHG begins to lose power (i.e. quasi-phasematching) [69]. For 2024nm → 1012nm SHG, a 29.5μm PPLN period is used, and the temperature of the PPLN is tuned to 160°C for optimal SHG. Focusing into the PPLN is accomplished with a 60mm focal-length plano-convex lens so that the depth-of-focus coincides with the 1 cm PPLN length.

Spectral Filtering of λ_f and λ_{2f}

Filtering is needed to eliminate everything that isn't part of the f_{ceo} beating process. Anything extra just adds to shot noise, but does nothing for the f_{ceo} beat. Since the λ_f signal has a 2.5nm bandwidth (SHG phasematching bandwidth), this means that everything but 1012nm ± 1.25nm should be bandpass filtered. Using wider bandpass filtering means shot noise is higher than it needs to be. Using shorter bandpass filtering removes a portion of λ_f and λ_{2f}, resulting in a less than optimal SNR. Only dielectric filters should be used. Filters with absorbing layers may operate over a broader range, but at the expense of over ~50% losses. Multiple dielectric filters will most likely need to be used in combination for proper filtering of octave-spanning spectra. Our f-2f interferometer uses three dielectric filters to filter out everything but λ_f and λ_{2f} – a short-pass dielectric filter with ~1100nm cutoff, a 10nm bandpass dielectric filter angle-tuned to 1012nm, and a 1.5nm bandpass dielectric filter angle-tuned to 1012nm. A custom coated 2.5nm bandpass dielectric filter could not be obtained in time for these experiments, costing us an estimated ~2dB in SNR.

Spatial and Angular Filtering of λ_f and λ_{2f}

Spatial and angular overlap of the λ_f and λ_{2f} beams on the detector surface is important as it ensures that all of λ_f and λ_{2f} is being used constructively to generate the f_{ceo} beat. Non-optimal spatial overlap leads to the non-overlapped regions not contributing to the f_{ceo} beat, but still contributing to shot noise. A mismatch in angular overlap leads to spatial beating of the λ_f and λ_{2f} beams, resulting in interference fringes on the detector surface. These fringes cause partial cancellation of the f_{ceo} beat, therefore contributing to the f_{ceo} beat in a negative way.

Thorough and precise alignment measures can be taken to maximize spatial and angular overlap. Coupling into singlemode fiber is the alignment approach taken here as it ensures complete spatial and angular overlap. There is some loss involved in coupling into fiber, but this loss is fairly small compared to the alternative of not being completely overlapped. The objective is to maximize λ_f coupling into fiber, even if it means sacrificing some λ_{2f}. This is achieved using a set of 25mm and 40mm lenses to mode-match the 1.5mm diameter λ_f beam to a collimator package for optimal coupling into Hi1060 fiber (which is singlemode at 1012nm). We were able to couple 70% of λ_f into the fiber. 70% of λ_{2f} was also coupled into the fiber, even though no additional measures were taken to mode-match the λ_{2f} beam. The fiber directs λ_f,λ_{2f} into a photodiode.

Photodiode Selection

Different photodiodes have different noise floors (spec'd as the detector dark current), so using a photodiode with a low noise floor may help SNR. Avalanche photodiodes are typically used for low power applications for this very reason. We tried a variety of photodiodes, including an InGaAs APD, to see if an increase in SNR would result. No discernable difference was noticed between the InGaAs APD and a fiber-coupled InGaAs photodiode with 10 GHz bandwidth (APD has bandwidth slightly greater than 1 GHz). This means that the shot noise in our signal is higher than the noise floor of both detectors.

RF Amplification

RF amplification of weak photodetected f_{ceo} beat signals is strongly recommended before being sent into the RF spectrum analyzer for analysis. More times than not, the spectrum analyzer will have a noise floor that's greater than the photodetected signal noise level. This

hurts SNR. RF amplification can also reduce SNR, so it's important to use amplifiers which provide linear amplification over all power levels.

Day-to-Day Optimization

Day-to-day (sometimes hour-to-hour) optimization may be needed to compensate for small changes in the laser. This typically involves tweaking the Raman fiber laser pump power level to adjust (slightly) supercontinuum generation. Changes to the laser state, however, will require the pre-chirp to be re-adjusted. If possible, adjustments to post-chirp fiber are avoided because the splices to both the gain fiber and HNLF have been optimized and are extremely troublesome to re-optimize (Caution: Even small splice losses can be detrimental at high powers) after each change to laser state.

5.1.3 f_{ceo} Beat Detection Results

λ_f,λ_{2f} powers of 28μW and 0.29mW, respectively, were obtained after the optimization steps above were applied to the continuum shown in Fig. 4-7. From our experience, this should be more than sufficient for detection of a strong f_{ceo} beat. An InGaAs APD detects the beat, followed by RF post-amplification to make sure the detected beat (including noise) is above the noise floor of the RF spectrum analyzer. The timing delay and waveplates (for temporal and polarization overlap) are re-tweaked to maximize SNR. This results in the f_{ceo} beat shown in Fig. 5-2. Depicted is the f_{ceo} beat along with one of its many copies (copies of the f_{ceo} beat exist to the left and right of each harmonic of the repetition rate).

For comparison, this beat is put side by side with the f_{ceo} beat generated out of a Menlo Systems commercial frequency comb system (see Fig. 5-3). The differences between the two are rather obvious. The Menlo Systems beat has a measured f_{ceo} linewidth of ~300 kHz, and appears just as narrow as the repetition rate line in the plotting range shown. On the other hand, the linewidth of the GHz beat can't even be measured because it jitters around too much. Even without measurement, the broadness of the beat is apparent.

The main sources for f_{ceo} noise come from the laser, as suggested by Newbury and others [70]. The laser was therefore adjusted to investigate the effect different modelocked states had

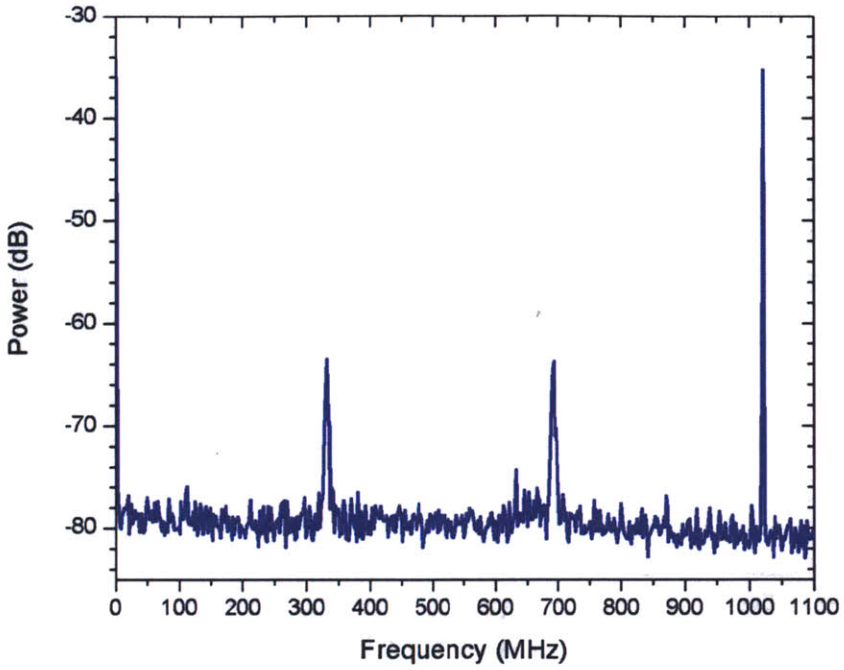

Figure 5-2: f_{ceo} beat detection. A 20dB SNR f_{ceo} beat is detected with λ_{FUND},λ_{SHG} powers of 0.29mW and 28μW, respectively. The low SNR relative to the 44dB SNR rep rate line means that the f_{ceo} beating process isn't completely phase-coherent and/or constructive. In addition, the broadness of the fceo beat corresponds to a noisy laser state.

on f_{ceo} noise. f_{ceo} noise directly stems from noise in the optical lines, which has been modeled [71] as

$$S(f) = \left(\frac{1}{8\pi^2} \theta h\nu \frac{l_{tot} f_{rep}}{E_p} \right) \frac{1}{f^2} \tag{5.3}$$

where θ, $h\nu$, E_p, l_{tot}, f_{rep} represent, respectively, the spontaneous emission factor, photon energy, intracavity pulse energy, intracavity roundtrip losses, and repetition rate. This PSD, derived from the classic Schawlow-Townes linewidth adapted for modelocked lasers, refers to the noise of the mean carrier frequency (i.e. the optical lines at the center of the optical spectrum). f_{ceo} noise is related to this by a factor $(\omega_c \tau_p)^2$ [72] such that

$$S(f) = (\omega_c \tau_p)^2 \left(\frac{1}{8\pi^2} \theta h\nu \frac{l_{tot} f_{rep}}{E_p} \right) \frac{1}{f^2} \tag{5.4}$$

This increase is attributed to increased noise for optical lines away from the center of the optical spectrum.

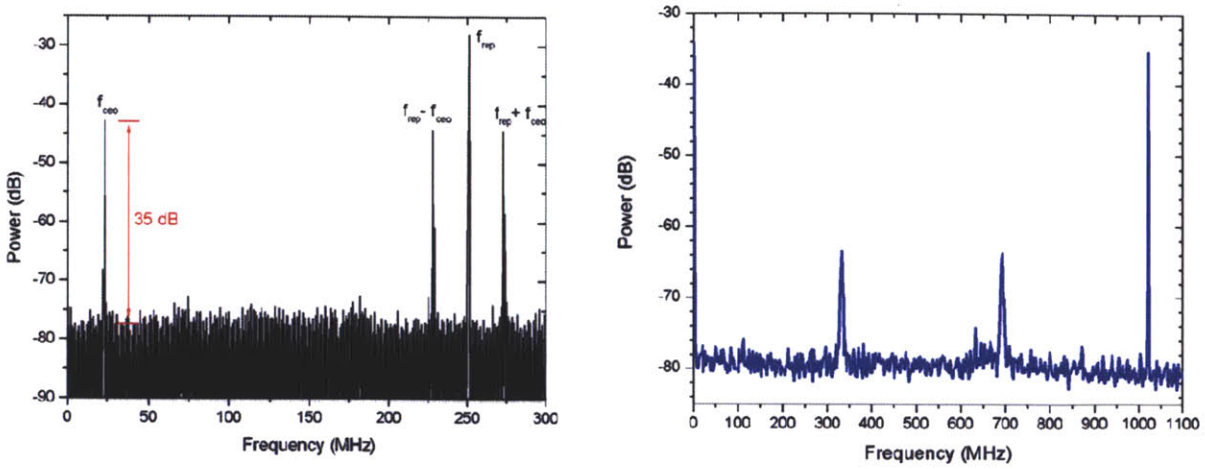

Figure 5-3: f_{ceo} beat comparison. Compared to the f_{ceo} beats generated out of a commercial Menlo Systems 250MHz frequency comb (a good representation of f_{ceo} beats from typical fiber lasers), those generated out of the GHz all-fiber laser appear much broader and more noisy.

The model reveals the importance of pulse energy and duration on f_{ceo} noise (along with intracavity roundtrip losses). This led us to try different modelocked laser states for f_{ceo} beat detection, specifically the ultra-broad, high-energy state described in Fig. 2-11. As it turned out, that state wasn't any better in terms of noisy f_{ceo} beats, so we moved on to other states.

The 1560nm-centered 7nm-bandwidth state depicted in Fig. 2-12 worked out best, generating the f_{ceo} beats shown in Fig. 5-4. The beats look strong (35dB SNR) and its linewidth appears as narrow as the repetition rate line in the plotting range shown. A zoom-in on the f_{ceo} beat, Fig. 5-5, gives a clearer indication of its linewidth. The beat still jitters around faster than the 50ms (20 Hz) sweep time of the spectrum analyzer, making it difficult to accurately measure its linewidth directly. Instead, a linewidth estimate is obtained by extrapolating the effect of the spectrum analyzer's resolution bandwidth setting on f_{ceo} SNR. A table summarizing these measurement results is shown in Fig. 5-5. For RBWs less than f_{ceo} linewidth, SNR should remain unchanged. Conversely, RBWs greater than f_{ceo} linewidth will lead to decreases in SNR, depending on the ratio of f_{ceo} beat to noise captured in the measurement slot. The data allows for the extrapolation of a 60kHz f_{ceo} beat linewidth.

Furthermore, a quantitative analysis can be performed to measure the quality of the f_{ceo} beating process. Optimized λ_f,λ_{2f} powers of 14μW and 56μW were used to generate the 33dB

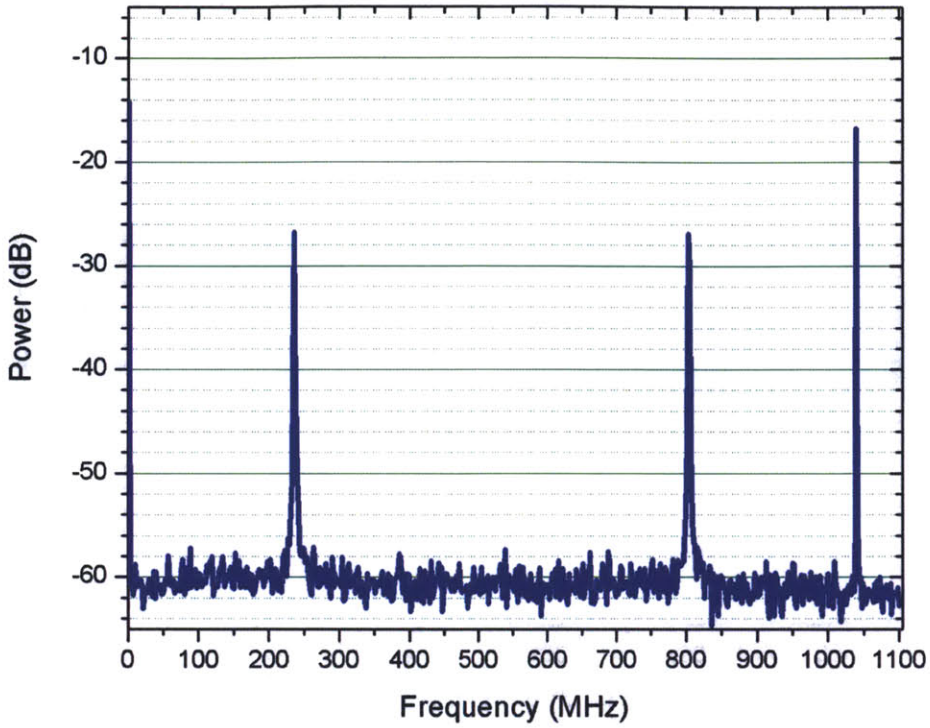

Figure 5-4: Improved f_{ceo} beat detection. A 33dB SNR f_{ceo} beat is detected with λ_{FUND},λ_{SHG} powers of 56μW and 14μW, respectively. The ~10dB difference in f_{ceo} and f_{rep} signifies almost complete phase-coherent and constructive beating of λ_{FUND} and λ_{SHG} to generate f_{ceo} (perfect f_{ceo} beating results in a f_{ceo},f_{rep} difference of 8dB).

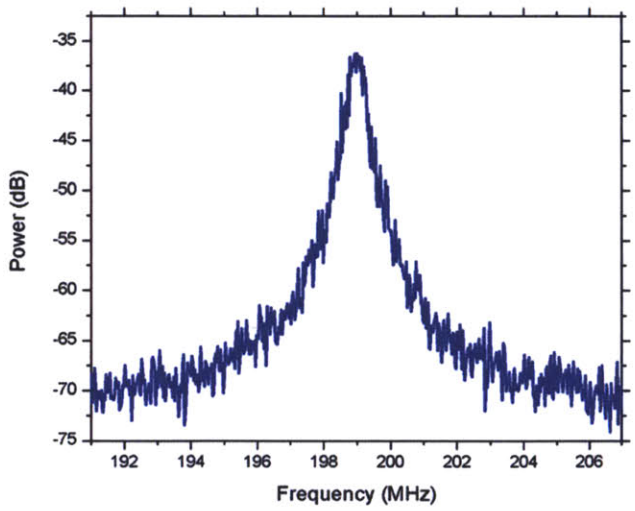

RBW Setting	f_{ceo} Beat SNR
10 kHz	37 dB
30 kHz	37 dB
100 kHz	33 dB
300 kHz	28 dB
1 MHz	23 dB

Figure 5-5: f_{ceo} beat linewidth measurement. Values for f_{ceo} beat SNR at different RF spectrum analyzer RBW settings are used to estimate an f_{ceo} beat linewidth of 60kHz.

SNR f_{ceo} beat. The total power onto the photodetector, 70μW, should be reflected in the strength of the repetition rate line depicted in Fig. 5-4. Since the f_{ceo} beat goes with the square root of the product of λ_f,λ_{2f} powers (Eq. (5.1)), it's calculated to contain 28μW. This is 2.5 times weaker than the total power contained in λ_f,λ_{2f}, meaning that the f_{ceo} beat should be ~8dB lower than the repetition rate line (after accounting for the extra factor of 2 from the optical-to-RF detection process, see Sec. 5.1.2). This analysis assumes perfect beating – to be specific, it assumes complete phase coherence (as well as flat phase) across λ_f and λ_{2f} so that all of the power incident on the photodetector beat constructively to generate the f_{ceo} beatnote. Our 33dB SNR f_{ceo} beat, depicted in Fig. 5-4, is determined to be ~10 dB below the repetition rate line – this agrees well with our analysis, indicating that λ_f and λ_{2f} are phase-coherent[17].

It's still not completely clear why this particular modelocked state (Fig. 2-12) worked better than the others, especially the one with shorter, more energetic pulses (Fig. 2-11). It may have something to do with the pump RIN, and how it's coupled into the laser state. This specific state is less responsive to manual changes of pump power compared to the "noisier" states, which may mean that it's also less susceptible to pump RIN.

5.2 Self-referenced f_{ceo} Beat Stabilization

Detection of a 33dB SNR f_{ceo} beat signal (in a 100kHz RBW) is more than sufficient for stabilization. Two approaches were pursued for correcting fluctuations in f_{ceo}. The pump power modulation technique for controlling f_{ceo} was tried first. A lock resulted, but stability issues caused an external cavity approach using an acousto-optic frequency shifter to be implemented for more stable locking. Both approaches are discussed, their limitations outlined, and results presented.

5.2.1 Pump Power Modulation

The conventional approach for compensating f_{ceo} fluctuations is through feedback to the pump source. Modulating the pump power into the laser cavity adjusts intracavity pulse

[17] If the wings of the octave-spanning supercontinuum are phase-coherent, it can be assumed that the phase coherence stretches across the entire supercontinuum.

energies[18], and this has an effect on f_{ceo} through nonlinear phase shifts [74]. Various schemes can be employed to modulate pump power, the two most common being an AOM for solid-state lasers and control of the current driving the pump diode for fiber lasers. The latter scheme is used in our case because of our all-fiber configuration.

5.2.1.1 Stabilization Setup

The stabilization setup is shown in Fig. 5-6. The f_{ceo} beat detected out of the APD is first low-pass filtered (1 GHz cutoff) and amplified. It's then mixed down with a signal generator (HP 83732B) to 10.7 MHz before it subsequently goes through an additional stage of amplification and a series of lowpass and bandpass filters. The resulting down-mixed, amplified, and filtered f_{ceo} beat is sent for phase detection with a reference RF oscillator (SRS DS345). The phase detection is accomplished with a digital phase detector with a $\pm 32\pi$ tracking range. This extended tracking range is typically needed for f_{ceo} locks, since f_{ceo} beats are considered relatively noisy. The phase detector output serves as the error signal, which is sent into a servo lockbox consisting of a loop filter with proportional-integral gain to generate the control signal.

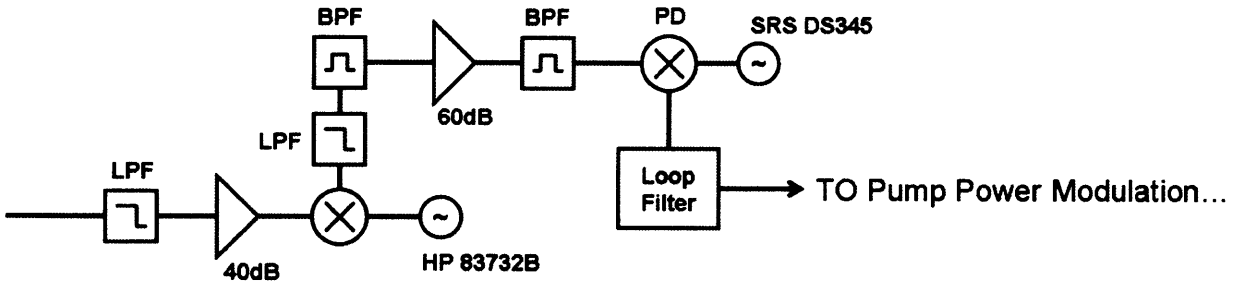

Figure 5-6: Locking electronics setup for stabilization of f_{ceo} to a RF reference oscillator (SRS DS345). The f_{ceo} beat is first lowpass filtered and amplified before being mixed down to 10.7MHz. The result is then lowpass and bandpass filtered, amplified, and again bandpass filtered before phase detection with the RF reference oscillator. The error signal is loop filtered with proportional integral gain, and sent to a modulation circuit to control pump power.

The control signal drives a current modulation circuit, its schematic illustrated in Fig. 5-7. The circuit is placed parallel to the pump diode anode-cathode leads, and consists of a BJT and

[18] Other gain/loss mechanisms exist, such as tilting of an end mirror to modulate the losses in the cavity [73].

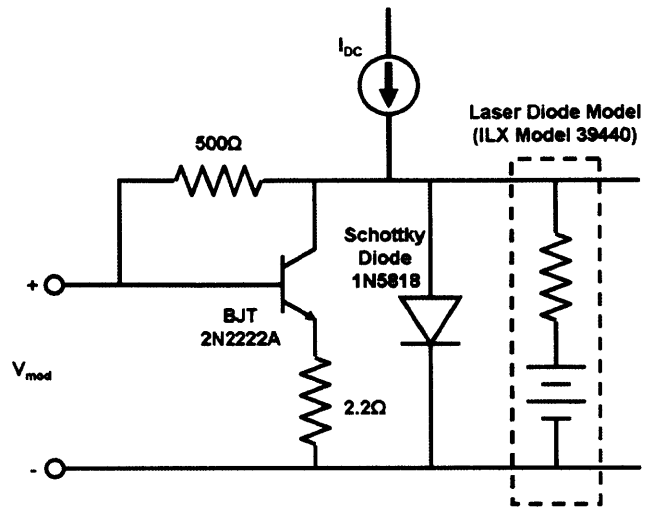

Figure 5-7: Pump power modulation circuit. A BJT is placed in parallel with the laser diode to extract a portion of the current driving it (up to 15mA). The Schottky diode is added to protect against accidental reverse-biasing of the laser diode.

Schottky diode. The control signal from the servo lockbox drives the base port of the BJT to extract current away from the pump diode. The Schottky diode is implemented for protection against reverse biasing. At the 1000mA pump current needed for sustained modelocking, a 1 V input to the current modulation circuit extracted ~2mA of current. In total, ~15mA of current could be modulated.

5.2.1.2 Stabilization Results

f_{ceo} stabilization using pump power modulation was extremely difficult, as changes to f_{ceo} using this technique were barely enough to compensate for its fluctuations[19]. This was to be expected, as we're operating with much shorter cavities (and longer pulses), reducing the amount of nonlinear phase shift every roundtrip. In the "good laser state", the f_{ceo} beat jittered ~1-2 MHz, but the beat could only be moved ~3 MHz with the pump power modulation levels available. In fact, it was tricky trying to separate f_{ceo} movements due to pump changes from those due to random noise fluctuations. In the "noisy laser state", the f_{ceo} beat jittered ~5 MHz.

[19] Tests were also conducted to identify the different sources responsible for fluctuations to f_{ceo}. These tests were performed by measuring f_{ceo} fluctuations at different stages of isolation from environmental disturbances. The results were as follows: ~50-100 MHz f_{ceo} fluctuations w/ no protection, ~10 MHz w/ enclosure (air currents), ~3 MHz w/ enclosure and lead-foam stack (air currents, mechanical vibrations), ~1-2 MHz w/ inch-thick foam enclosure and lead-foam stack (air currents, mechanical vibrations, acoustic vibrations).

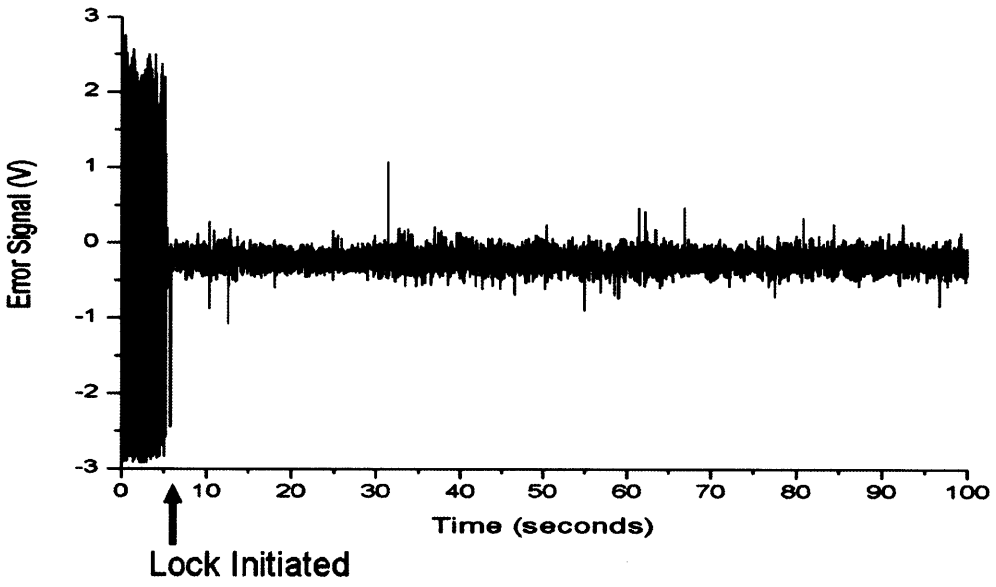

Figure 5-8: f_{ceo} lock with pump power modulation. In-loop error signal out of the digital phase detector, plotted over 100 seconds. The error signal collapses to ~100mV RMS when the lock is initiated.

The beat was more responsive to pump modulations in this state, but not responsive enough to correct for the increased fluctuations. Nevertheless, locking was achieved in the "good laser state" (lock-settings: Gain = 6.76, Corner Frequency = 3 kHz). Despite the lock being difficult to maintain, the following oscilloscope trace measuring the in-loop error signal was taken, Fig. 5-8. It demonstrates an f_{ceo} lock lasting over a minute. A PSD measuring residual phase noise could not be taken before the lock was lost. This was not very easily reproducible.

5.2.2 Acousto-optic Frequency Shifter

The problems encountered with the pump power modulation scheme can be largely overcome with the use of an acousto-optic frequency shifter [75]. The AOFS scheme is external to the laser cavity, meaning that modelocking is not disturbed. It also decouples changes to f_{ceo} from f_{rep}[20], making it easier for both locks to co-exist.

The principle of acousto-optic frequency shifting is diagrammed in Fig. 5-9. AOFSs provide frequency shifts through the Doppler Effect. Either a forward shift or a retarded shift is

[20] Pump power modulations affected f_{rep} through thermal effects related to pump absorption.

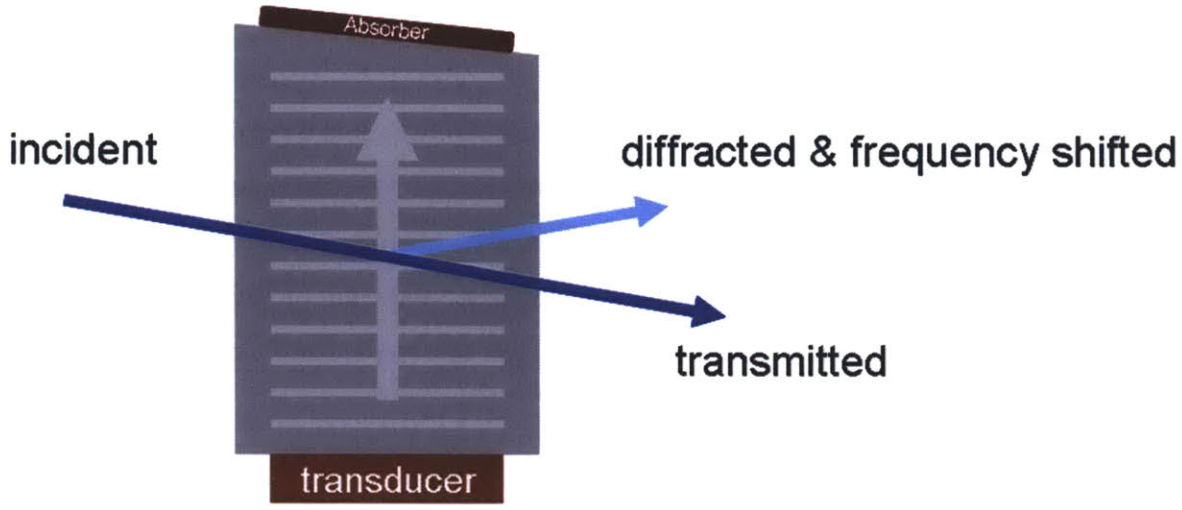

Figure 5-9: Acousto-optic Frequency Shifter for f_{ceo} control. A piezo-electric transducer at one end of an acousto-optic crystal (i.e. TeO_2) produces propagating sound waves that periodically alter the crystal's refractive index to form a moving diffraction grating. The incident laser beam is both diffracted (due to the grating) and frequency shifted (due to the Doppler Effect). An absorber is attached to the angled back facet to help reduce unwanted back-reflected sound waves.

produced when the input beam propagates at the Bragg angle relative to the propagating sound wave. A piezo-electric transducer at one end of the acoustic medium generates the propagating sound wave. The pressure of the oscillating sound wave modifies the refractive index of the material. The intensity of that sound wave, along with the medium in which the sound wave propagates, determines how much of the input beam is shifted. Ideally, these sound waves would propagate in an infinite length of crystal to eliminate any chance of back reflections. Practical designs minimize back-reflections using three techniques. The first involves using longer crystals to take advantage of material absorption. The second and third techniques both involve reducing reflections at the back-end of the crystal (i.e. the end opposite the transducer). The end facet is angled (to redirect reflected sound waves in a different propagation direction) and equipped with an acoustic absorber (to absorb as much of the sound wave so that less is reflected).

Other concerns (and resolutions) with AOFSs for f_{ceo} control:

Locking Modulation Bandwidth

The AOFS used in these experiments is made from TeO_2, which is typically used at 1.5μm applications because of its high elasto-optic coefficient. Sound waves propagate at 4260 m/s in TeO_2, which is the main limitation to locking modulation bandwidth. A 1.4mm diameter beam propagating adjacent to the transducer could have a locking bandwidth of 380kHz. To increase this bandwidth, focusing into the AOFS is needed. To get to a target bandwidth of 5MHz requires a focused beam diameter of ~100μm.

Angular Deviations

Doppler frequency shifts are accompanied by changes to the propagation angle of the output beam. These angular deviations will lead to huge coupling losses when going back into fiber. A double-pass technique can be used to completely eliminate these angular deviations [76]. Doing this, however, can lead to worsening of other concerns (see amplitude modulation). Instead, focusing into the AOFS using a set of lenses effectively transfers angular deviations to spatial deviations (in our setup, spatial deviations are much more tolerable compared to angular deviations). Focusing allowed only 20% coupling losses over the 10 MHz operating range.

Amplitude Modulation

Our concerns with amplitude modulation are well documented in the section on vector solitons (Sec 2.1.2.3). There it was shown the effect amplitude modulations have on subsequent amplification and nonlinear spectral generation processes. Two sources of amplitude modulation exist with the use of AOFSs. One source comes from the back-reflections described earlier. Back-reflections provide frequency up-shifts (down-shifts) which spatially overlap the frequency down-shifted (up-shifted) beams resulting from the forward propagating sound wave. The up-shifted and down-shifted frequencies result in an amplitude modulation at twice the drive frequency. This form of amplitude modulation is specific to the AOFS used – reductions to amplitude modulation require improved AOFS designs (outlined above). The second source of amplitude modulation comes from the beating of frequency shifted and frequency un-shifted signals resulting in an amplitude modulation at the drive frequency. There should theoretically

be no spatial overlap of the frequency un-shifted and frequency up-shifted (frequency down-shifted) beams. However, this cannot be avoided in practice, particularly when focusing into the AOFS. We found that defocusing into the AOFS, i.e. making sure that the focal point of the beam is not in the path of the propagating sound wave, minimizes amplitude modulations at the drive frequency.

5.2.2.1 Stabilization Setup

Our setup places the AOFS between the laser and pre-amplifier. Two collimators are used to couple out and back into fiber, with the use of 60mm lenses (stipulated earlier for ~5MHz locking bandwidths) to focus into the AOFS. The AOFS is driven by a control signal from the feedback loop, the setup shown in Fig. 5-10. It resembles the pump power modulation setup diagrammed in Fig. 5-6, with the differences coming after the control signal is generated from the servo lockbox. In this setup, the control signal is used to drive a linear voltage-controlled-oscillator between 129MHz and 139MHz. Because the AOFS is designed for operation at 50-

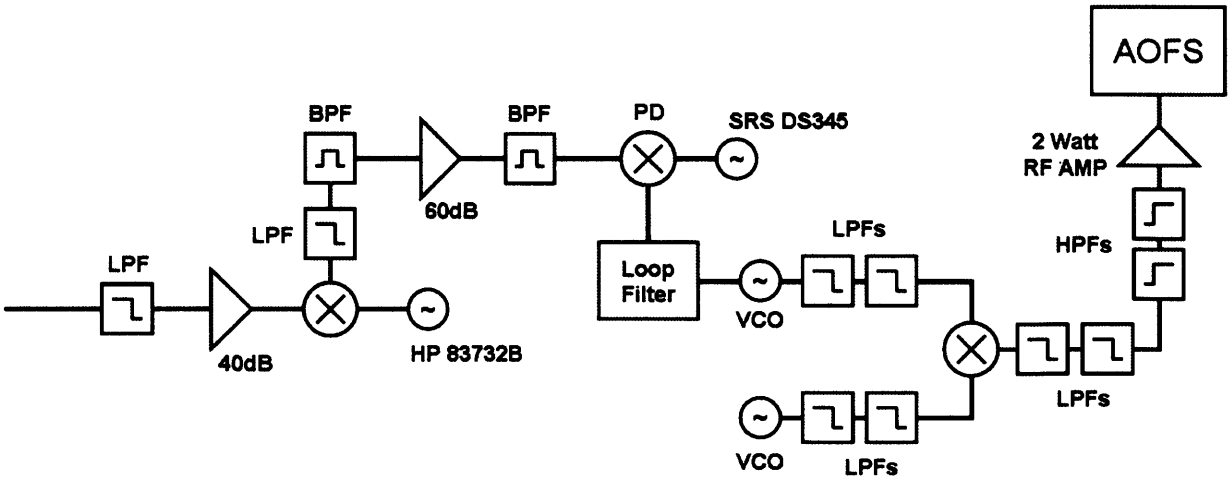

Figure 5-10: Locking electronics setup for stabilization of f_{ceo} to a RF reference oscillator (SRS DS345) using feedback to an AOFS. The front-end of the setup is similar to that used for the pump power modulation locking scheme, Fig. 5-6. That is, the f_{ceo} beat is lowpass filtered, amplified, and mixed down to 10.7MHz. The down-mixed signal is then filtered and amplified before phase detection with the RF reference oscillator. The error signal goes into a loop filter with proportional integral gain and the resulting control signal drives a VCO, which is mixed with another VCO set to a fixed frequency to generate the 50-60MHz feedback signal to the AOFS (amplification to 2W is needed for maximum diffraction efficiency).

60MHz, the VCO is mixed down to 50-60MHz with another VCO set to 189MHz. A series of RF filters suppresses everything but the 50-60MHz control signal. This signal is then amplified to 2 Watts using a high-power RF amplifier, and then sent to drive the AOFS.

5.2.2.2 Stabilization Results

The AOFS setup provides 10MHz of dynamic range, making stabilization of the "good laser state", which only has f_{ceo} fluctuations of ~1-2MHz, relatively straightforward (lock-settings: Gain = 4.6, Corner Frequency = 10kHz). A PSD of the residual phase noise was measured (from the in-loop error signal), and is shown in Fig. 5-11. The figure also shows a plot of the integrated phase noise, integrated up from 10MHz. The integrated phase noise from [10Hz,10MHz] is 3.97 rad. A comparison of our phase noise with that of a stabilized Menlo Systems 250MHz frequency comb shows similar integrated phase noise (Fig. 5-12). It's difficult

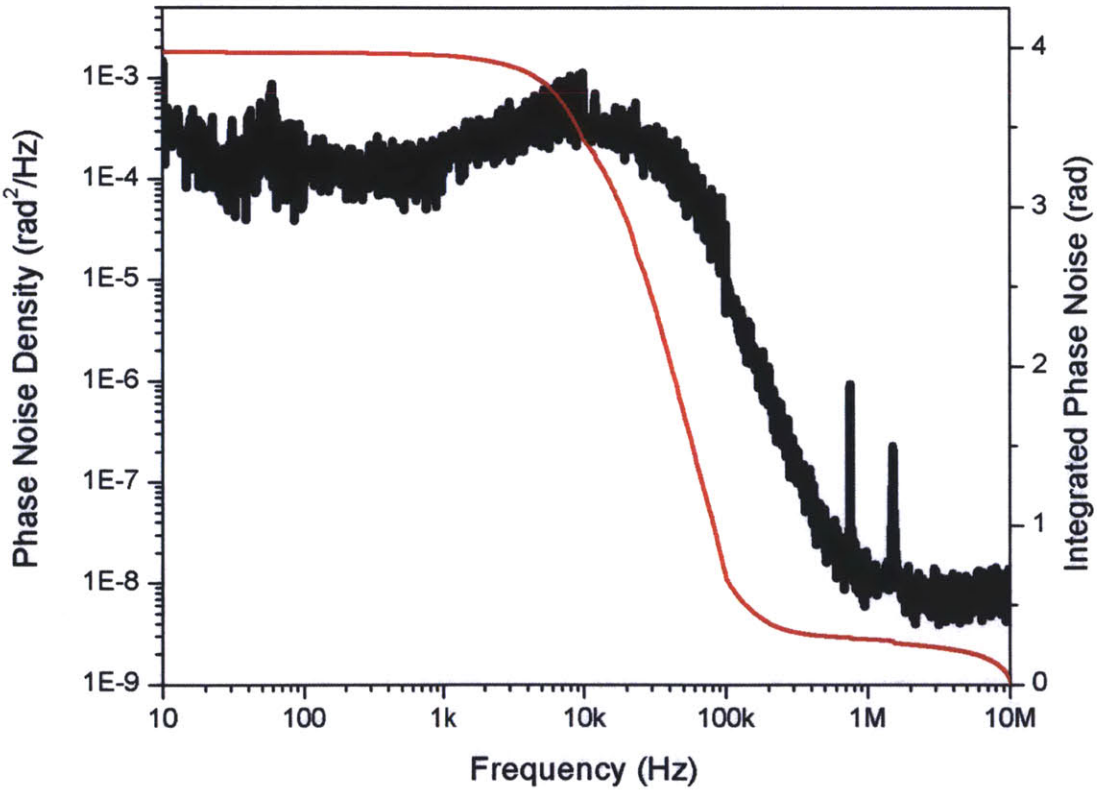

Figure 5-11: f_{ceo} lock performance with acousto-optic frequency shifting. Residual phase noise measurement of the in-loop error signal from [10Hz,10MHz], demonstrating a locking bandwidth of 25kHz and an integrated phase noise of 3.97 rad.

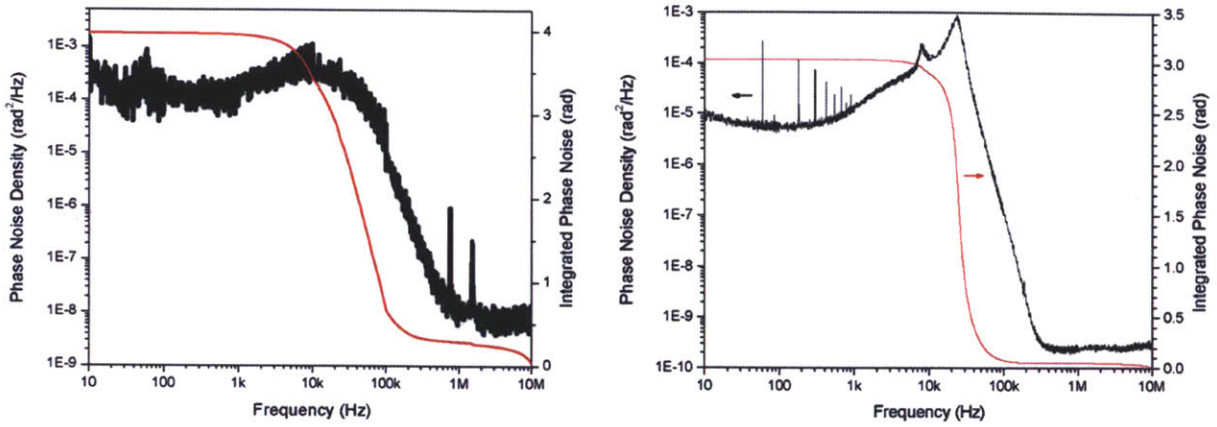

Figure 5-12: Comparison of f_{ceo} lock performance. The residual phase noise measurements of the f_{ceo}-locked GHz all-fiber laser (using acousto-optic frequency shifting) are compared to those obtained out of a commercial Menlo Systems 250MHz frequency comb (using pump power modulation). The locks are comparable in terms of their locking bandwidths, as well as their integrated phase noise.

to get the integrated phase noise below 1 rad with fiber lasers because f_{ceo} is extremely noisy outside its locking range. Increases in locking bandwidth would certainly help suppress this noise. In Er-doped fiber lasers, locking bandwidths by gain modulation are limited to 1-10kHz because of Erbium's long upper-state lifetime (~1 ms). Phase-lead circuits can be used to extend this bandwidth out to ~100kHz. It's these locking bandwidths which have been used to generate the ~1 rad integrated phase noise locks reported with fiber lasers [77].

5.3 Optically-stable Frequency Combs

Frequency comb stability is in general limited by the stability of the repetition rate lock. This is the case even though f_{rep} locks have demonstrated three to four orders less integrated residual phase noise compared to f_{ceo} locks. The reason for this is that the residual noise in the f_{rep} lock is multiplied up to the optical domain by a factor determined by the ratio of its center frequency to repetition rate (i.e. f_c/f_{rep})[21]. For a 1 GHz repetition rate, this factor is ~2×10^5. To overcome this limitation, f_{rep} is locked to an optical reference.

[21] Recall that cavity length fluctuations on the order of an optical wavelength (1.5μm) results in minimal change to the repetition rate, but in the optical domain, these fluctuations are magnified leading to shifting of the optical comb lines over an entire repetition rate.

5.3.1 DFG Lock to 3.39μm Optical Reference

A commercially available, compact and transportable, methane-stabilized HeNe laser[22] provides a 3.39μm optical reference which we use to "optically" lock f_{rep}. This process involves performing difference frequency generation to 3.39μm, which requires a spectrally broadened continuum spanning roughly 70% of an octave[23]. The DFG process effectively decouples f_{rep} from f_{ceo} (just as the f-2f self-referencing process decoupled f_{ceo} from f_{rep} – this is important as stabilization of f_{ceo}/f_{rep} should not rely on or affect the other) as follows:

$$f_{DFG} = (nf_{rep} + f_{ceo}) - (mf_{rep} + f_{ceo}) = (n-m)f_{rep} \tag{5.5}$$

where n and m are integers. The resulting 3.39μm DFG signal is just a multiple of f_{rep}, the 88,496th harmonic to be exact (assuming a 1 GHz repetition rate). Locking the DFG to the HeNe reference laser therefore locks f_{rep} to

$$\frac{1}{n-m}\left(\frac{c}{3.39\mu m}\right) \tag{5.6}$$

and it does so with 88,496 times more precision and stability compared to direct RF locking techniques.

5.3.1.1 DFG Setup

The DFG process is carried out experimentally with the setup shown in Fig. 5-13. A spectrum broad enough to generate a difference frequency (DFG) of 3.39 μm is produced out of a commercial Menlo Systems 250MHz frequency comb system, Fig. 5-14. A Mach-Zehnder interferometer, similar to the f-2f interferometer setup depicted in Fig. 5-1, is used for DFG. The continuum is first passed through a dichroic to separate the two wavelengths used for 3.39μm DFG, λ_l=1095nm and λ_h=1617nm. λ_l and λ_h traverse separate arms of the interferometer so that their temporal, spatial, angular, and polarization overlap can be optimized. A second dichroic recombines λ_l and λ_h, and a 40mm focal-length plano-convex lens used to focus into a PPLN phasematched for DFG at λ_l,λ_h. The optimal PPLN period is 29.5μm at an oven temperature of

---

[22] The 3.39μm HeNe frequency is stabilized to Methane's $F_2^{(2)}(P(7),\upsilon_3)$ optical transition [78].

[23] An optical spectrum centered at 1550nm and spanning 1260 – 2010nm corresponds to ~70% of an octave.

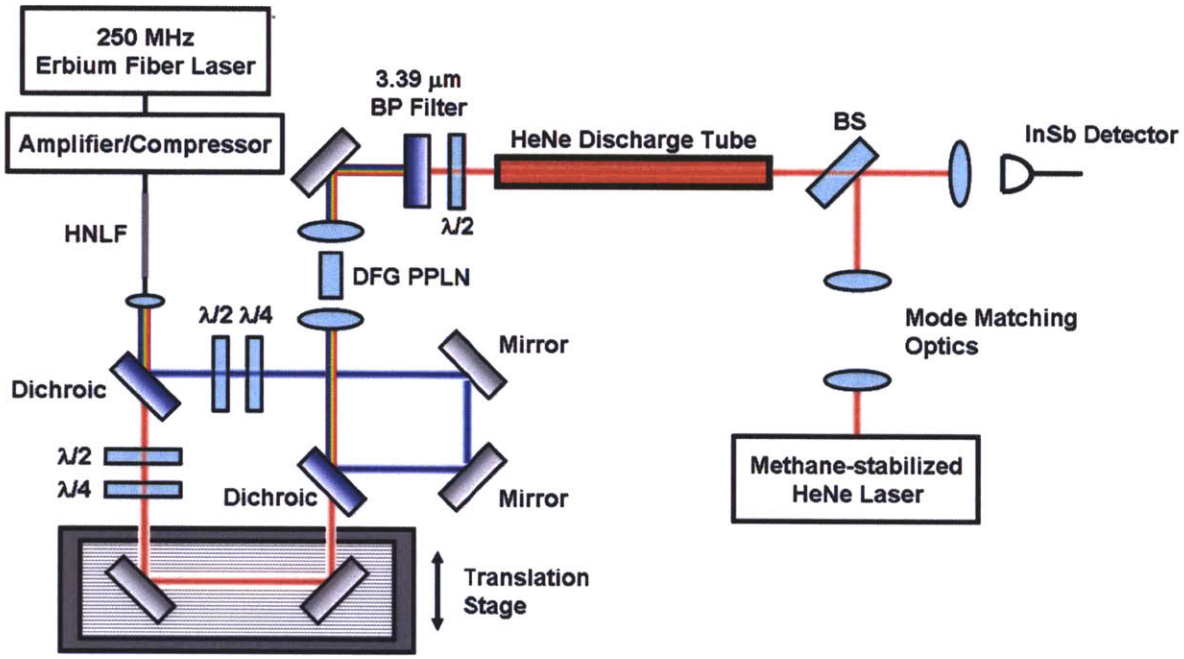

Figure 5-13: The DFG interferometer. A dichroic mirror separates the two wavelengths responsible for generating the 3.39μm DFG signal (1095nm and 1617nm), so that their temporal, spatial, angular, and polarization overlap can be optimized for DFG. Another dichroic mirror recombines the two wavelengths to perform DFG in a 29.5μm-period PPLN. The generated DFG signal is then bandpass filtered, amplified with a HeNe discharge tube, and combined with the 3.39μm HeNe reference signal. The DFG-HeNe beat is detected on a InSb photodetector.

160.2°C, which coincidently are the same phasematching conditions for the f-2f SHG process. A 40nm bandpass filter at 3.39μm filters out everything but the DFG signal before being detected in a liquid-nitrogen-cooled InSb detector. The detected DFG power is measured by connecting the detector output to a transimpedance amplifier set to a gain of 1 μA/V, and then monitoring the output of the transimpedance amplifier on an oscilloscope. Coupling into the detector using a 20mm focal-length plano-convex lens is then optimized, resulting in a 2.88V signal on the oscilloscope. This voltage is converted to a detected power of 1.1μW using the following values for the detector responsivity (2.56 A/W at 3.39μm) and transimpedance gain (1 μA/V). Assuming the 40nm bandpassed DFG contains ~4200 modes spaced by 250MHz, means ~260pW per mode.

The HeNe reference laser is mode-matched to the DFG beam using a 200mm/75mm telescope, and coupled into the DFG path through a beamsplitter. The HeNe power on the detector is measured to be 4.3μW (measured in the same manner as that described for DFG:

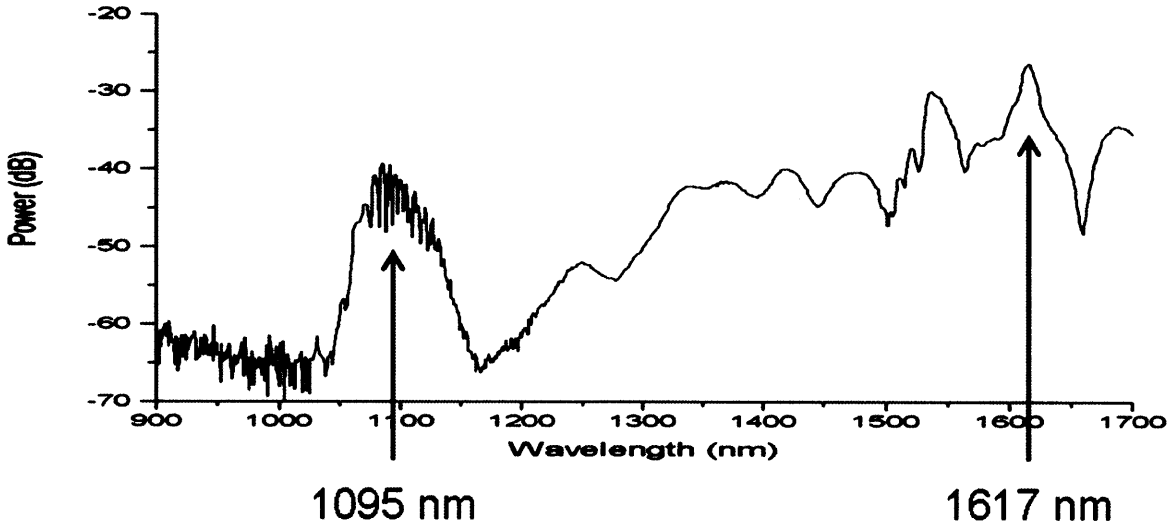

Figure 5-14: The DFG continuum. The continuum generated with the amplified/compressed Menlo Systems 250MHz frequency comb, optimized for performing DFG with the two wavelengths indicated (1095nm and 1617nm).

2.18V transimpedance amplifier output with gain set to 5 μA/V). Note that this power is all in a single longitudinal mode – this means the HeNe line dominates the DFG line (4.3μW vs. 260pW). In such cases, as discussed earlier, increases to the much weaker DFG line are completely transferred to SNR increases (i.e. since negligible change to shot noise level). For that reason, a HeNe discharge tube is placed in the DFG path to amplify the power in one DFG mode by 10dB, i.e. the mode closest to the 3.39μm HeNe laser line. Since only one mode is amplified, total DFG power isn't noticeably increased (2.6nW), but the SNR of the DFG-HeNe beat should see a 10dB increase.

5.3.1.2 DFG-HeNe Beat Detection and Stabilization

A DFG-HeNe beat is detected with 25dB SNR (note that prior to insertion of the HeNe discharge tube, the SNR was only 15dB, as expected), Fig. 5-15. The beat is tuned to 10MHz through adjustment to the laser repetition rate, and then locked to an RF reference oscillator (SRS DS345) using the feedback loop setup shown in Fig. 5-16. The digital phase detector measures the phase difference between the RF beat and reference signals, and outputs an error signal which is subsequently loop-filtered and P-I amplified (lock-settings: Gain = 2.08, Corner

Frequency = 1kHz), and sent to a custom home-built high-voltage piezo driver circuit which modulates a piezo-mounted end mirror in the laser cavity.

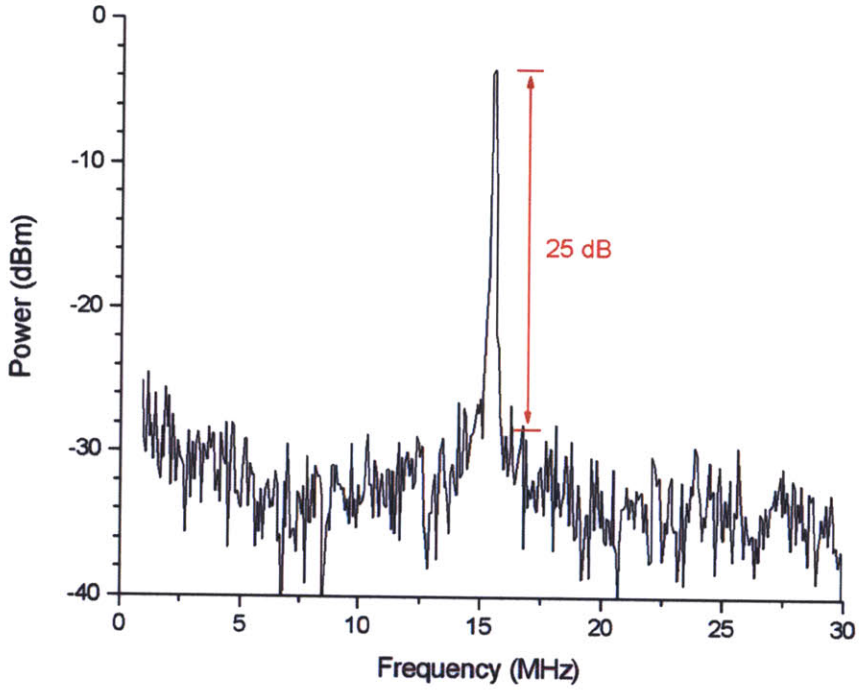

Figure 5-15: The DFG-HeNe beat. A 25dB SNR DFG-HeNe beat is measured (100kHz RBW).

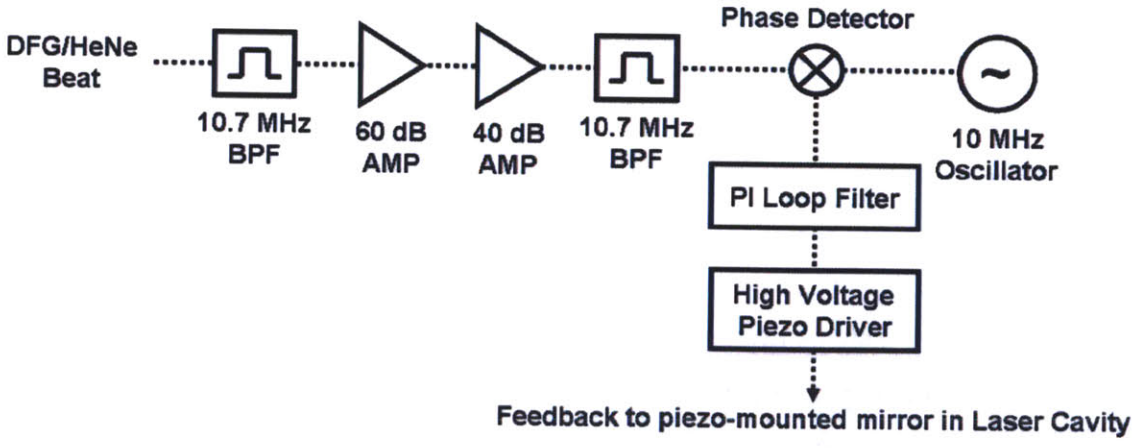

Figure 5-16: Feedback loop setup for DFG-HeNe lock. The DFG-HeNe beat is bandpass-filtered and amplified, then compared to a 10MHz RF reference oscillator using a digital phase detector. The error signal out of the digital phase detector is loop filtered with proportional integral gain, then sent into a custom high-voltage piezo driver to control the piezo-mounted end mirror in the laser cavity.

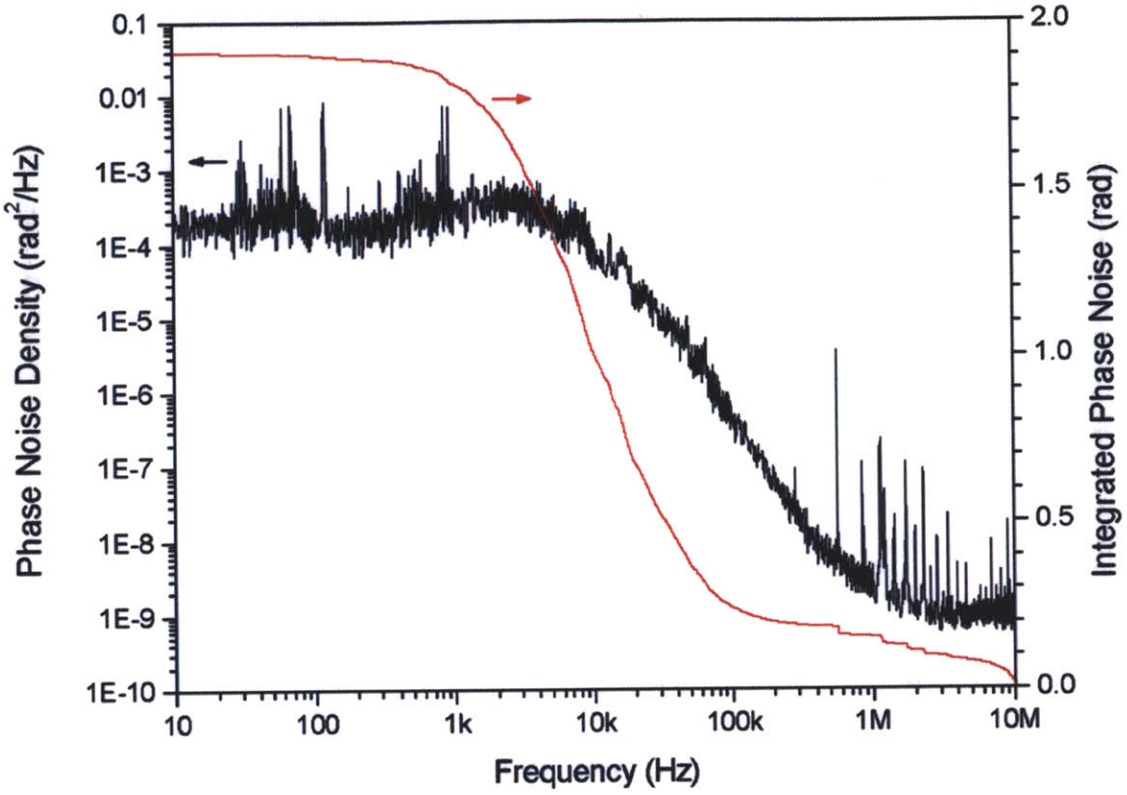

Figure 5-17: DFG-HeNe lock performance. In-loop phase noise spectrum of the frep-locked system, demonstrating a locking bandwidth of 8kHz and an integrated phase noise of 1.9 rad.

5.3.1.3 Phase Noise/Frequency Stability Analysis of DFG f_{rep} Lock

An in-loop phase noise measurement was taken to analyze the lock, Fig. 5-17. Notice that the low frequency phase noise is only suppressed up to ~8 kHz, which is the locking bandwidth of our feedback loop. Beyond this, the phase noise follows that of the free-running oscillator. The bandwidth limitation stems from a non-optimal piezo-mounted end mirror assembly. We can expect to obtain locking bandwidths of >60 kHz with optimized assemblies, resulting in improved phase noise performance. As is, the integrated phase noise is ~1.9 rad, integrated from [10Hz,10MHz]. This is still one to two orders of magnitude more stable than the best RF f_{rep} locks.

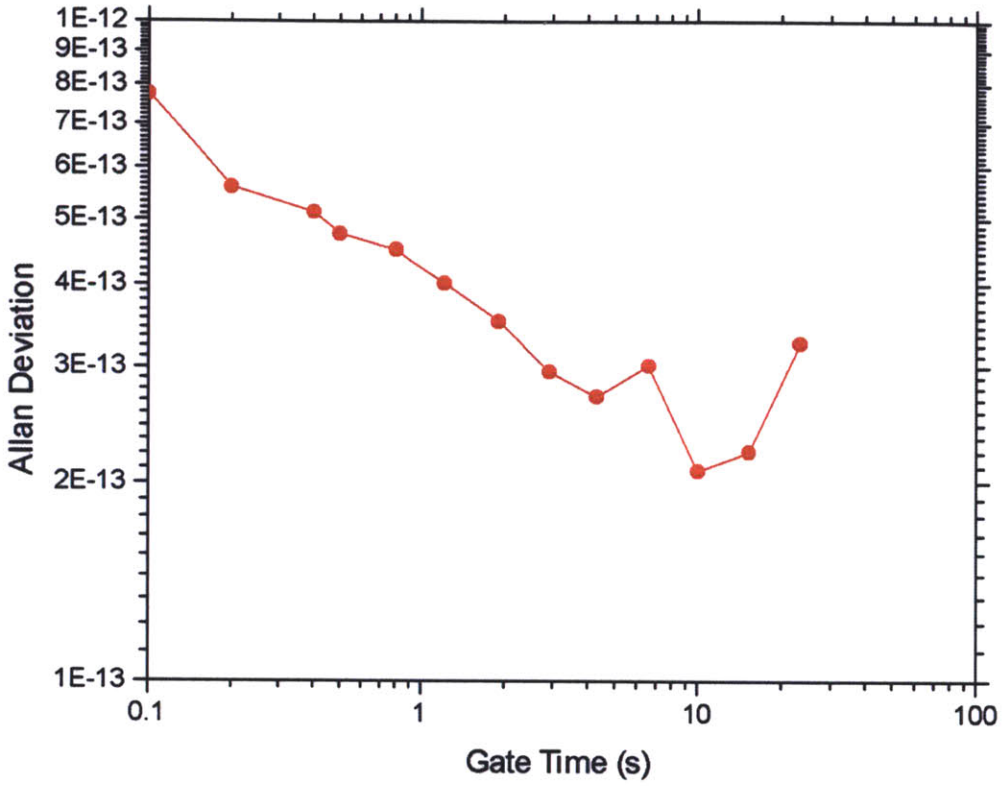

Figure 5-18: Long-term frequency stability of DFG-HeNe lock. The Allan deviation of the DFG-HeNe beat is measured for several gate times providing a measure of f_{rep} long-term stability with respect to the methane-stabilized HeNe reference.

Long term frequency stability measurements were also taken using the stabilized 10MHz DFG-HeNe beat. The Allan deviation plot shown in Fig. 5-18 provides a measure of DFG stability relative to the HeNe reference laser. For a 1 s gate time, stability of ~$4x10^{-13}$ is achieved. A comparison with a similarly locked Ti:Sa system was also performed using the setup depicted in Fig. 5-19. The 10 GHz repetition rate harmonic for each laser (10^{th} harmonic for Ti:Sa, 40^{th} harmonic for ErFL) was detected, bandpass filtered, amplified, and then used to mix down to a few Hz. The measured stability is plotted in Fig. 5-20. Allan deviation traces for the ErFL and Ti:Sa DFG-HeNe beats are included for reference. The comparison is limited by the ErFL DFG-HeNe lock.

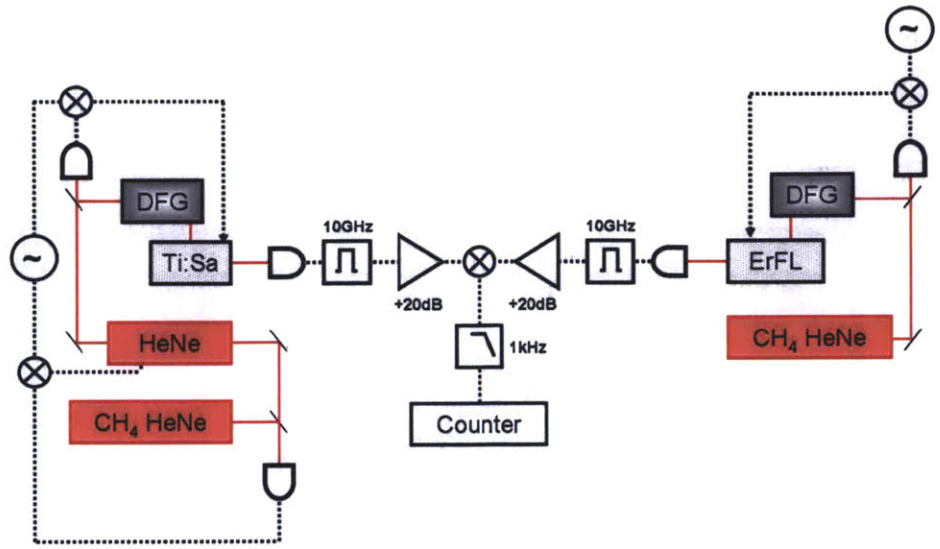

Figure 5-19: Setup for DFG-locked ErFL/Ti:Sa comparison measurements. The 10GHz repetition rate harmonic of the DFG-locked ErFL and Ti:Sa systems are detected, bandpass filtered, amplified, and then mixed down to a counter measuring frequency differences.

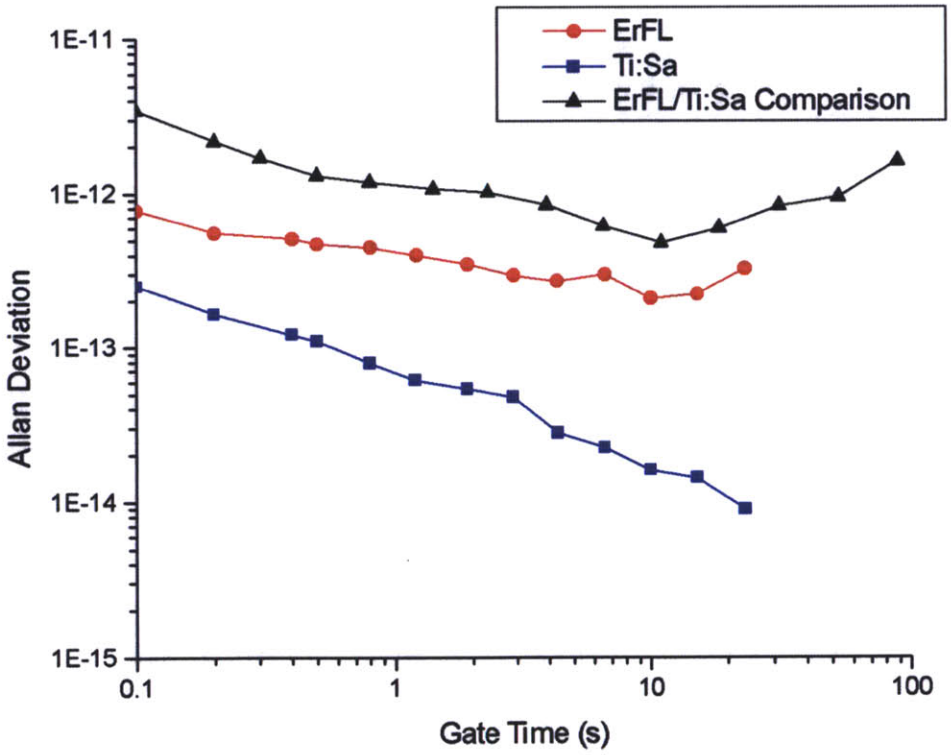

Figure 5-20: ErFL/Ti:Sa Allan Deviation comparison. Allan deviation measurements for the DFG-locked ErFL and Ti:Sa systems are shown for gate times up to 100 seconds. The measurements are limited by the ErFL DFG-HeNe lock, as the comparison of ErFL (red) and Ti:Sa (blue) DFG-HeNe beat stability measurements indicate.

Chapter 6

Frequency Multiplication Experiments*

Frequency multiplication techniques can be used to further extend pulse repetition rate [79]. Applied outside the laser cavity, these techniques offer increases to repetition rate with much fewer stringent requirements for implementation. This form of multiplication isn't perfect, however, as only partial suppression of unwanted frequency modes can be achieved. In other words, modulation at the fundamental frequency, associated with coupling of the input fundamental pulse train to the output multiplied pulse train, cannot be completely avoided. It can only be limited, with the use of high Q cavities. For most applications, especially those that don't involve nonlinear amplification[24], this partial level of suppression should be more than sufficient. To this end, a Fabry-Pérot (FP) interferometric approach to frequency multiplication is implemented to repetition rate multiply 1 GHz pulse trains up to 10 GHz.

Time and frequency domain descriptions of FP operation are illustrated in Fig. 6-1. In the time domain, input laser pulses feed an oscillating FP pulse which has a roundtrip time that's exactly a fraction of the laser roundtrip time. A portion of this oscillating FP pulse is output every roundtrip, resulting in a pulse train whose repetition rate is an exact multiple of the laser

* With contributions from Andrew Benedick

[24] Nonlinear four-wave mixing can severely reduce suppression levels.

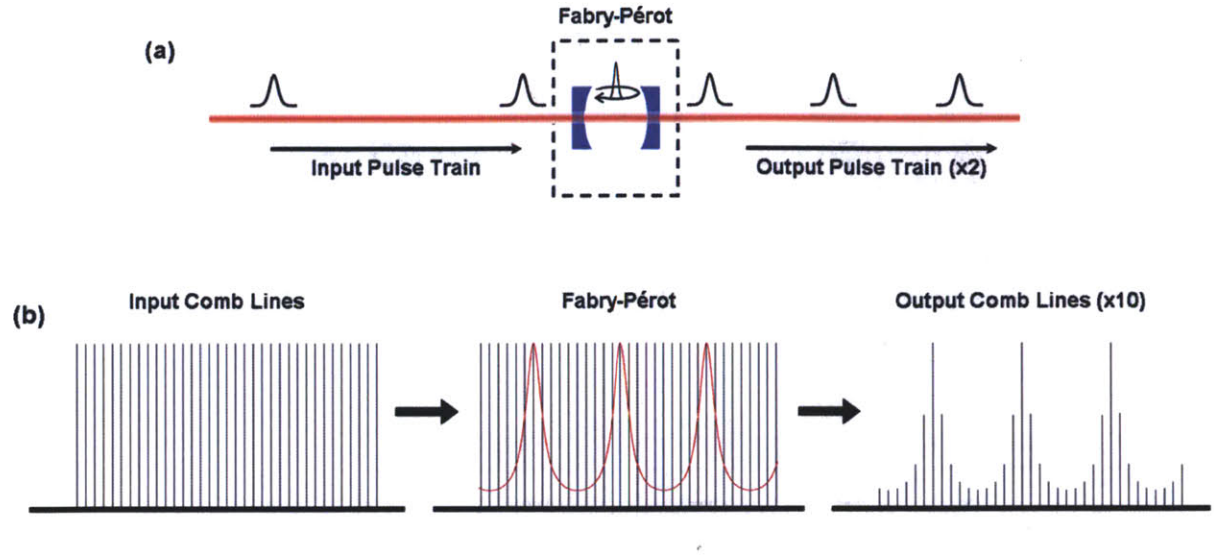

Figure 6-1: Fabry-Pérot repetition rate multiplication in the time and frequency domain. (a) Time domain description. The FP cavity roundtrip time is a fraction of the input pulse train period. The input pulses arrive at the FP input after multiple cavity roundtrips, whereas an output pulse is generated every cavity roundtrip. (b) Frequency domain description. The FP acts as a filter, filtering out every Nth comb line leading to an N times increase in repetition rate when its free spectral range is an exact multiple (N) of the input comb spacing. The N-1 filtered comb lines are only partially suppressed – its level of suppression determined by the cavity Q (or cavity finesse).

repetition rate. A FP etalon acts as a filter in the frequency domain, with sharp transmission windows evenly spaced by the inverse cavity roundtrip time

$$\Delta\nu = \frac{c}{2nL} \tag{6.1}$$

also known as the free spectral range (c: speed of light in vacuum, n: refractive index, L: cavity length). Frequency multiplication results when the FP's free spectral range is an exact multiple of the laser repetition rate.

FP cavities used for frequency multiplication typically consist of two highly reflecting mirrors. Its finesse, determined from the mirror reflectivities ($r_{1,2}$) by

$$F = \frac{\Delta\nu}{\delta\nu} = \frac{\pi}{2\sin^{-1}\left(\frac{1-\sqrt{r_1 r_2}}{2\sqrt[4]{r_1 r_2}}\right)} \approx \frac{2\pi}{1-r_1 r_2} \tag{6.2}$$

is the ratio of the free spectral range ($\Delta\nu$) and transmission window bandwidth ($\delta\nu$), and provides a measure of the FP's filtering performance. No matter how sharp the FP's resonances, full suppression of non-resonant modes is not possible. The sharpness does, however, determine

suppression levels. In order to adequately suppress neighboring frequency modes, high reflectivity mirrors are needed. For the case of multiplying from 1 GHz to 10 GHz, r = 99% mirrors (F=313) suppress neighboring modes by 36 dB and r = 99.9% mirrors (F=3140) provide 56 dB suppression of neighboring modes. There's a limit to this multiplication, as higher factors require higher-Q cavities to ensure sufficient suppression of unwanted modes – the extent of this multiplication greatly depends on the target suppression levels. For instance, multiplication from 10 MHz to 10 GHz is achievable with r = 99.9% mirrors, so long as 16 dB of suppression is all that's needed (r = 99% mirrors only give ~1 dB of sidemode suppression). Though in theory, any multiplication factor and suppression level is possible with sufficiently high reflectivity mirrors (super-mirrors) and/or FP stages, as long as bandwidth and/or the complexity of multiple phase lock loops are not concerns.

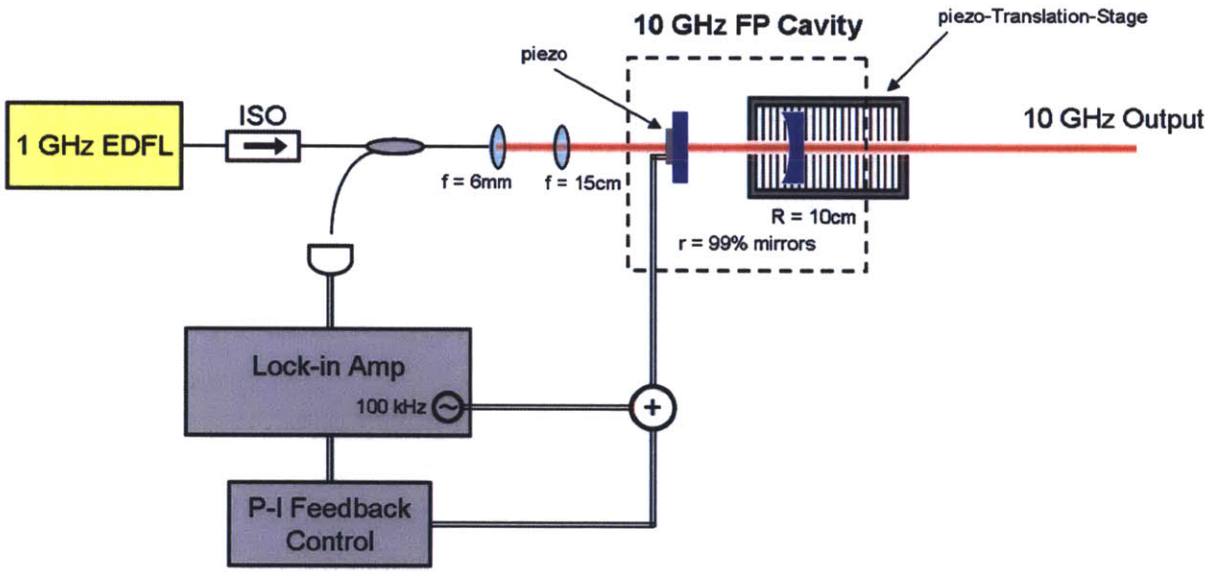

Figure 6-2: Fabry-Pérot repetition rate multiplication setup. The FP is locked to the 1GHz frequency comb input (free-running in these experiments) to generate a 10GHz output. A piezo-translation-stage is used for rough alignment of the FP cavity (consisting of a r=99% flat mirror and a r=99% R=10cm curved mirror). The flat mirror is mounted on a donut-shaped piezo, which is driven by the feedback control signal and a 100kHz modulation signal. The 100kHz modulation allows lock-in detection of the error signal, which is then sent into a loop filter with proportional integral gain to generate the feedback control signal.

6.1 Cavity Locking to Frequency Comb

To ensure the FP and frequency comb remain aligned, one must be stabilized to the other. Since the frequency comb has already been stabilized, the FP is locked to the frequency comb. For our frequency multiplication experiments, the dither-lock scheme depicted in Fig. 6-2 is employed. In this scheme, one of the FP mirrors is swept back and forth (i.e. dithered) at a lock-in detection frequency. The lock-in amplifier monitors the back-reflected FP response to generate an error signal. When aligned, a strong, steep-sloped error signal exists for locking.

An isolated 970 MHz pulse train[25], with optical and RF spectra shown in Fig. 6-3, serves as the input to a 10.67 GHz FP cavity (11x multiplication rate). The multiplication cavity consists of a flat planar mirror at the input and a curved (R=10 cm) mirror at the output, both with reflectivities of r = 99%. We chose a curved mirror resonator design, since the use of only flat mirrors would result in diffraction losses leading to lower cavity Q. For optimal coupling into the cavity, a mode-matching lens system comprising of a 6 mm lens collimator and a 150 mm plano-convex lens images the 10.4 μm MFD SMF-28e fiber output to 260 μm at the FP input.

One of the mirrors (curved) sits on a piezo-actuated translation stage providing the adjustment necessary for coarse alignment of the FP to the input pulse train, and the other mirror (flat) is mounted on a donut-shaped piezo for high-bandwidth cavity-length locking adjustments.

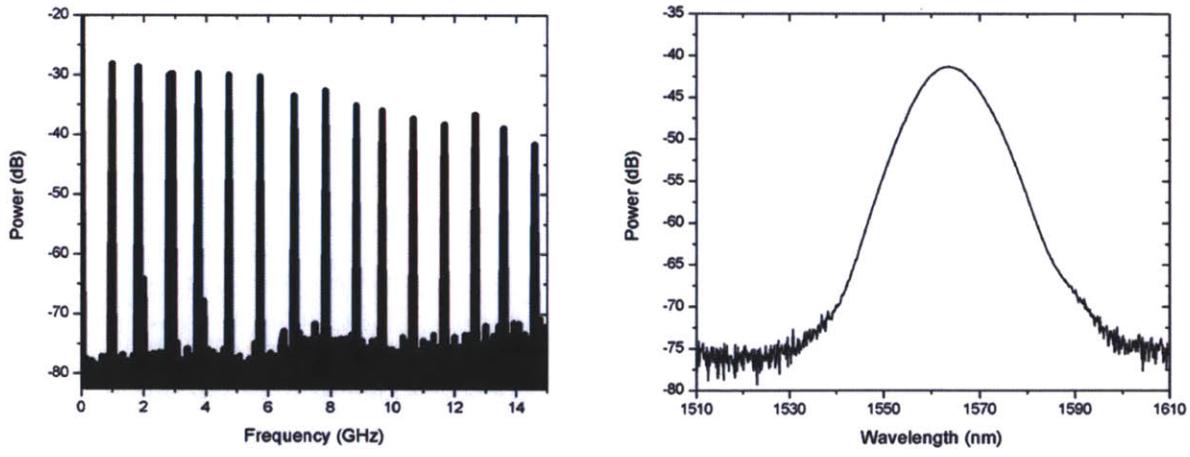

Figure 6-3: The 1GHz RF and optical input.

[25] This GHz input pulse train is free-running (unlocked) in these experiments to show the full capability of the dither-lock technique. A locked input pulse train should perform just as well, if not better.

The piezo is driven by the summation of two signals, a 100 kHz dithering reference signal from the lock-in amplifier and the P-I feedback control signal. A 90/10 fiber splitter is used to detect a portion of the back-reflected light, which is then sent back into the lock-in amplifier to generate the error signal via lock-in detection. A high-speed servo controller lockbox loop filters the error signal with P-I gain (Gain: 5.14, Corner Frequency: 1 kHz) to form the control signal. Locking the error signal to a non-zero bias point (Input Offset Voltage: 5.01 V) aligns the GHz pulse train to the FP cavity resonances (to one of its sides).

When locked, the RF spectrum of the 10.67 GHz output indicates a sidemode suppression of 28 dB, as seen in Fig. 6-4. This compares favorably with the predicted 36 dB optical suppression. r = 99.9% mirrors can be used if additional suppression is needed. Also, as expected, a zoom-in shot of the 10.67 GHz line shows modulation sidebands separated by the 100 kHz dithering frequency. The optical spectrum of the output, shown in Fig. 6-5, also provides confirmation of successful frequency multiplication. When unlocked, the optical

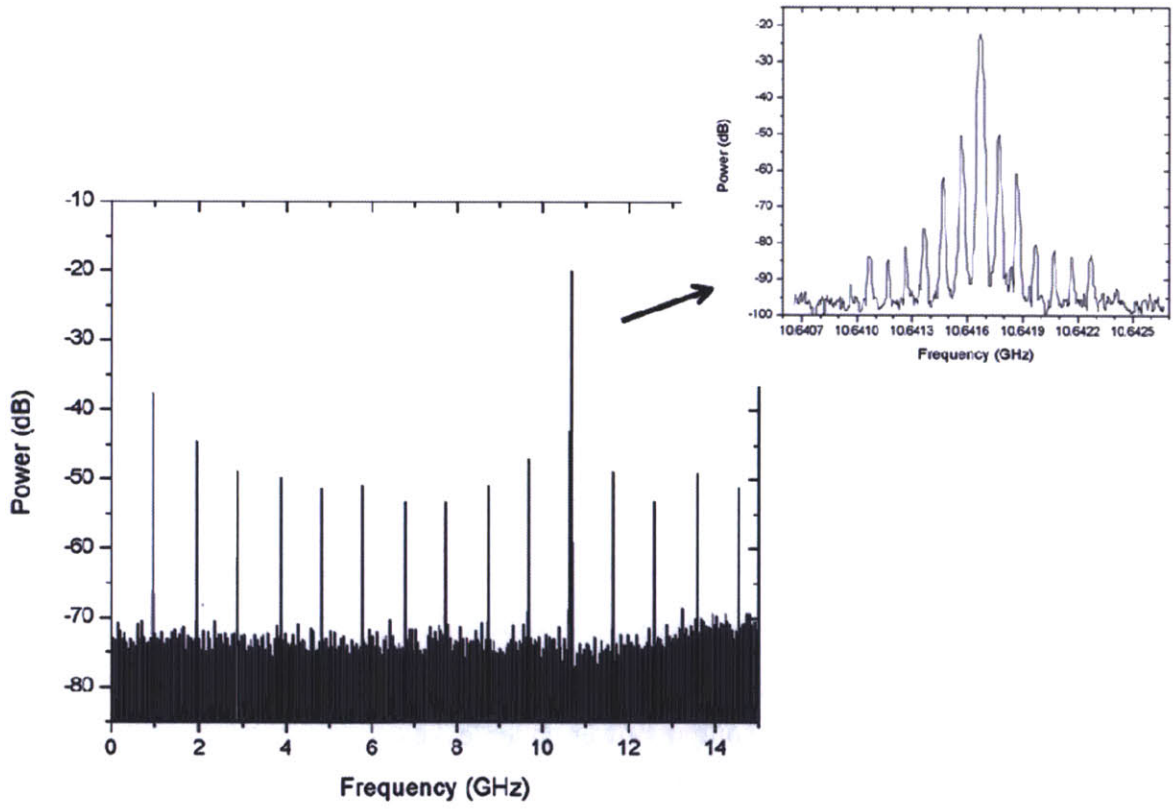

Figure 6-4: The 10GHz RF output. Repetition rate multiplication (x11) is achieved with 28dB RF sidemode suppression, as expected with a F=313 FP cavity. A zoom-in of the 10GHz line reveals the 100kHz modulation used for lock-in detection.

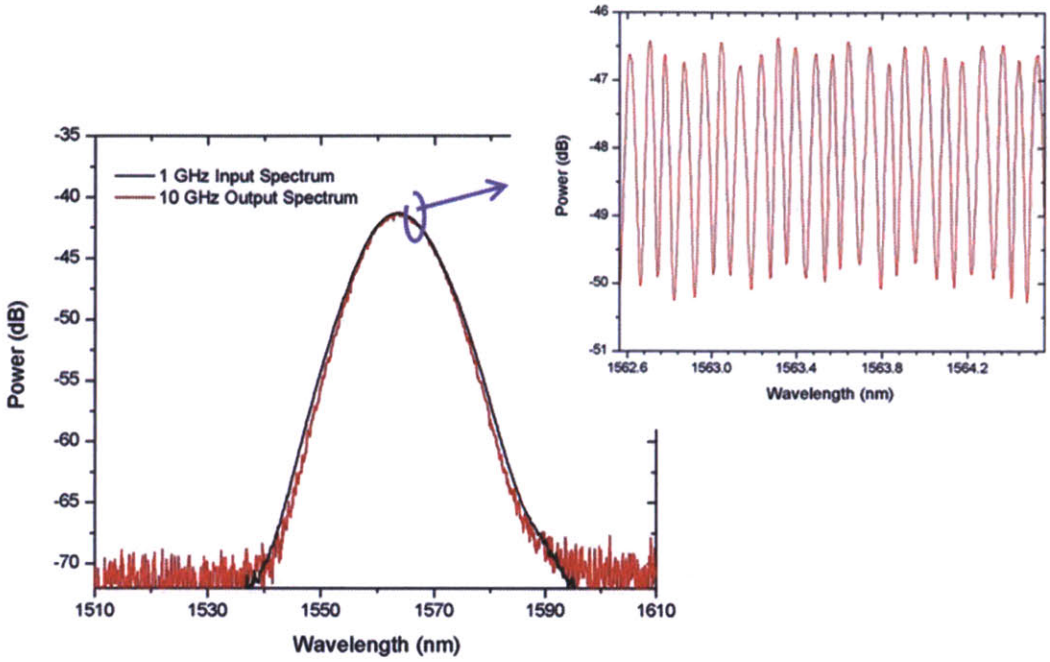

Figure 6-5: The 10GHz optical output. The 1GHz input and 10GHz output spectra are overlaid showing that the process is not yet bandwidth-limited. A zoom-in of the 10GHz spectrum reveals a 0.08nm modulation which corresponds to the 10GHz-spaced rep rate multiplied comb lines.

spectrum is unsettled due to output power fluctuations. In addition, its structure remains smooth since the OSA can't resolve 1 GHz spaced frequencies. The lock settles the optical spectrum so that one can start to make out the individual frequency lines, now spaced at 10 GHz, the resolution bandwidth limit of the OSA (0.08 nm RBW limit, which at 1560 nm corresponds to a spacing of 9.86 GHz). Because we're operating at the RBW limit, the individual frequency lines aren't fully resolved, but instead impart a sinusoidal modulation onto the optical spectrum. There's very little change in the spectral bandwidth of the multiplied output compared to the input, indicating that our multiplication cavity is not bandwidth limited, and can support even larger bandwidth inputs. If needed, dispersion flattened mirrors can be used for even more bandwidth. Finally, a measure of the output power under locked conditions, $P_{10.67\ GHz} = 0.39$ mW, compared to $P_{970\ MHz} = 7.9$ mW, verifies (provides further confirmation of) good cavity alignment. Perfect alignment and mode-matching would result in output powers of ~0.72 mW, if

aligned at the transmission peak. Additional losses from locking slightly off-resonance can easily account for the discrepancy.

Chapter 7

Conclusions and Future Research

This thesis set out to overcome the challenges associated with generating high repetition rate frequency combs – specifically, 1.5μm fiber frequency combs at GHz repetition rates. Compared to frequency combs based on solid-state architectures (10GHz repetition rates), and even those constructed using other fiber platforms such as Ytterbium-based fiber frequency combs at 1μm (1GHz repetition rates), Erbium-based fiber frequency combs at 1.5μm face a number of additional constraints which have so far limited their repetition rates to 300MHz (with little potential for further scaling). Techniques have been developed here making possible the first self-referenced 1.5μm fiber frequency comb at or above a GHz repetition rate. More importantly, these techniques have the capability of being scaled to even higher repetition rates, tens of GHz perhaps, potentially surpassing the solid-state frequency combs that are the current benchmark.

7.1 Thesis Summary

GHz Mode-locked Fiber Lasers

Fundamentally mode-locked fiber lasers have been constructed in two linear cavity configurations, one with an intracavity free-space section and the other all-fiber. Problems with SBR burning and vector solitons have been overcome leading to stable, compact and robust mode-locking at GHz repetition rates. Output pulses centered between 1550-1575nm with

optical bandwidths ranging from 5nm up to 15.6nm, corresponding to transform-limited pulse durations as low as 166fs and pulse energies as high as 25pJ, have been generated with these lasers.

Harmonically mode-locked fiber lasers have also been studied. 1 GHz repetition rate pulse trains were generated using regenerative phase modulation for sorting the intracavity pulses. However, the phase relationship of the individual pulses making up this pulse train were not correlated using such an approach. Gires-Tournois and Fabry-Pérot interferometers were therefore investigated for phase correlation, but harmonic mode-locking with either of these interferometers has so far been unsuccessful.

High-power Amplification and Femtosecond-pulse Compression

Raman fiber lasers are used as singlemode pump sources at 1480nm to provide high-power amplification with minimal accumulation of nonlinear phase shifts. 2 Watts of amplification is achieved (at a conversion efficiency of 41%) in only 1.2 meters of gain fiber. A compression scheme based on self-phase modulation in normal dispersion gain fiber produces compressible spectral generation allowing pulses to be compressed down to 95fs durations with only a modest pedestal. The resulting 2nJ/95fs pulses are sufficient for phase-coherent supercontinuum generation in HNLFs.

Octave-spanning Supercontinuum Generation

Supercontinuum generation experiments were conducted using a variety of dispersion-shifted small-core step-index HNLFs and PCFs. The OFS Type B HNLF worked best with our 2nJ/95fs pulses, generating over an octave of supercontinuum spanning 1μm-2.4μm (with peak concentrations of power at the f and 2f wavelengths) in a short length measuring just 11cm. The supercontinuum is shown to be highly phase-coherent leading to strong f_{ceo} beat detection.

Stabilization of f_{ceo} and f_{rep}

The f_{ceo} of the GHz all-fiber laser is detected using an f-2f self-referencing technique resulting in a 33dB SNR beat in a 100kHz RBW. Two approaches were implemented for locking the f_{ceo} beat, one involving feedback to the laser diode pumping the cavity and the other involving feedback to an external acousto-optic frequency shifter. The latter provided the more

stable lock, and measurements taken to characterize the quality of this lock revealed a locking bandwidth of 25kHz and an integrated residual phase noise of 3.97 rad from [10Hz,10MHz].

The f_{rep} of the GHz all-fiber laser is stabilized through butt-coupling modulation at the SBR end of the laser cavity to provide adjustments to its cavity length. A well-isolated laser experiences repetition rate fluctuations of 0.1kHz, which were compensated with cavity length adjustments of only 30nm. RF photodetection of the repetition rate was used to lock to an RF reference oscillator, resulting in an integrated timing jitter of 217fs from [10Hz,10MHz] with a 1kHz locking bandwidth. Since the f_{rep} lock typically limits frequency comb stability, a DFG technique for locking f_{rep} to an optical reference was implemented using a Menlo Systems 250MHz frequency comb as a proof-of-concept. Measurements showed this lock to be an order of magnitude better than RF locking of f_{rep}. A discussion of this approach for improving the overall stability of our GHz frequency combs will be provided in the next section.

Repetition Rate Multiplication using Fabry-Pérot Cavities

Repetition rate multiplication from 1GHz to 10GHz is accomplished by locking an external 10GHz Fabry-Perot cavity to the 1GHz input pulse train. This technique provides a path to higher repetition rates, but at the expense of only partial suppression of fundamental modes. RF sidemode suppression of 28dB is achieved with an F=313 cavity. If needed, better suppression (but never complete suppression) can be obtained with higher finesse FP cavities.

7.2 Future Research

Passively mode-locked HMLLs

The problem of phase correlation in harmonically mode-locked lasers has been well-documented here, and several approaches for its resolution have already been pursued, but have thus far proven unsuccessful as additional measures are required before stable operation can be achieved. Specifically, better temporal alignment of the interferometer and laser cavities is needed. Locking one cavity to the other (e.g. Pound-Drever-Hall cavity stabilization) is one option. A second option is to use saturable absorber mode-locking to provide timing adjustments through center wavelength shifts (together with cavity dispersion). Even with these timing adjustments, it's still important to make the interferometer as stable as possible to FSR

fluctuations. This can be achieved using ultra-stable FP cavities, constructed with low thermal expansion spacers (i.e. Schott Zerodur or Corning ULE) between the two highly-reflecting end mirrors.

Improvements to f_{ceo} lock

There is still room for improvement to the f_{ceo} lock, particularly with regards to increases in locking bandwidth. A phase lead circuit used in combination with pump power modulation has been shown to extend locking bandwidths out to 100kHz, resulting in a reduction of integrated phase noise to ~1 rad. Alternatively, the acousto-optic frequency shifting approach should have even greater potential for increased locking bandwidths (~1MHz) when properly optimized.

Improvements to f_{rep} lock

The DFG approach for locking f_{rep} to an optical reference can be implemented for the GHz frequency comb, which has only been locked using RF techniques to date – it is this lock which currently limits overall frequency comb stability. The supercontinuum generated in Fig. 4-7 is used to identify the optimal wavelengths for 3.39μm DFG to be 1060nm and 1550nm, as pictured in Fig. 7-1. This continuum possesses two advantages compared to the DFG

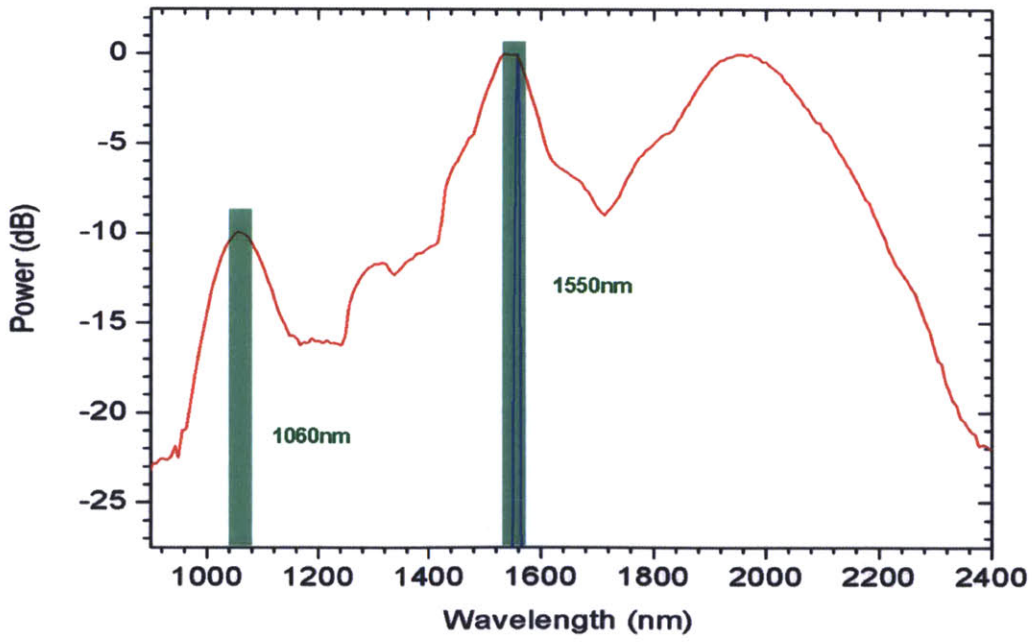

Figure 7-1: Proposed wavelengths for 3.39μm DFG.

experiments conducted with the Menlo Systems 250MHz frequency comb (which resulted in a 25dB DFG beat mainly limited by the amount of DFG generation). More power in the continuum at the appropriate wavelengths for the DFG process will produce an increase in DFG power. Since the 25dB DFG beat was ultimately limited by DFG (and not by the methane-stabilized HeNe), an increase in DFG power will lead to a stronger beat and a better lock. Drastically improved frequency comb stability should result – recall that even the 25dB DFG beat demonstrated a lock that's over an order of magnitude better than the best RF locks.

Bibliography

[1] Shapiro, S.L. Ultrashort Light Pulses (Picosecond Techniques and Applications). Topics in Applied Physics, v 18, (1984).

[2] Hargrove, L.E., Fork, R.L., and Pollack, M.A. Locking of He-Ne laser modes induced by synchronous intracavity modulation. Applied Physics Letters, v 5, p 4-5, (1964).

[3] DeMaria, A.J., Stetser, D.A., and Heynau, H. Self mode-locking of lasers with saturable absorbers. Applied Physics Letters, v 8, p 174-176, (1966).

[4] Ippen, E.P., Shank, C.V., and Dienes, A. Passive mode locking of the cw dye laser. Applied Physics Letters, v 21, p 348-350, (1972).

[5] Hall, J.L. Nobel Lecture: Defining and measuring optical frequencies. Reviews of Modern Physics, v 78, n 4, p 1279-95, (2006).

[6] Hansch, T.W. Nobel lecture: passion for precision. Reviews of Modern Physics, v 78, n 4, p 1297-309, (2006).

[7] Hocker, L.O., Javan, A., Rao, D.R., Frenkel, L., and Sullivan, T. Absolute frequency measurement and spectroscopy of gas laser transitions in the far infra-red. Applied Physics Letters, v 10, n 5, p 147-149, (1967).

[8] Evenson, K.M., Wells, J.S., Petersen, F.R., Danielson, B.L., and Day, G.W. Accurate frequencies of molecular transitions used in laser stabilization: the 3.39-μm transition in CH_4 and the 9.33- and 10.18-μm transitions in CO_2. Applied Physics Letters, v 22, n 4, p 192-5, (1973).

[9] Udem, T., Huber, A., Gross, B., Reichert, J., Prevedelli, M., Weitz, M., and Hansch, T.W. Phase-coherent measurement of the hydrogen 1S-2S transition frequency with an optical frequency interval divider chain. Physical Review Letters, v 79, n 14, p 2646-9, (1997).

[10] Schwob, C., Jozefowski, L., de Beauvoir, B., Hilico, L., Nez, F., Julien, L., Biraben, F., Acef, O., and Clairon, A. Optical frequency measurement of the 2S-12D transitions in hydrogen and deuterium: Rydberg constant and Lamb shift determinations. Physical Review Letters, v 82, n 25, p 4960-3, (1999).

[11] de Beauvoir, B., Schwob, C., Acef, O., Jozefowski, L., Hilico, L., Nez, F., Julien, L., Clairon, A., and Biraben, F. Metrology of the hydrogen and deuterium atoms: determination of the Rydberg constant and Lamb shifts. European Physical Journal D, v 12, n 1, p 61-93, (2000).

[12] Hils, D. and Hall, J.L. Improved Kennedy-Thorndike experiment to test special relativity. Physical Review Letters, v 64, n 15, p 1697-700, (1990).

[13] Niering, M., Holzwarth, R., Reichert, J., Pokasov, P., Udem, T., Weitz, M., Hansch, T.W., Lemonde, P., Santarelli, G., Abgrall, M., Laurent, P., Salomon, C., and Clairon, A. Measurement of the hydrogen 1S-2S transition frequency by phase coherent comparison with a microwave cesium fountain clock. Physical Review Letters, v 84, n 24, p 5496-9, (2000).

[14] Diddams, S.A., Udem, T., Bergquist, J.C., Curtis, E.A., Drullinger, R.E., Hollberg, L., Itano, W.M., Lee, W.D., Oates, C.W., Vogel, K.R., and Wineland, D.J. An optical clock based on a single trapped $^{199}Hg^{+}$ ion. Science, v 293, n 5531, p 825-8, (2001).

[15] Thorpe, M.J., Moll, K.D., Jones, R.J., Safdi, B., and Ye, J. Broadband cavity ringdown spectroscopy for sensitive and rapid molecular detection. Science, v 311, n 5767, p 1595-9, (2006).

[16] Chang, Z. and Corkum, P. Attosecond photon sources: the first decade and beyond. Journal of the Optical Society of America B (Optical Physics), v 27, n 11, p B9-B17, (2010).

[17] Diddams, S.A., Hollberg, L., and Mbele, V. Molecular fingerprinting with the resolved modes of a femtosecond laser frequency comb. Nature, v 445, n 7128, p 627-30, (2007).

[18] Thorpe, M.J., Balslev-Clausen, D., Kirchner, M.S., and Ye, J. Cavity-enhanced optical frequency comb spectroscopy: application to human breath analysis. Optics Express, v 16, n 4, p 2387-97, (2008).

[19] Kim, J., Park, M.J., Perrott, M.H., and Kartner, F.X. Photonic subsampling analog-to-digital conversion of microwave signals at 40-GHz with higher than 7-ENOB resolution. Optics Express, v 16, n 21, p 16509-15, (2008).

[20] Li, C., Benedick, A.J., Fendel, P., Glenday, A.G., Kartner, F.X., Phillips, D.F., Sasselov, D., Szentgyorgyi, A., and Walsworth, R.L. A laser frequency comb that enables radial velocity measurements with a precision of 1 cm s^{-1}. Nature, v 452, n 7187, p 610-12, (2008).

[21] Ippen, E., Benedick, A., Birge, J., Byun, H., Chen, L.-J., Chang, G., Chao, D., Morse, J., Motamedi, A., Sander, M., Petrich, G., Kolodziejski, L., and Kartner, F. Optical Arbitrary Waveform Generation (paper JThC4). 2010 Conference on Lasers and Electro-Optics (CLEO), (2010).

[22] Yoo, S.J.B. Monolithically integrated optical arbitrary waveform generators by line-by-line amplitude and phase modulators (paper WB4). IEEE Lasers and Electro-Optics Society 2008 Annual Meeting, p 425-6, (2008).

[23] Jiang, Z., Leaird, D.E., and Weiner, A.M. Line-by-line pulse shaping control for optical arbitrary waveform generation. Optics Express, v 13, n 25, (2005).

[24] Dugan, M.A., Tull, J.X., and Warren, W.S. High-resolution acousto-optic shaping of unamplified and amplified femtosecond laser pulses. Journal of the Optical Society of America B (Optical Physics), v 14, n 9, p 2348-58, (1997).

[25] Cao, J., Broeke, R.G., Fontaine, N.K., Ji, C., Du, Y., Chubun, N., Aihara, K., Pham, A., Olsson, F., Lourdudoss, S., and Yoo, S.J.B. Demonstration of spectral phase O-CDMA encoding and decoding in monolithically integrated arrayed-waveguide-grating-based encoder. IEEE Photonics Technology Letters, v 18, n 24, p 2602-4, (2006).

[26] Fontaine, N.K., Scott, R.P., and Yoo, S.J.B. Dynamic optical arbitrary waveform generation and detection in InP photonic integrated circuits for Tb/s optical communications. Optics Communications, v 284, n 15, p 3693-705, (2011).

[27] Telle, H.R., Steinmeyer, G., Dunlop, A.E., Stenger, J., Sutter, D.H., and Keller, U. Carrier-envelope offset phase control: a novel concept for absolute optical frequency measurement and ultrashort pulse generation. Applied Physics B (Lasers and Optics), v B69, n 4, p 327-32, (1999).

[28] Jones, D.J., Diddams, S.A., Ranka, J.K., Stentz, A., Windeler, R.S., Hall, J.L., and Cundiff, S.T. Carrier-envelope phase control of femtosecond mode-locked laser and direct optical frequency synthesis. Science, v 288, n 5466, p 635-9, (2000).

[29] Diddams, S.A., Jones, D.J., Ye, J., Cundiff, T., Hall, J.L., Ranka, J.K., Windeler, R.S., Holzwarth, R., Udem, T., and Hansch, T.W. Direct link between microwave and optical frequencies with a 300 THz femtosecond laser comb. Physical Review Letters, v 84, n 22, p 5102-5, (2000).

[30] Ell, R., Morgner, U., Kartner, F.X., Fujimoto, J.G., Ippen, E.P., Scheuer, V., Angelow, G., Tschudi, T., Lederer, M.J., Boiko, A., and Luther-Davies, B. Generation of 5-fs pulses and octave-spanning spectra directly from a Ti:sapphire laser. Optics Letters, v 26, n 6, p 373-5, (2001).

[31] Chen, L., Benedick, A.J., Birge, J.R., Sander, M.Y., and Kartner, F.X. Octave-spanning, dual-output 2.166 GHz Ti:sapphire laser. Optics Express, v 16, n 25, p 20699-705, (2008).

[32] Bartels, A., Heinecke, D., Diddams, S.A. 10-GHz Self-Referenced Optical Frequency Comb. Science, v 326, n 5953, p 681, (2009).

[33] Washburn, B.R., Diddams, S.A., Newbury, N.R., Nicholson, J.W., Yan, M.F., and Jorgensen, C.G. Phase-locked, erbium-fiber-laser-based frequency comb in the near infrared. Optics Letters, v 29, n 3, p 250-2, (2004).

[34] Hartl, I., Mckay, H.A., Thapa, R., Thomas, B.K., Dong, L., and Fermann, M.E. GHz Yb-femtosecond-fiber laser frequency comb (paper CMN1). 2009 Conference on Lasers and Electro-Optics (CLEO), (2009).

[35] Peng, J., Liu, T., and Shu, R. Octave-spanning fiber laser comb with 300 MHz Comb spacing for optical frequency metrology (paper CTuK3). 2009 Conference on Lasers and Electro-Optics (CLEO), (2009).

[36] Ruehl, A., Mai-cinkevicius, A., Fermann, M.E., and Hartl, I. 80 W, 120 fs Yb-fiber frequency comb. Optics Letters, v 35, n 18, p 3015-17, (2010).

[37] Mollenauer, L.F. and Stolen, R.H. The soliton laser. Optics Letters, v 9, n 1, p 13-15, (1984).

[38] Tamura, K., Ippen, E.P., Haus, H.A., and Nelson, L.E. 77-fs pulse generation from a stretched-pulse mode-locked all-fiber ring laser. Optics Letters, v 18, n 13, p 1080-2, (1993).

[39] Ilday, F.O., Buckley, J.R., Lim, H., Wise, F.W., and Clark, W.G. Generation of 50-fs, 5-nJ pulses at 1.03 μm from a wave-breaking-free fiber laser. Optics Letters, v 28, n 15, p 1365-7, (2003).

[40] Wilken, T., Hansch, T.W., Holzwarth, R., Adel, P., and Mei, M. Low phase noise 250 MHz repetition rate fiber fs laser for frequency comb applications (paper CMR3). 2007 Conference on Lasers and Electro-Optics (CLEO), (2007).

[41] Chen, J., Sickler, J.W., Ippen, E.P., and Kartner, F.X. High repetition rate, low jitter, low intensity noise, fundamentally mode-locked 167 fs soliton Er-fiber laser. Optics Letters, v 32, n 11, p 1566-8, (2007).

[42] Kelly, S.M.J. Characteristic sideband instability of periodically amplified average soliton. Electronics Letters, v 28, n 8, p 806-7, (1992).

[43] Jones, D.J., Chen, Y., Haus, H.A., and Ippen, E.P. Resonant sideband generation in stretched-pulse fiber lasers. Optics Letters, v 23, n 19, p 1535-7, (1998).

[44] Morse, J.L., Sickler, J.W., Chen, J., Kartner, F.X., and Ippen, E.P. High repetition rate, high average power, femtosecond erbium fiber ring laser (paper CML1). 2009 Conference on Lasers and Electro-Optics (CLEO), (2009).

[45] Chen, J., Sickler, J.W., Byun, H., Ippen, E.P., Jiang, S., and Kartner, F.X. Fundamentally mode-locked 3 GHz femtosecond erbium fiber laser. Ultrafast Phenomena XIV: Proceedings of the 16th International Conference, p 727-9, (2008).

[46] Martinez, A. and Yamashita, S. Multi-gigahertz repetition rate passively modelocked fiber lasers using carbon nanotubes. Optics Express, v 19, n 7, p 6155-63, (2011).

[47] Motamedi, A.R. Ultrafast Nonlinear Optical Properties of Passive and Active Semiconductor Devices (PhD Thesis), (2011).

[48] Christodoulides, D.N. and Joseph, R.I. Vector solitons in birefringent nonlinear dispersive media. Optics Letters, v 13, n 1, p 53-5, (1988).

[49] Zakharov, V.E. and Shabat, A.B. Exact theory of two-dimensional self-focusing and one-dimensional self-modulation of waves in nonlinear media. Zhurnal Eksperimental'noi i Teoreticheskoi Fiziki, v 61, n 1, p 118-34, (1971).

[50] Grudinin, A.B., Richardson, D.J., and Payne, D.N. Energy quantisation in figure eight fibre laser. Electronics Letters, v 28, n 1, p 67-8, (1992).

[51] Collings, B.C., Bergman, K., and Knox, W.H. Stable multigigahertz pulse-train formation in a short-cavity passively harmonic mode-locked erbium/ytterbium fiber laser. Optics Letters, v 23, n 2, p 123-5, (1998).

[52] Quinlan, F., Williams, C., Ozharar, S., Gee, S., and Delfyett, P.J. Self-stabilization of the optical frequencies and the pulse repetition rate in a coupled optoelectronic oscillator. Journal of Lightwave Technology, v 26, n 15, p 2571-7, (2008).

[53] Yoshida, M., Kasai, K., and Nakazawa, M. Mode-hop-free, optical frequency tunable 40-GHz mode-locked fiber laser. IEEE Journal of Quantum Electronics, v 43, n 8, p 704-8, (2007).

[54] Nakazawa, M., Kasai, K., and Yoshida, M. C_2H_2 absolutely optical frequency-stabilized and 40 GHz repetition-rate-stabilized, regeneratively mode-locked picosecond erbium fiber laser at 1.53 μm. Optics Letters, v 33, n 22, p 2641-3, (2008).

[55] Yu, C.X., Haus, H.A., Ippen, E.P., Wong, W.S., and Sysoliatin, A. Gigahertz-repetition-rate mode-locked fiber laser for continuum generation. Optics Letters, v 25, n 19, p 1418-20, (2000).

[56] Drever, R.W.P., Hall, J.L., Kowalski, F.V., Hough, J., Ford, G.M., Munley, A.J., and Ward, H. Laser phase and frequency stabilization using an optical resonator. Applied Physics B (Photophysics and Laser Chemistry), v B31, n 2, p 97-105, (1983).

[57] Tamura, K. and Nakazawa, M. Dispersion-tuned harmonically mode-locked fiber ring laser for self-synchronization to an external clock. Optics Letters, v 21, n 24, p 1984-6, (1996).

[58] Pedersen, B., Dakss, M.L., Thompson, B.A., Miniscalco, W.J., Wei, T., and Andrews, L.J. Experimental and theoretical analysis of efficient erbium-doped fiber power amplifiers. IEEE Photonics Technology Letters, v 3, n 12, p 1085-7, (1991).

[59] Strickland, D. and Mourou, G. Compression of amplified chirped optical pulses. Optics Communications, v 56, n 3, p 219-21, (1985).

[60] Nicholson, J.W., Yan, M.F., Wisk, P., Fleming, J., DiMarcello, F., Monberg, E., Taunay, T., Headley, C., and DiGiovanni, D.J. Raman fiber laser with 81 W output power at 1480 nm. Optics Letters, v 35, n 18, p 3069-71, (2010).

[61] Gapontsev, V., Gapontsev, D., Platonov, N., Shkurikhin, O., Fomin, V., Mashkin, A., Abramov, M., and Ferin, S. 2 kW CW ytterbium fiber laser with record diffraction-limited brightness. 2005 Conference on Lasers and Electro-Optics Europe, p 508, (2005).

[62] Tomlinson, W.J., Stolen, R.H., and Shank, C.V. Compression of optical pulses chirped by self-phase modulation in fibres. Journal of the Optical Society of America B (Optical Physics), v 1, n 2, p 139-49, (1984).

[63] Agrawal, G.P. Nonlinear Fiber Optics, (2001).

[64] Dudley, J.M., Genty, G., and Coen, S. Supercontinuum generation in photonic crystal fiber. Reviews of Modern Physics, v 78, n 4, p 1135-84, (2006).

[65] Okuno, T., Onishi, M., Kashiwada, T., Ishikawa, S., and Nishimura, M. Silica-based functional fibers with enhanced nonlinearity and their applications. IEEE Journal of Selected Topics in Quantum Electronics, v 5, n 5, p 1385-91, (1999).

[66] Westbrook, P.S., Nicholson, J.W., Feder, K.S., and Yablon, A.D. Improved supercontinuum generation through UV processing of highly nonlinear fibers. Journal of Lightwave Technology, v 23, n 1, p 13-18, (2005).

[67] Serkin, V.N., Vysloukh, V.A., and Taylor, J.R. Soliton spectral tunnelling effect. Electronics Letters, v 29, n 1, p 12-13, (1993).

[68] Omenetto, F.G., Wolchover, N.A., Wehner, M.R., Ross, M., Efimov, A., Taylor, A.J., Kumar, V.V.R.K., George, A.K., Knight, J.C., Joly, N.Y., and Russell, P.St.J. Spectrally smooth supercontinuum from 350 nm to 3 μm in sub-centimeter lengths of soft-glass photonic crystal fibers. Optics Express, v 14, n 11, (2006).

[69] Miller, G.D., Batchko, R.G., Tulloch, W.M., Weise, D.R., Fejer, M.M., and Byer, R.L. 42%-efficient single-pass CW second-harmonic generation in periodically poled lithium niobate. Optics Letters, v 22, n 24, p 1834-6, (1997).

[70] Newbury, N.R. and Swann, W.C. Low-noise fiber-laser frequency combs (invited). Journal of the Optical Society of America B (Optical Physics), v 24, n 8, p 1756-70, (2007).

[71] Paschotta, R., Telle, H.R., and Keller, U. Noise of Solid State Lasers, (2007).

[72] Paschotta, R., Schlatter, A., Zeller, S.C., Telle, H.R., and Keller, U. Optical phase noise and carrier-envelope offset noise of mode-locked lasers. Applied Physics B (Lasers and Optics), v B82, n 2, p 265-73, (2006).

[73] Cundiff, S.T. Phase stabilization of ultrashort optical pulses. Journal of Physics D (Applied Physics), v 35, n 8, p R43-59, (2002).

[74] Haus, H.A. and Ippen, E.P. Group velocity of solitons. Optics Letters, v 26, n 21, p 1654-6, (2001).

[75] Koke, S., Grebing, C., Frei, H., Anderson, A., Assion, A., and Steinmeyer, G. Direct frequency comb synthesis with arbitrary offset and shot-noise-limited phase noise. Nature Photonics, v 4, n 7, p 462-5, (2010).

[76] Donley, E.A., Heavner, T.P., Levi, F., Tataw, M.O., and Jefferts, S.R. Double-pass acousto-optic modulator system. Review of Scientific Instruments, v 76, n 6, p 63112-1-6, (2005).

[77] McFerran, J.J., Swann, W.C., Washburn, B.R., and Newbury, N.R. Suppression of pump-induced frequency noise in fiber-laser frequency combs leading to sub-radian f_{ceo} phase excursions. Applied Physics B (Lasers and Optics), v B86, n 2, p 219-27, (2007).

[78] Gubin, M.A., Tyurikov, D.A., Shelkovnikov, A.S., Kovalchuk, E.V., Kramer, G., and Lipphardt, B. Transportable He-Ne/CH_4 optical frequency standard and absolute measurements of its frequency. IEEE Journal of Quantum Electronics, v 31, n 12, p 2177-82, (1995).

[79] Chen, J., Sickler, J.W., Fendel, P., Ippen, E.P., Kartner, F.X., Wilken, T., Holzwarth, R., and Hansch, T.W. Generation of low-timing-jitter femtosecond pulse trains with 2 GHz repetition rate via external repetition rate multiplication. Optics Letters, v 33, n 9, p 959-61, (2008).